Technical Physics Letters, Vol. 31, No. 11, 2005, pp. 901–904. Translated from Pis'ma v Zhurnal Tekhnicheskoĭ Fiziki, Vol. 31, No. 21, 2005, pp. 1–8.

Turbulent Phase Distribution during Lag Synchronization Breakage

A. A. Koronovskiĭ*, A. A. Tyshchenko, and A. E. Hramov**

Saratov State University, Saratov, Russia

*e-mail: * alkor@cas.ssu.runnet.ru; ** aeh@cas.ssu.runnet.ru*

Received May 31, 2005

Abstract—The distribution of turbulent phases in a time realization of dynamical systems in the regime of intermittent lag synchronization has been studied. A method of determining the duration of laminar and turbulent phases by means of the wavelet transform is proposed. © *2005 Pleiades Publishing, Inc.*

The synchronization of chaotic oscillations is a basic phenomenon in nature. Investigations into this phenomenon are of considerable importance, since it is encountered in many physical [1, 2], biological [3–5], and other systems.

There are several principal types of synchronization of coupled chaotic oscillators [6, 7]. Let us briefly mention some of these types. In the regime of complete (full) synchronization (CS) [8, 9], the vectors characterizing the states of the interacting systems obey the relation $\mathbf{x}_1(t) = \mathbf{x}_2(t)$: this equation is characteristic of identical chaotic oscillators. If the control parameters of the coupled systems are slightly different, the state vectors are close, $|\mathbf{x}_1(t)–\mathbf{x}_2(t)| \approx 0$, but still differ from each other. Another type of synchronization of coupled chaotic oscillators with slightly different control parameters is so-called lag synchronization (LS) [10, 11]. In this case, the oscillations in one system follow those in the other system with a certain time lag: $\mathbf{x}_2(t + \tau) \approx \mathbf{x}_1(t)$, where τ is the delay time. As the parameter of coupling between the two systems is increased, the delay time decreases and tends to zero, so that the coupled system pass to the CS regime. The phenomenon of phase synchronization (PS) is usually described and analyzed in terms of the phase $\phi(t)$ of a chaotic signal [6, 7, 12]. Then, the PS regime means entrainment of the phases of two chaotic oscillators, whereas their amplitudes remain uncorrelated. The transition from PS to LS proceeds via an intermittent lag synchronization (ILS) regime [11, 13]. In the analysis of this process, it is expedient to study a signal representing the difference $\mathbf{x}_2(t + \tau) – \mathbf{x}_1(t)$, which tends to zero in the LS regime. In the ILS state, this signal appears as a random sequence of regular (laminar) phases separated by irregular (turbulent) outbursts. By laminar phase, we mean the interval of time in which $|\mathbf{x}_2(t + \tau) – \mathbf{x}_1(t)| \approx 0$. Thus, the differential signal is subject to sharp variations of large amplitude. When the coupling parameter is increased, the number of such irregular outbursts decreases. This intermittent transient regime is referred to as the on–off intermittency [14].

In the analysis of intermittency, an important aspect is related to the diagnostics of laminar and turbulent phases of motion. There are effective methods of separating laminar phases (see, e.g., [13]), whereas the diagnostics of turbulent phases meets certain difficulties. Previously, we proposed [15] to analyze intermittency using wavelet transformation [16], which offers an effective approach to analysis of the behavior of nonlinear systems featuring complicated dynamics (see also [17, 18]). The continuous wavelet transform of a chaotic signal is defined as

$$W(t, s) = \frac{1}{\sqrt{s}}\int_{-\infty}^{+\infty} x(t')\psi^*\left(\frac{t-t'}{s}\right)dt', \qquad (1)$$

where $x(t)$ is a time realization, $\psi(\eta)$ is the base wavelet function (the asterisk denotes complex conjugation), and s is the analyzed time scale. For the base wavelet, we suggested the Morlet wavelet $\psi(\eta) = \pi^{-1/4}e^{j\omega_0\eta}e^{-\eta^2/2}$ representing a rapidly decaying harmonic function with $\omega_0 = 2\pi$ to be used. It was shown that the wavelet surface $|W(t, s)|$ has significantly different structures for the laminar and turbulent phases of motion [15]. Thus, an analysis of the wavelet surface structure can provide reliable separation of the different phases of motion.

Let us apply the approach based on the continuous wavelet transform to the analysis of two mutually (two-way) coupled nonidentical Rössler oscillators [14]:

$$\begin{aligned}\dot{x}_{1,2} &= -\omega_{1,2}y_{1,2} - z_{1,2} + \varepsilon(x_{2,1} - x_{1,2}),\\ \dot{y}_{1,2} &= \omega_{1,2}x_{1,2} + ay_{1,2},\\ \dot{z}_{1,2} &= f + z_{1,2}(x_{1,2} - c),\end{aligned} \qquad (2)$$

1063-7850/05/3111-0901$26.00 © 2005 Pleiades Publishing, Inc.

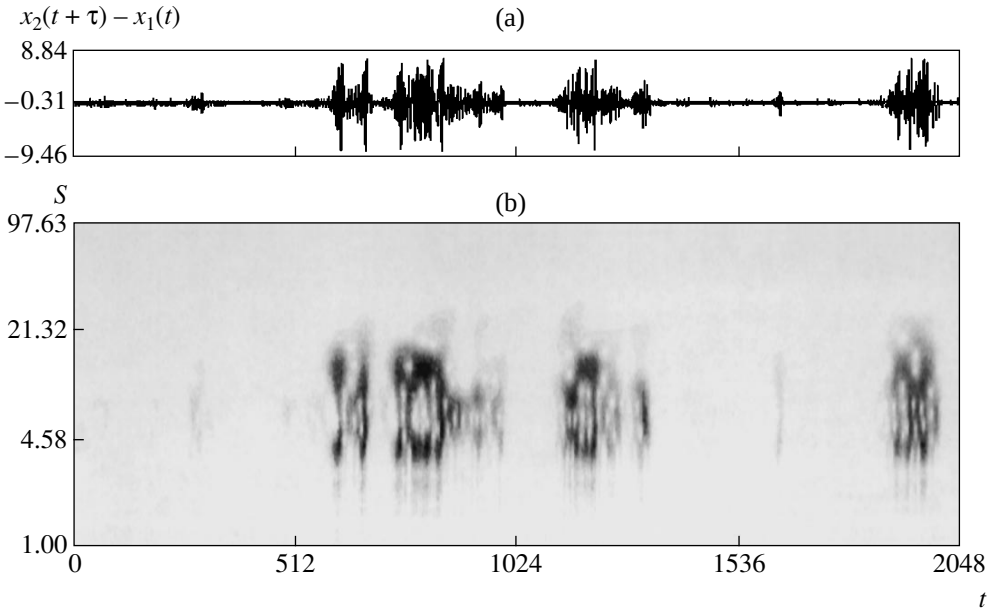

Fig. 1. The regime of intermittent lag synchronization between two coupled Rössler systems (2) with $\varepsilon = 0.13$ ($\tau = 0.32$): (a) the typical time series of the differential signal $\mathbf{x}_2(t+\tau) - \mathbf{x}_1(t)$; (b) the corresponding projection of the wavelet surface modulus $|W(t, s)|$.

where ε is the coupling parameter, $\omega_1 = 0.99$, $\omega_2 = 0.95$, $a = 0.165$, $f = 0.2$, and $c = 10$. As the ε value increases, the coupled systems sequentially exhibit the PS, LS, and CS regimes. In the interval $0.1 < \varepsilon < 0.15$ (corresponding to the passage from PS to LS regime) the coupled systems occur in the ILS state. For arbitrary systems, the delay time τ is usually determined using the similarity function (see, e.g., [11, 13, 14]). However, recently we demonstrated [19] that τ for the coupled systems under consideration is proportional to a phase shift between the main spectral components of the Fourier spectrum and depends on the coupling parameter according to the power law $\tau = k\varepsilon^{-1}$. For the values of parameters specified above, $k = 0.0418$. In this study, the delay time was determined using the established power relation.

Figure 1 shows the typical time series of the signal $\mathbf{x}_2(t+\tau) - \mathbf{x}_1(t)$ and the corresponding projection of the wavelet surface modulus $|W(t, s)|$ for $\varepsilon = 0.13$ ($\tau = 0.32$). The dark regions correspond to maxima of the wavelet surface. As can be seen, the projection of the wavelet surface modulus clearly reveals a pattern of laminar and turbulent phases in the given time series. In the regime of chaotic dynamics, the maxima of the wavelet surface correspond to the outbursts of oscillations with various time scales. Regions corresponding to the turbulent phases are clearly localized on the time scale. In the laminar periods, the wavelet surface structure remains virtually unchanged and its amplitude is minimal.

Figure 2a shows an average energy distribution with respect to the time scale for a time series duration of $N = 2^{15}$ dimensionless time units. This curve exhibits two clear maxima corresponding to the time scales $s_1 = 4.4$ and $s_2 = 9$. These values determine the average structure of the wavelet surface in the turbulent phase. We propose the following procedure for determining the duration of laminar and turbulent phases. First, the wavelet transformation $|W(t, s)|_{s = s_1, s_2}$ is constructed for the two time scales (s_1 and s_2) corresponding to the maxima of the averaged energy distribution $\langle E(s)\rangle$, and a threshold value Δ_i is selected for each wavelet curve $|W(t, s_i)|$ ($i = 1, 2$). As was noted above, the wavelet surface amplitude reaches maximum in the turbulent phases. It might seem natural to consider the motion as laminar when the given wavelet curve $|W(t, s_i)|$ is above the threshold and as turbulent when it is above this level. However, situations are possible where the amplitude of the wavelet curve $|W(t, s_1)|$ is at a minimum (i.e., is below the threshold Δ_1), whereas the $|W(t, s_2)|$ amplitude is greater than Δ_2 and vice versa, so that the time scale s_2 is predominating at a given moment of time. This possibility is related to the fact that the excitation and suppression of oscillations takes place for these very time scales over the entire turbulent phase. Therefore, exact determination of the laminar and turbulent phases requires the analysis to be performed for both time scales. Accordingly, the laminar phase is assigned only to the states in which both wavelet curves $|W(t, s_i)|$ are below the corresponding thresholds Δ_i. It should be noted that, if the system under consideration is characterized by a single maximum in the energy distribution over the time scales, the problem is simplified and the wavelet transformation can be considered for this single fixed scale.

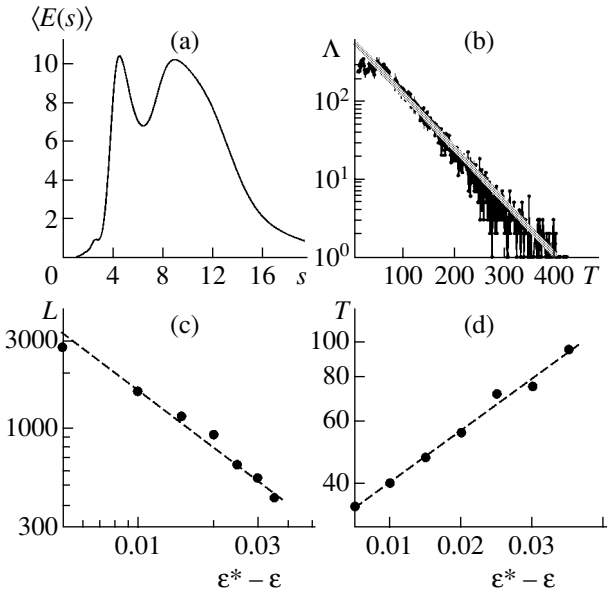

Fig. 2. The results of wavelet analysis of the regime of intermittent lag synchronization between two coupled Rössler systems (2): (a) an average energy distribution with respect to the time scale for $\varepsilon = 0.1$ ($\Delta_1 = 2$, $\Delta_2 = 1.5$); (b) a statistical distribution Λ (plotted on a logarithmic scale) of the turbulent phase duration T for $\varepsilon = 0.1$ (solid line corresponds to the exponential dependence with an exponent of –0.015); (c) a double logarithmic plot of the average of the laminar phase duration L versus critical parameter $\varepsilon - \varepsilon^*$ near the LS regime threshold $\varepsilon^* \approx 0.15$ (dashed line corresponds to the power law with an exponent of –1); (d) a semilogarithmic plot of the average turbulent phase duration T versus critical parameter $\varepsilon - \varepsilon^*$ near the LS regime threshold $\varepsilon^* \approx 0.15$ (dashed line corresponds to an exponential law).

Using the method described above, we have obtained the distributions of laminar and turbulent phases in the course of breakage of the LS regime for various values of the coupling parameter and determined the dependence of the average durations of these phases on the coupling parameter. Figure 2b shows the statistical distribution Λ (plotted on a logarithmic scale) of the turbulent phase duration T for $\varepsilon = 0.1$. The number of analyzed phases was about 30000 of the characteristic intervals. As can be seen, the distribution obeys the exponential law with an exponent of –0.015. The analogous distribution for the laminar phases obeys the power law with an exponent of –3/2 (this value is typical of the on–off intermittency) [13].

We have also constructed plots of the average duration of the laminar and turbulent phases versus the critical parameter $\varepsilon - \varepsilon^*$, where $\varepsilon^* \approx 0.15$ is a threshold coupling parameter for establishment of the LS regime (Figs. 2c and 2d). These characteristics were determined for 600–2700 phases (at a fixed length of the time series). When the coupling parameter increases in the interval $0.11 < \varepsilon < 0.15$, the number of turbulent (and laminar) phases sharply decreases, the laminar phases become longer, and the turbulent phases become shorter. Figure 2c presents a plot of the laminar phase duration L versus critical parameter $\varepsilon - \varepsilon^*$ on a double logarithmic scale. As can be seen, the average L value decreases according to the power law $(\varepsilon^* - \varepsilon)^{-1}$ typical of the on–off intermittency. Figure 2d presents a plot of the turbulent phase duration T (in the logarithmic scale) versus $\varepsilon - \varepsilon^*$. As can be seen, the average T value grows according to the exponential law with increasing difference $\varepsilon^* - \varepsilon$. It should be emphasized that the proposed method (in contrast to that described in [13]) readily provides data on the turbulent phase durations.

In conclusion, we have developed an effective method based on wavelet transformation for an analysis of the LS regime breakage in a system of two coupled chaotic oscillators. The results obtained for the average laminar phase duration agree well with the data published previously [13]. It is established that the turbulent phase duration obeys an exponential dependence on the deviation of the coupling parameter from the LS threshold value. The proposed wavelet analysis procedure has quite a universal character with respect to the description of intermittency and, hence, can be used for the separation and analysis of laminar and turbulent phases in the time series of various dynamical systems exhibiting the phenomenon of intermittency.

Acknowledgments. This study was supported by the Russian Foundation for Basic Research (project nos. 05-02-16273 and 05-02-16282), the Presidential Program of Support for Leading Scientific Schools in Russia (project no. NSh-1250.2003.02), and the Science and Education Center "Nonlinear Dynamics and Biophysics" at Saratov State University (sponsored by the US Civilian Research and Development Foundation for the Independent States of the Former Soviet Union, CRDF award no. REC-006). The authors also gratefully acknowledge support from the "Dynasty" Foundation and the International Center for Basic Research in Physics (Moscow).

REFERENCES

1. E. Allaria, F. T. Arecchi, A. D. Garbo, and R. Meucci, Phys. Rev. Lett. **86**, 791 (2001).
2. D. I. Trubetskov and A. E. Hramov, Radiotekh. Élektron. (Moscow) **48**, 116 (2003).
3. V. S. Anishchenko, A. G. Balanov, N. B. Janson, *et al.*, Int. J. Bifurcation Chaos Appl. Sci. Eng. **10**, 2339 (2000).
4. R. C. Elson *et al.*, Phys. Rev. Lett. **81**, 5692 (1998).
5. N. F. Rulkov, Phys. Rev. E **65**, 041922 (2002).
6. A. Pikovsky, M. Rosenblum, and J. Kurths, *Synchronization: A Universal Concept in Nonlinear Sciences* (Cambridge Univ. Press, Cambridge, 2001).
7. V. S. Anishchenko, T. E. Vadivasova, and V. V. Astakhov, *Nonlinear Dynamics of Chaotic and Stochastic Systems* (Izd. Saratovsk. Univ., Saratov, 1999) [in Russian].

8. L. M. Pecora and T. L. Carroll, Phys. Rev. A **44**, 2374 (1991).
9. K. Murali and M. Lakshmanan, Phys. Rev. E **49**, 4882 (1994).
10. O. Sosnovtseva, A. Balanov, T. Vadivasova, *et al.*, Phys. Rev. E **60**, 6560 (1999).
11. S. Boccaletti and D. Valladares, Phys. Rev. E **62**, 7497 (2000).
12. A. Pikovsky, M. Rosenblum, and J. Kurths, Int. J. Bifurcation Chaos Appl. Sci. Eng. **10**, 2291 (2000).
13. Meng Zhan, G. W. Wei, and C.-H. Lai, Phys. Rev. E **65**, 036202 (2002).
14. M. G. Rosenblum, A. S. Pikovsky, and J. Kurths, Phys. Rev. Lett. **78**, 4193 (1997).
15. A. A. Koronovskiĭ and A. E. Hramov, Pis'ma Zh. Tekh. Fiz. **27** (1), 3 (2001) [Tech. Phys. Lett. **27**, 1 (2001)].
16. A. A. Koronovskiĭ and A. E. Khramov, *Continuous Wavelet Analysis and Its Applications* (Fizmatlit, Moscow, 2003) [in Russian].
17. A. Hramov and A. Koronovskiĭ, Chaos **14**, 603 (2004).
18. A. E. Hramov, A. A. Koronovskiĭ, and Yu. I. Levin, Zh. Éksp. Teor. Fiz. **127**, 886 (2005) [JETP **100**, 784 (2005)].
19. A. Hramov, A. Koronovskiĭ, M. K. Kurovskaya, and O. I. Moskalenko, Phys. Rev. E **71**, 056204 (2005).

Translated by P. Pozdeev

Technical Physics Letters, Vol. 31, No. 11, 2005, pp. 905–907. Translated from Pis'ma v Zhurnal Tekhnicheskoĭ Fiziki, Vol. 31, No. 21, 2005, pp. 9–16.

Wavelet Analysis of a Laser Interference Signal Measured upon Impact Excitation of the Reflector

O. I. Chanilov, D. A. Usanov*, A. V. Skripal', and A. S. Kamyshanskiĭ

Saratov State University, Saratov, Russia

** e-mail: UsanovDA@info.sgu.ru*

Received April 11, 2005

Abstract—By means of wavelet analysis of the laser interference response signal received from a system subjected to impact loading, it is possible to determine the absolute values of the characteristics of shock wave propagation in solids. This method has been applied to the experimental investigation of decaying oscillations induced in a metal rod by a single mechanical impact. *© 2005 Pleiades Publishing, Inc.*

Introduction. An analysis of the mechanical oscillations excited by impact in solid parts of various systems is of considerable basic interest in the physics of shock wave excitation in solids. At the same time, this analysis is important for evaluating the working properties of articles operating under impact loading conditions. The response to impact is usually determined with acoustic sensors. In order to determine the characteristics of mechanical oscillations induced by impact, such sensors must be preliminarily calibrated. The possibility of determining the absolute values of the characteristics of oscillations induced by impact without preliminary calibration is offered by laser interferometry.

Methods for solving the inverse problems in laser interferometry are well developed only for the case of periodic oscillations of a reflecting surface [1–3]. In such cases, the characteristics of oscillating systems can be determined by means of a Fourier analysis of the measured laser interference signal. However, the oscillations of a solid surface in response to impact are aperiodic, resembling the process developing upon a single initial perturbation in an oscillatory circuit with losses.

This paper shows that the characteristics of oscillations of the surface a solid excited by impact can be determined by means of wavelet analysis of an interference response signal [4, 5] received from an autodyne system with the reflector excited by impact.

Theoretical background of the proposed method. The normalized variable component of the interference signal in an autodyne system with the optical feedback coefficient $C \ll 1$ can be written in the following form [6]:

$$U(t) = \cos\left(\theta + \frac{4\pi}{\lambda} f(t)\right), \qquad (1)$$

where t is the current time, θ is the signal phase, λ is the laser radiation wavelength, and $f(t)$ is a function describing longitudinal motions of the object. The latter function can be represented using a wavelet transformation as

$$f(t) = K_{\psi_1}^{-1} \int_{-\infty}^{\infty}\int_{-\infty}^{\infty} C(a,b)\frac{1}{\sqrt{a}}\psi_1\left(\frac{t-b}{a}\right)\frac{da\,db}{a^2}, \qquad (2)$$

where

$$C(a,b) = \int_{-\infty}^{\infty} f(t)\frac{1}{\sqrt{a}}\psi_1\left(\frac{t-b}{a}\right)dt,$$

$$K_{\psi_1} = 2\pi\int_{-\infty}^{\infty}\frac{|\psi_f(\omega)|^2}{\omega}d\omega.$$

Here, ψ_1 is the base wavelet function, $C(a, b)$ are the coefficients of the wavelet expansion of $f(t)$ in the ψ_1 basis, K_{ψ_1} is a constant factor determined by the base wavelet function, and $\psi_f(\omega)$ is the Fourier transform of ψ_1. For Eq. (2) to be valid, the base function ψ_1 must possess wavelet properties—that is, it must be localized in both space and time, possess a zero average over the entire interval of time, and be limited.

Let us introduce a function $S(t)$ such that its spectrum corresponds to within a constant factor to the spectrum of the signal to be reconstructed [1]:

$$S(t) = \frac{dU/dt}{\pm\sqrt{1-U^2(t)}}. \qquad (3)$$

Taking into account expression (1) and using the integral representation of $f(t)$ given by Eq. (2), we can write the new function as

$$S(t) = \frac{4\pi}{\lambda K_{\psi_1}}\int_{-\infty}^{\infty}\int_{-\infty}^{\infty} C(a,b)\frac{1}{\sqrt{a}}\psi_2\left(\frac{t-b}{a}\right)\frac{da\,db}{a^2}, \qquad (4)$$

1063-7850/05/3111-0905$26.00 © 2005 Pleiades Publishing, Inc.

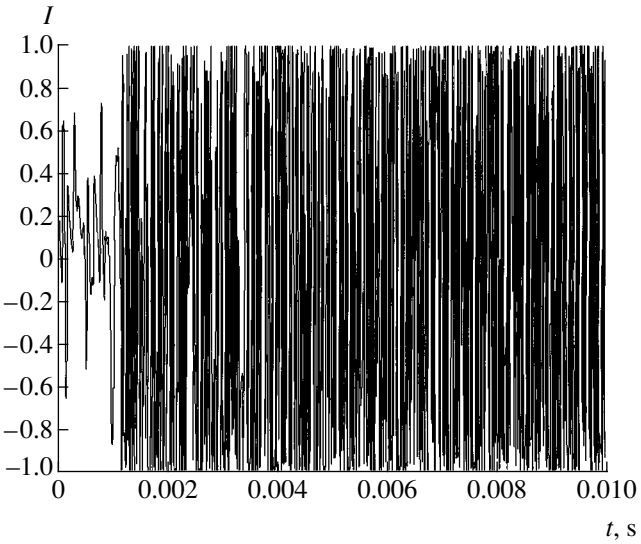

Fig. 1. A fragment of the autodyne response signal from an impact-loaded rod.

where ψ_2 is the derivative of the base wavelet function.

The sign in the denominator of expression (3) can be determined using the following procedure. First, the function $U(t)$ is used to calculate $\pm\sqrt{1-U^2(t)}$ at the first point, where the sign at the square root is set arbitrarily. Then, the sign of the derivative dU/dt is determined and the function $\sqrt{1-U^2(t)}$ is constructed so that its sign is changed to the opposite at the points where dU/dt is zero. If this function has discontinuities, its sign in the intervals between such points is changed to the opposite. This procedure leads to a continuous function $\pm\sqrt{1-U^2(t)}$ with the correctly selected sign.

Below, it is assumed that the wavelet function $\psi_1(t)$ is differentiable and its derivative is a wavelet. A comparison of the functions $f(t)$ and $S(t)$ given by Eqs. (2) and (4) shows that these expressions differ by the base wavelet functions and by the constant factor $4\pi/\lambda$. Constructing the function $S(t)$ based on the interference signal (1), we can expand it in the ψ_2 wavelet basis with the wavelet expansion coefficients

$$C(a,b) = \int_{-\infty}^{\infty} \frac{\lambda}{4\pi} S(t) \frac{1}{\sqrt{a}} \psi_2\left(\frac{t-b}{a}\right) dt. \qquad (5)$$

Using these coefficients, we can perform the inverse transformation in the ψ_1 bases to obtain

$$f(t) = K_{\psi_1}^{-1} \int_{-\infty}^{\infty}\int_{-\infty}^{\infty} C(a,b) \frac{1}{\sqrt{a}} \psi_1\left(\frac{t-b}{a}\right) \frac{da\,db}{a^2}. \qquad (6)$$

Thus, using the interference signal, it is possible to determine the function describing the motion of the part of the object from which a laser beam forming the interference response pattern is reflected. The arbitrary choice of the sign of $\pm\sqrt{1-U^2(t)}$ at the first point implies that we cannot determine the direction of motion. However, the proposed method can be successfully used in cases where the initial direction of motion is known a priori or when only the law of the object motion with time is of interest while the direction of this motion is insignificant.

Experimental results. In order to study oscillations induced by impact in a solid, we performed experiments using an autodyne system and a special impact-loading device mounted on an optical bench. The impact-loading device comprised a spring-driven striker and a fixed metal rod to which the impact load was applied. The spring compression was controlled by means of changing the plunger position. Thus, we have experimentally measured the motion of the rod edge surface, which was related to the time-dependent strain caused by the impact loading.

The experiments were performed using an autodyne system employing a laser diode of the RLD-650 type based on a quantum-confined semiconductor structure operating in a diffraction-limited solitary spatial mode. The laser parameters were as follows: output power, 5 mW; working wavelength, 652 nm; threshold current, 20 mA. The laser radiation reflected from the metal rod edge was used to form the autodyne signal, which was detected, amplified, processed by an analog-to-digital converter (ADC), and fed to a personal computer. The digitized signal was stored and processed so as to reconstruct the law of motion of the rod edge upon a single impact produced by the striker. In order to reduce the influence of noises in the electric circuit on the useful response signal, the laser operating in an autodyne mode was powered from a storage battery. The coefficient of reflection and the distance from the rod edge to the radiation source were selected such that the optical feedback coefficient obeyed the condition $C \ll 1$.

Figure 1 shows a fragment of the typical time series of a response signal measured by the photodetector. As can be seen, the signal was rather noisy, which was probably related to the instability of the laser diode frequency, mechanical vibrations of the experimental setup, and noise in the electric circuit. In order to decrease the effect of noise on the reconstructed signal, we used two-stage autodyne signal processing. Rough filtration of the noise was provided by a Savitzky–Golay digital filter [7], after which fine noise reduction was ensured by wavelet filtration using the MATLAB program package [8, 9].

The digitally filtered laser interference response signal was processed as described above so as to solve the inverse problem of laser interferometry and reconstruct the function describing the shock wave propagation in the solid rod. Figure 2 shows the reconstructed law of motion of the rod upon a single impact. As can be seen, the character of the shock wave propagation in the rod

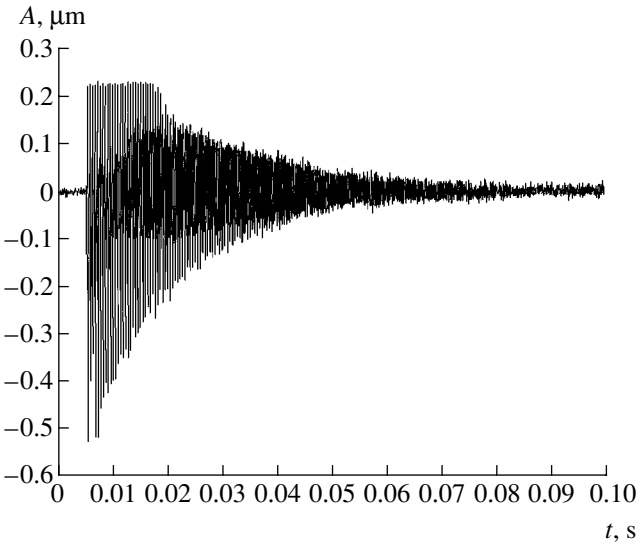

Fig. 2. The law of oscillatory motion of an impact-loaded metal rod as reconstructed by means of the wavelet analysis of the autodyne response signal.

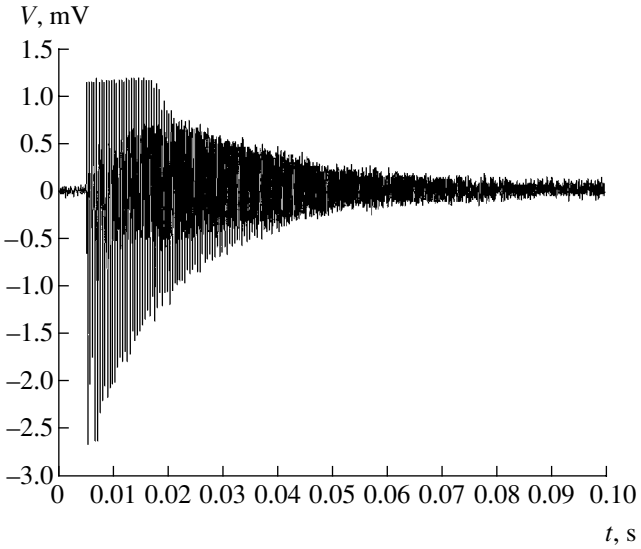

Fig. 3. Time variation of the self-induction emf in an impact-loaded rod measured using the induction technique.

is similar to the shape of oscillations observed upon a single initial perturbation in an oscillatory circuit with losses.

In order to verify the results obtained using the proposed method, we have also measured the parameters of shock wave propagation in the rod by means of the so-called induction technique. According to this, the impact-excited rod is placed inside an induction sensor whose output signal is digitized by an ADC and fed to a personal computer. The self-induction emf generated in the coil of the sensor is induced by oscillations of the rod caused by the propagating shock wave. The compression of the spring driving the striker was the same as that in the experiments with autodyne monitoring. Figure 3 presents the typical time variation of the self-induction emf measured by the induction technique, which is proportional to the rod displacement. A comparison of the patterns in Figs. 2 and 3 shows that the frequency and the logarithmic damping factor of oscillations determined using the interferometric method differ by no more than 0.5 and 1.2%, respectively, from the corresponding values obtained from the induction measurements. This is evidence of a good coincidence of the results obtained by the two methods.

Certain limitations of the proposed laser interferometric technique are related to the finite period of discretization of the measured autodyne signal, which is provided by the existing ADCs. In particular, the restricted rate of ADC operation makes it impossible to measure shock waves with a front rise time shorter than the discretization period. On the other hand, for a sufficiently large rise time of the shock wave front, it is expedient to use the method described previously [10].

Conclusion. We have demonstrated the possibility of determining the parameters of shock waves propagating in solids using wavelet analysis of the laser interference response signal received from an autodyne system employing a semiconductor laser and an impact-driven external reflector.

REFERENCES

1. S. V. Gangnus, A. V. Skripal', and D. A. Usanov, Avtometriya, No. 1, 31 (1999).
2. D. A. Usanov, A. V. Skripal', and S. V. Gangnus, Avtometriya, No. 1, 117 (2001).
3. S. V. Gangnus, D. A. Usanov, and A. V. Skripal, Proc. SPIE **3726**, 226 (1999).
4. N. M. Astaf'eva, Usp. Fiz. Nauk **166**, 1145 (1996) [Phys. Usp. **39**, 1085 (1996)].
5. A. V. Skripal', D. A. Usanov, and O. I. Chanilov, Avtometriya, No. 5, 56 (2004).
6. Z. Wang, M. S. Graca, P. J. Bryanston-Cross, *et al.*, Opt. Eng. **35**, 2327 (1996).
7. A. Savitzky and M. Golay, Anal. Chem. **36**, 1627 (1964).
8. V. P. D'yakonov, *MATLAB: Processing of Signals and Images (A Handbook)* (Piter, St. Petersburg, 2002) [in Russian].
9. V. P. D'yakonov, *Wavelets: From Theory to Practice* (SOLON, Moscow, 2002) [in Russian].
10. D. A. Usanov, A. V. Skripal', and A. S. Kamyshanskiĭ, Pis'ma Zh. Tekh. Fiz. **30** (7), 77 (2004) [Tech. Phys. Lett. **30**, 295 (2004)].

Translated by P. Pozdeev

Technical Physics Letters, Vol. 31, No. 11, 2005, pp. 908–911. Translated from Pis'ma v Zhurnal Tekhnicheskoĭ Fiziki, Vol. 31, No. 21, 2005, pp. 17–23.

Phase Transitions in Thin Titanium Oxide Films under the Action of Excimer Laser Radiation

P. Mitrev[a], G. Benvenuti[a], P. Hofman[a], A. Smirnov[b], N. Kaliteevskaya[b,*], and R. Seĭsyan[b]

[a] *Ecole Polytechnique Federale de Lausanne (EPFL), CH-1015 Lausanne, Switzerland*

[b] *Ioffe Physicotechnical Institute, Russian Academy of Sciences, St. Petersburg, 194021 Russia*

** e-mail: Natalia.Kalit@ffm.ioffe.ru*

Received June 21, 2005

Abstract—We have studied the action of pulsed vacuum ultraviolet (VUV) radiation of an ArF excimer laser (wavelength, 193 nm; pulse duration, 20 ns; pulse energy density, 40–50 J/cm^2) on thin amorphous films of titanium oxide (TiO_2) grown by light-assisted molecular beam epitaxy. A comparison of the Raman spectra of samples measured before and after exposure shows that VUV irradiation at increasing fluence induces the crystallization of amorphous TiO_2 to anatase, which is further transformed into rutile. © *2005 Pleiades Publishing, Inc.*

Owing to the advantageous combination of physical and chemical properties, titanium oxide (TiO_2) is widely used as a material for optical and protective films, photocatalysts, gas sensors, biocompatible coatings, etc. [1]. Another potential field of applications for this oxide is microelectronics. It has been suggested [2] to use titanium oxide films as photoresist in laser-beam lithography and as a high-permittivity material for the next generation of charge-storage devices (dynamic memory, field-effect transistors, etc.).

This paper presents the results of investigations into the action of pulsed vacuum ultraviolet (VUV) radiation of an ArF excimer laser operating at a wavelength of λ = 193 nm on thin amorphous films of titanium oxide (TiO_2) grown by light-assisted molecular beam epitaxy. The effects induced by excimer laser radiation in oxide films are of interest for two reasons. First, the relatively small radiation penetration depth focuses all the laser-induced physical and chemical processes predominantly in a thin (~10 nm) surface layer of the material. Thus, an energy of 1–100 kJ per unit film volume (1 cm × 1 cm × 10 nm) is deposited for the laser pulse energies within 1–100 mJ/cm^2. Second, the high laser photon energy ($h\nu \approx 6.4$ eV) is close to the molecular binding energy of TiO_2 and more than twice as large as the bandgap width of TiO_2 ($E_g \approx 3.18$ eV for anatase [3]).

Titanium oxide exists in three different crystal modifications: anatase, rutile, and brookite, the first two being most frequently encountered and used. According to the phase diagram of TiO_2 [4], anatase and brookite transform into rutile on heating to 700 and 900°C, respectively, while amorphous TiO_2 crystallizes into anatase on heating above 300°C. Accordingly, variation of the parameters of technological processes leads to the formation of TiO_2 coatings with different properties.

Numerous effects were observed previously in irradiated titanium oxide films grown by physical gas phase epitaxy [5], chemical vapor deposition [6], and electrochemical anodic oxidation [7]. It was also reported [8] that fluence-dependent changes in the composition and structure of pressed TiO_2 powder samples took place under the action of a pulsed KrF excimer laser (248 nm, 25 ns). In particular, the anatase–rutile phase transition was observed at a laser fluence above 710 mJ/cm^2.

Synthesis and characterization of TiO_2 films. Titanium oxide films were obtained by means of light-assisted molecular beam epitaxy in a reactor designed and constructed at EPFL (Lausanne, Switzerland). There are various types of vapor phase epitaxy (VPE), which can be subdivided depending on the method of activation—in particular, thermoactivated, plasma-enhanced, and light-assisted VPE. The method of light-assisted molecular beam epitaxy belongs to the latter type. A detailed description of these techniques is given in monographs [9, 10].

The main advantage of said reactor is the possibility of obtaining homogeneous deposits with a precisely controlled thickness on large-area substrates [11]. Films with a thickness nonuniformity below 2% can be deposited at a growth velocity ranging from 50 to 1000 nm/h. Our experiments were performed with TiO_2

1063-7850/05/3111-0908$26.00

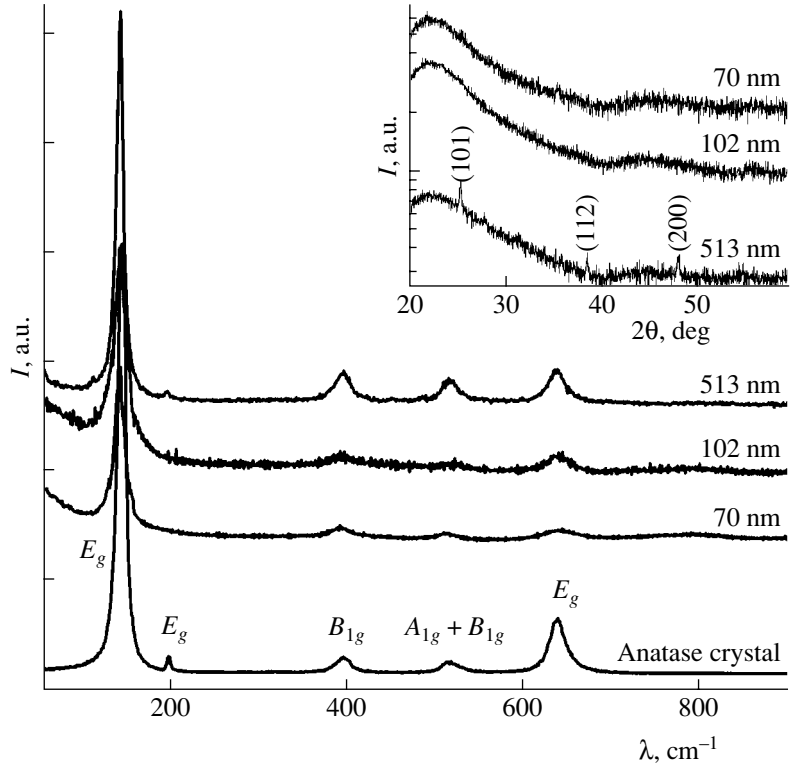

Fig. 1. The Raman spectra of three TiO_2 films of various thicknesses (indicated at the curves) in comparison to the spectrum of a pure anatase crystal. As can be seen, the anatase phase is present in all samples. The inset shows the fragments of X-ray duffractograms of the same films.

films of various thicknesses (70, 102, and 513 nm) grown on Pyrex glass substrates.

The film structures were studied and their degrees of crystallization were compared by means of X-ray diffraction. The results of such analysis are illustrated in the inset to Fig. 1. As can be seen from these data, the films with a thickness of 70 and 102 nm are substantially X-ray amorphous, whereas the 513-nm-thick film contains an anatase phase with the crystal lattice oriented in the (101), (112), and (200) directions. The latter sample was grown at a relatively low temperature (as compared to those used for the deposition of the two other films). Thus, the degree of crystallization in titanium oxide films obtained in the given reactor increases with the film thickness.

Figure 1 shows the Raman spectra of three TiO_2 films of various thicknesses in comparison to the spectrum of a pure anatase crystal. As can be seen, all three films contain the anatase phase. Indeed, except for the weak E_g peak at 199 cm^{-1} observed only for the 513-nm-thick film, all peaks characteristic of the anatase phase are well distinguished in the spectra of three samples, including E_g mode (143 and 640 cm^{-1}), $A_{1g} + B_{1g}$ double mode (516 cm^{-1}) and B_{1g} mode (399 cm^{-1}).

VUV-radiation-induced crystallization. Figure 2 shows a series of the Raman spectra of a 70-nm-thick TiO_2 film measured in the course of irradiation, which

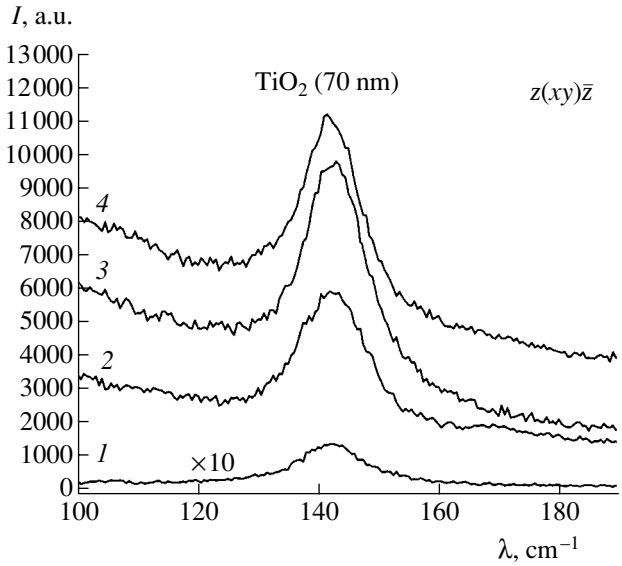

Fig. 2. The Raman spectra of a 70-nm-thick TiO_2 film measured (*1*) before irradiation and (*2–4*) after exposure to 64, 128, and 256 laser pulses, respectively, at an energy density of 45.1 mJ/cm^2.

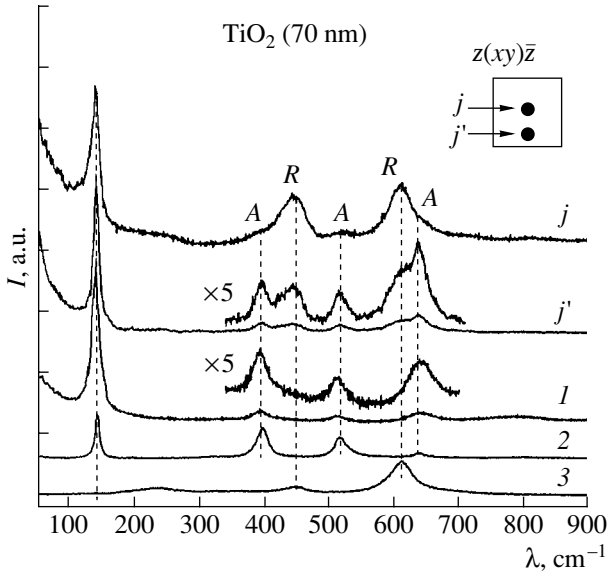

Fig. 3. The Raman spectra of a 70-nm-thick TiO_2 film (*1*) before irradiation and (*j*, *j*') after exposure to 256 laser pulses at an energy density of 46.1 mJ/cm^2 (for the sample probed at points *j* and *j*' of the laser-irradiated zone as indicated in the inset). Comparison to the spectra of (*2*) anatase and (*3*) rutile crystals shows that the laser irradiation leads to the anatase–rutile phase transition, which is more pronounced in the central (*j*') than in the peripheral (*j*') region of the irradiated zone.

demonstrate an increase in the degree of crystallization with increasing fluence of laser radiation with λ = 193 nm. Indeed, as can be seen, the exposure to an increasing number of laser radiation pulses with an energy density of 46.1 mJ/cm^2 leads to a significant increase in the intensity of the signal due to the crystalline phase. The peak intensity upon exposure to 128 and 256 laser pulses is about 50 times that for the unirradiated sample. This increase in the signal intensity in the Raman spectrum of the irradiated zone is attributed to the growth of the crystalline component in the TiO_2 film under the action of laser radiation.

For a 102-nm-thick TiO_2 film irradiated at the maximum fluence (64 pulses with 50.1 mJ/cm^2), the characteristic signal intensity exhibited an approximately threefold increase in comparison to that for the unirradiated sample. Similar behavior was also observed for the 513-nm-thick film, where the signal intensity upon irradiation at approximately the same fluence was increased by a factor of about 1.5.

Thus, the content of the crystalline phase in thin TiO_2 films significantly increases upon exposure to VUV laser radiation with λ = 193 nm. The effect of laser radiation strongly depends on the film thickness: the thicker the film, the less pronounced the laser action.

Laser-induced anatase–rutile phase transition. We have measured the Raman spectra in the 50–900 cm^{-1} range for the regions of films irradiated at a maximum laser pulse energy for each sample. The most interesting results are as follows. Figure 3 presents the Raman spectrum of a 70-nm-thick TiO_2 film exposed to 256 laser pulses at an energy density of 46.1 mJ/cm^2. For comparison, this figure also shows the spectrum of the same sample prior to irradiation and the spectra of rutile and anatase crystals. The anatase spectrum was measured in the (xx) polarization, which provides the maximum intensity at 399 and 516 cm^{-1}.

The data in Fig. 1 show evidence of the phase transition from anatase to rutile. This process is illustrated by the spectra measured at points *j* and *j*' of the same irradiated zone of the sample (see the inset to Fig. 3). As can be seen, the material modified by irradiation contains both phases, predominantly rutile. Differences between the compositions of central and peripheral regions of the irradiated zone are explained by the nonuniform distribution of intensity in the laser beam cross section: the radiation intensity is higher at the center than at the edge of the beam. A lower intensity results in a smaller fraction of the irradiated material being converted from anatase to rutile at point *j*' than at point *j* (where a considerable proportion of TiO_2 occurs in the rutile phase). For better illustration of the phase transition (and in view of the significant difference in the intensity of the characteristic Raman signals from the irradiated and unirradiated zones), all the Raman spectra of the 70-nm-thick film in Fig. 3 are normalized so as to provide equal heights of the peaks at 145 cm^{-1}. In the 102- and 513-nm-thick films, the phase transition from anatase to rutile was not observed.

Conclusion. The investigation of the structure of thin TiO_2 films grown by light-assisted molecular beam epitaxy showed evidence for an increase in the degree of crystallization with increasing film thickness. The exposure of these films to pulsed VUV radiation (193 nm, 20 ns) leads to the crystallization of the initial amorphous phase to anatase. The smaller the film thickness (i.e., the lower the initial degree of crystallization), the higher the efficiency of laser action. A further increase in the laser fluence (at a laser pulse energy density of 40–50 mJ/cm^2) for the thinnest (70 nm) film leads to the phase transition from anatase to rutile. This is the first observation of such a phase transition in initially amorphous TiO_2 films under the action of ArF excimer laser radiation. A comparison of the obtained results to the data reported in [8] showed that a decrease in the laser wavelength from 248 nm (for KrF laser [8]) to 193 nm (ArF laser, this study) leads to a significant decrease in the threshold energy for the phase transition.

REFERENCES

1. U. Diebold, Surf. Sci. Rep. **48**, 53 (2003).
2. P. F. Chauvy, C. Madore, and D. Landolt, Electrochem. Solid-State Lett. **2**, 123 (1999).
3. A. M. Peiro, J. Peral, C. Domonogo, *et al.*, Chem. Mat. **13**, 2567 (2001).
4. Landolt-Bornstein, *Numerical Data and Functional Relationships in Science and Technology* (Springer, Berlin, 1984), Group III, Vol. 17G, p. 413.
5. Y. Ichikawa, K. Setsune, S. Kawashima, and K. Kugimiya, Jpn. J. Appl. Phys., Part 2 **40**, L1054 (2001).
6. G. Benvenuti, PhD Thesis (EPFL, Lausanne, 2003).
7. P.-F. Chauvy, P. Hoffmann, and D. Landolt, Appl. Surf. Sci. **211**, 113 (2003).
8. T. D. Robert, L. D. Laude, V. M. Geskin, *et al.*, Thin Solid Films **440**, 268 (2003).
9. C. E. Morosanu, *Thin Films by Chemical Vapor Deposition* (Elsevier, Amsterdam, 1990).
10. L. I. Maissel and R. Glang, *Handbook of Thin Film Technology* (McGraw-Hill, New York, 1970; Sov. Radio, Moscow, 1977).
11. G. Benvenuti, E. Halary-Wagner, A. Brioude, and P. Hoffmann, Thin Solid Films **427**, 411 (2003).

Translated by P. Pozdeev

Technical Physics Letters, Vol. 31, No. 11, 2005, pp. 912–914. Translated from Pis'ma v Zhurnal Tekhnicheskoĭ Fiziki, Vol. 31, No. 21, 2005, pp. 24–29.

Effect of Ultrasonic Plastic Treatment on the Surface Structure and Phase State of Nickel Titanium

A. I. Lotkov*, A. A. Baturin, V. N. Grishkov, Zh. G. Kovalevskaya, and P. V. Kuznetsov

Institute of Strength Physics and Materials Science, Siberian Division, Russian Academy of Sciences, Tomsk, 634055 Russia

** e-mail: lotkov@ispms.tsc.ru*

Received June 20, 2005

Abstract—The influence of ultrasonic plastic treatment (UPT) on the relief, microstructure, and phase state of the surface of nickel titanium (TiNi) has been studied. The UPT leads to significant hardening, nanofragmentation, and a change in the phase state of the surface TiNi layer. *© 2005 Pleiades Publishing, Inc.*

The physical properties of metals and alloys are determined to a considerable extent by the structure (crystalline and granular) and phase state of the surface layer, as well as by the density and type of structural defects. As is known, reduction in the grain size to 100 nm and below leads to a significant increase in the yield stress and ultimate strength of alloys, including those based on intermetallic compounds and exhibiting the phenomena of shape memory and superelasticity, an example being offered by nickel titanium (TiNi) [1]. There are several methods for the formation of nanostructures in massive TiNi samples, in particular, equichannel angular pressing (ECAP) and 3D-forging [1]. The most effective methods of modification are based on deformation by high-pressure torsion [2] and severe plastic deformation (SPD) by rolling after ECAP [3]. The formation of nanostructured layers on the surface of alloys requires special processing techniques [4].

A promising method of surface treatment for the formation of submicrocrystalline and nanostructured surface layers is offered by ultrasonic plastic treatment (UPT) [5–7]. However, this method has never been used previously for the surface modification of shape memory materials in order to study the influence of modified layers on the properties of such materials. This Letter presents the first original results of our investigation of the influence of UPT on the microstructure, microhardness, and phase state of the surface layers of nickel titanium.

Experimental. The experiments were performed on a TiNi alloy with a nearly equiatomic composition, which is known to exhibit B2 $\longleftrightarrow$ B19' martensitic transformations on cooling and heating. The martensitic transformation start (M_1 and M_2) and finish (A_1 and A_2) temperatures for this alloy on cooling and heating, respectively, are as follows: M_1 = 340 K, M_2 = 313 K, A_1 = 360 K, and A_2 = 370 K. At T = 300 K, the samples possessed a martensite (B19') structure and exhibited a coarse-grain morphology with ~25 μm equiaxial grains. The samples had the shape of 1.8-mm-thick disks with a diameter of 30 mm and were preliminarily ground and then annealed for 1 h at 1073 K in vacuum at a residual gas pressure below 10^{-3} Pa. After annealing, the mechanically damaged outer surface layer was removed by chemical polishing to a depth of ~0.2 mm.

The source of ultrasonic oscillations was a UZG-0.2/22 acoustic generator operating at a frequency of 22.8 kHz. The sample surface was processed with an ultrasound-driven indenter having a spherical tip with a diameter of 5 mm made of a hard alloy (VK8). The indenter performed oscillations with an amplitude of 5–7 μm, being pressed to the sample surface at a normal load of 75 N [5]. The UPT was performed within a ring zone with outer and inner radii of 12 and 5 mm, respectively, on the surface of a disk sample. For this purpose, the disk was rotated at a circular frequency of 62 rpm and the indenter was shifted in the radial direction at a velocity of s = 0.05, 0.025, or 0.01 mm per turn.

The parameters of the mesorelief produced by the UPT were determined using a Micromeasure 3D Station profilometer, and the microstructure was studied by scanning tunneling microscopy (STM) on a CMM-2000T multimicroscope. The crystal structure and phase composition of samples upon UPT were studied by X-ray diffraction on a DRON-3M diffractometer using FeK_α radiation. The microhardness was measured using a PMT-3 device.

Results. The UPT led to a significant change in the surface morphology of samples, resulting in the appearance of a spiral mesorelief different from that of the chemically polished surface (Fig. 1). Data on the parameters of surface roughness in the initial and ultrasonically treated samples are presented in the table.

1063-7850/05/3111-0912$26.00 © 2005 Pleiades Publishing, Inc.

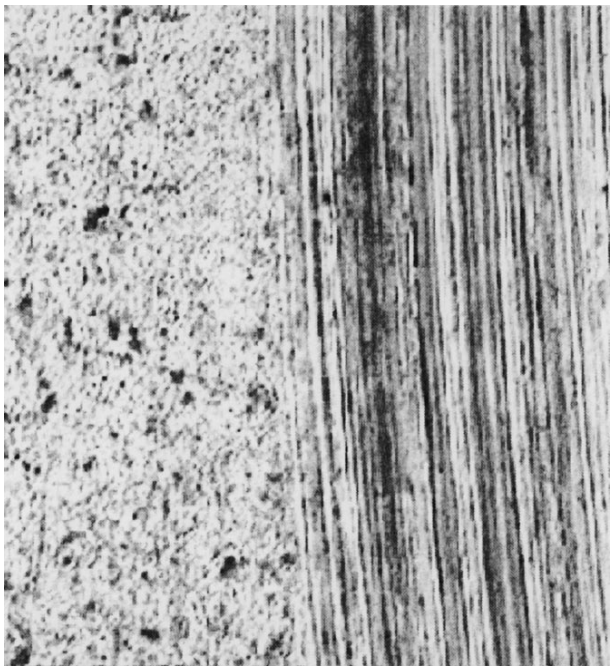

Fig. 1. Micrographs of the surface relief on a TiNi sample after chemical polishing (left-hand side) and upon UPT at s = 0.05 mm/turn (right-hand side) (magnification, ×200).

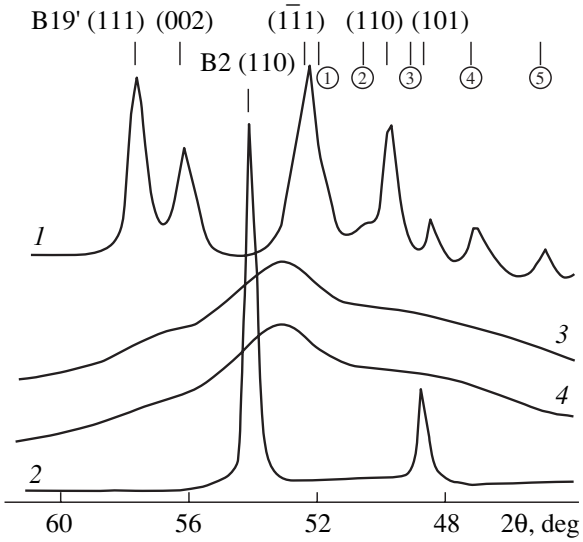

Fig. 2. Fragments of the X-ray diffraction patterns for TiNi alloy samples: (*1*, *2*) in the initial (chemically polished) state, measured at T = 296 and 360 K, respectively; (*3*, *4*) upon UPT at s = 0.05 mm/turn, measured at 296 K in the regions spaced by 4 and 6 mm, respectively, from the outer boundary of the processed ring zone. The area of scanned regions was 2.5×4 mm^2.

As can be seen from data in the table, both lateral (R_a) and vertical (R_z) roughness parameters are significantly reduced upon UPT (by 39 and 24%, respectively) as compared to the values observed for the same sample after chemical polishing. Note that the parameters of periodicity of the regular mesorelief are not directly proportional to the radial velocity of the indenter. At a constant sample rotation speed and a fixed radial velocity of the indenter, the "grooves" overlap and the frequency of impacts increases on approaching the central part of the sample. In order to elucidate the character of the resulting microrelief and to establish the laws of redistribution of the microvolumes of the deformed alloy, it is necessary to perform model experiments for determining the parameters of impact interactions between the indenter and the sample surface.

Discussion. The results of X-ray diffraction measurements showed that the UPT not only produced a regular mesorelief on the surface of samples but also changed the TiNi phase state in the most heavily strained surface layer (90% of the signal intensity measured using the FeK_α radiation in the angular interval 2θ = 44°–60° is due to the layer with a thickness of ~3.5 μm). The X-ray diffractograms of ultrasonically treated samples (Fig. 2) display a wide modulated diffraction profile formed by the broadened reflections of B19' martensite, narrow (110) reflections of the B2 phase, and probably a (003)–(112) doublet of the rhombohedral R-martensite (previously observed in strongly deformed TiNi alloys of nearly equiatomic composition [3]). Qualitatively similar X-ray diffractograms were observed in TiNi based binary alloys upon volume SPD deformation [3]. Such patterns are also characteristic of ultrafine powders obtained by methods of mechanoactivation [8], where the B2 phase of TiNi appears due to a decrease in the start temperatures (M_1 and M_2) for the B2 ⟷ B19' transformation. This decrease is caused by strain hardening accompanied by the formation of a submicrocrystalline or nanocrystalline structures.

It was reported [1] that TiNi based binary alloys with submicrocrystalline and nanocrystalline structures exhibit an increase (about twofold) in microhardness H_μ as compared to that of their coarse-grained counterparts. The results of microhardness measurements for our samples also showed that H_μ increased from 1.9 GPa in the initial alloy to 3.5–4.0 GPa upon the UPT. The thickness of a hardened surface layer (estimated from a change in size of the Vickers pyramid

The parameters of lateral (R_a) and vertical (R_z) roughness for TiNi samples upon UPT at different radial velocities s of the indenter

Surface treatment	s, mm/turn	R_a, μm	R_z, μm
Chemical polishing	–	0.353	3.05
Ultrasonic treatment	0.05	0.312	1.96
Ultrasonic treatment	0.01	0.215	2.2

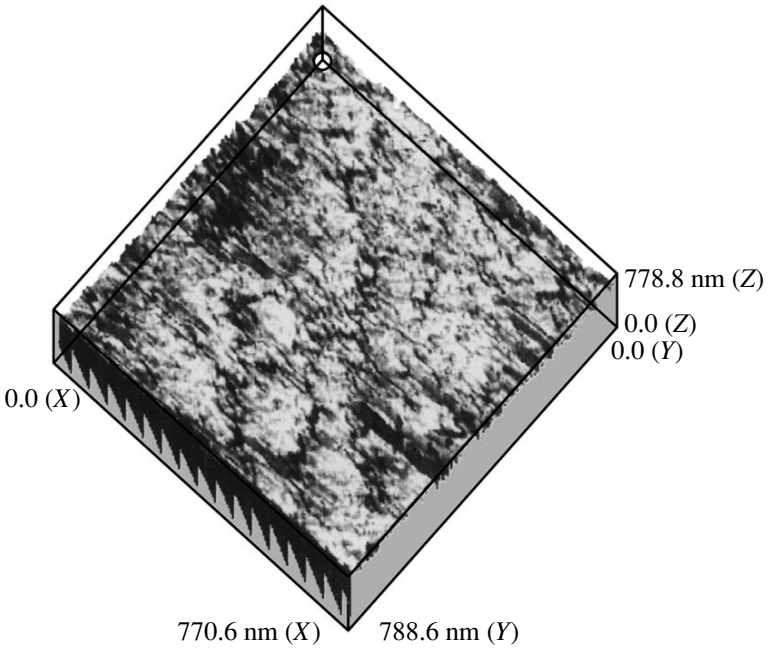

Fig. 3. STM image showing the microstructure of the TiNi surface upon UPD at s = 0.025 mm/turn, measured in the region 6 mm from the outer boundary of the processed ring zone.

indenter mark with increasing load) was no less than 8 μm (at this depth, the H_μ value exhibited a 10% decrease).

The results of STM examination of the microstructure of UPT-modified surface layers showed that this treatment leads to the formation of an ultrafine-grained structure including large regions in which the material occurs in a nanostructured state. Indeed, the STM images predominantly revealed fragments with an average size of 100 nm and below (Fig. 3).

The results of our investigation show that UPT is an effective method for the formation of nanostructured near-surface layers and their hardening in TiNi based alloys. However, for practical applications of this method, it is insufficient to study the material structure in the near-surface layer: it is no less important to characterize the structural-phase state and defectness of a deeper zone with a high level of long-range residual stresses. The thickness of such zones in steels and titanium reaches 200 μm [4–7]. The importance of such investigations is determined by the strong dependence of the sequence and temperatures of the martensitic transformations, shape memory parameters, and superelasticity characteristics in TiNi based alloys on the type and level of internal stresses.

Acknowledgments. This study was supported by the Siberian Division of the Russian Academy of Sciences (integration project no. 8.10) and by the program of basic research of the Presidium of the Russian Academy of Sciences (project no. 8).

REFERENCES

1. V. G. Pushin and R. Z. Valiev, in *Proceedings of the E-MRS Fall Meeting on Nanostructure Materials and Nanostructure Technology, Warsaw, 2002.*
2. T. Waitz, V. Kazykhanov, and H. P. Karnthaler, Acta Mater. **52**, 137 (2004).
3. V. N. Grishkov, A. I. Lotkov, E. F. Dudarev, *et al.*, Fiz. Mezomekh., Special Issue, Chap. 2, 26 (2004).
4. K. Lu and J. Lu, Mater. Sci. Eng. A **375–377**, 38 (2004).
5. V. E. Panin, V. A. Klimenov, Zh. G. Kovalevskaya, *et al.*, in *Proceedings of the International Conference on the Mechanics and Tribology of Transport Systems, Rostov-on-Don, 2003*, Vol. 2, pp. 195–198.
6. Yu. R. Kolobov, O. A. Kashin, E. F. Dudarev, *et al.*, Izv. Vyssh. Uchebn. Zaved., Fiz., No. 9, 45 (2000).
7. A. V. Panin, Fiz. Met. Metalloved. **98**, 109 (2004).
8. V. I. Itin, O. G. Terekhova, T. E. Ul'yanova, *et al.*, Pis'ma Zh. Tekh. Fiz. **26** (10), 73 (2000) [Tech. Phys. Lett. **26**, 436 (2000)].

Translated by P. Pozdeev

Technical Physics Letters, Vol. 31, No. 11, 2005, pp. 915–918. Translated from Pis'ma v Zhurnal Tekhnicheskoĭ Fiziki, Vol. 31, No. 21, 2005, pp. 30–36.

GaN Films Grown by Vapor-Phase Epitaxy in a Hydride–Chloride System on Si(111) Substrates with AlN Buffer Sublayers

V. N. Bessolov[a], V. Yu. Davydov[a], Yu. V. Zhilyaev[a], E. V. Konenkova[a], G. N. Mosina[a], S. D. Raevskiĭ[a], S. N. Rodin[a], Sh. Sharofidinov[a], M. P. Shcheglov[a], Hee Seok Park[b], and Masayoshi Koike[b]

[a] *Ioffe Physicotechnical Institute, Russian Academy of Sciences, St. Petersburg, 194021 Russia*
[b] *Samsung Electro-Mechanics Co. Ltd., Suwon, Gyunggi-Do, Korea*

Received May 17, 2005

Abstract—Oriented GaN layers with a thickness of about 10 μm have been grown by hydride–chloride vapor-phase epitaxy (HVPE) on Si(111) substrates with AlN buffer layers. The best samples are characterized by a halfwidth (FWHM) of the X-ray rocking curve of ω_θ = 3–4 mrad. The level of residual mechanical stresses in AlN buffer layers decreases with increasing temperature of epitaxial growth. The growth at 1080°C is accompanied by virtually complete relaxation of stresses caused by the lattice mismatch between AlN and Si. © *2005 Pleiades Publishing, Inc.*

Gallium nitride (GaN) epitaxial films have become an important semiconductor material for microwave electronics. For this reason, a currently important task is to obtain such films on silicon substrates, which would allow a significant reduction in the production cost and provide possibilities for integrating GaN-based optoelectronic devices into silicon-based microelectronics. Unfortunately, the growth of epitaxial GaN layers on single crystal silicon substrate encounters considerable difficulties: first, because of the significant differences in the lattice parameters and thermal expansion coefficients of these materials and, second, because of the active interaction of the silicon surface with ammonium (with the formation of SiN_x) in the stage of nucleation of the epitaxial layer (epilayer). One possible way to avoid these difficulties is related to the use of intermediate layers (sub- or buffer layers) deposited on the surface of silicon substrates. In recent years, this approach has been successfully employed for the growth of GaN films by molecular beam epitaxy (MBE) and metalorganic chemical vapor deposition (MOCVD) on AlAs [1], HfN [2], Ga_2O_3 [3], Al_2O_3 [4], and AlN [5] sublayers and intermediate AlGaN/GaN superlattices [6].

The method of hydride–chloride vapor phase epitaxy (HVPE) is characterized by high growth rates and is predominantly used for obtaining bulk (>100 μm thick) GaN layers, in most cases on sapphire substrates. However, it was reported that relatively thin GaN films can also be obtained by HVPE on gallium arsenide [7] and silicon [8, 9] substrates with AlN sublayers deposited by RF sputtering.

This paper reports the HVPE growth of oriented epitaxial GaN films on Si(111) substrates with AlN sublayers. The AlN layers were grown on preliminarily cleaned 2-inch (50 mm) Si(111) wafers rotated in a flow of hydrogen at a rate of 60 rpm. The ratio of the H_2/NH_3 flow rates in the course of AlN growth was 2 : 1, the substrate temperature was varied in the interval from 800 to 1100°C, and the time of exposure in the AlN growth zone was 1–20 min. The subsequent growth of 10-μm-thick GaN epilayers was carried out for 60 min at 950°C on substrates covered by AlN buffer layers with a thickness of 30–300 nm.

In order to elucidate the details of the formation of AlN buffer layers and to evaluate the quality of GaN epilayers, we have performed a comparative study of the structures of two types, AlN/Si(111) and GaN/AlN/Si(111). The samples were characterized by methods of Raman spectroscopy, transmission electron microscopy (TEM), and X-ray diffraction.

Figure 1 shows the typical Raman spectra measured in the region of the E_2 (high) phonon mode for AlN layers grown by HVPE at various temperatures on Si(111) substrates. For comparison, we also present the spectrum of a high-quality unstressed 5-μm-thick AlN layer grown by MOCVD on a sapphire (Al_2O_3) substrate. Data on the full width at half maximum (FWHM) of the observed E_2 (high) phonon peak and its spectral position ω for AlN films of various thicknesses h grown for the same period of time t at different temperatures (T_{growth}) are presented in Table 1 in comparison to the values for a thick unstressed AlN layer on Al_2O_3.

1063-7850/05/3111-0915$26.00 © 2005 Pleiades Publishing, Inc.

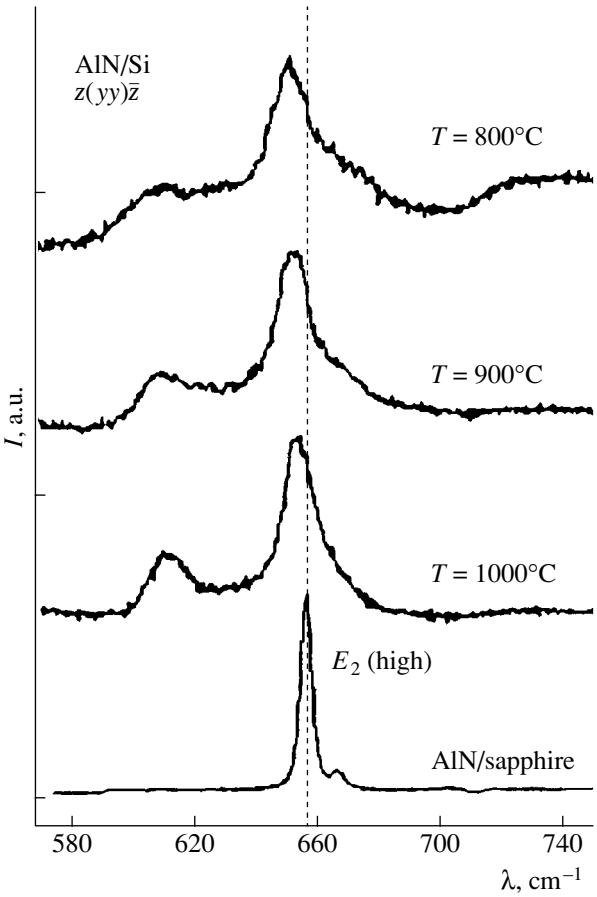

Fig. 1. The typical Raman spectra measured in the region of the E_2 (high) phonon mode for AlN layers grown by HVPE on Si(111) substrates at various temperatures (in comparison to the spectrum of a thick unstressed AlN layer grown on sapphire).

As can be seen from the data in Table 1, the peaks of the E_2 (high) phonon mode in the Raman spectra of AlN/Si(111) epilayers are shifted toward lower frequencies as compared to the ω value for the unstressed AlN layer on Al_2O_3. This behavior is evidence for the presence of tensile stresses in AlN in the plane parallel to the substrate, while variation of the shift is indicative

Table 1. The frequencies and halfwidths of the E_2 (high) phonon peaks in the Raman spectra of AlN layers grown at various temperatures on Si(111) substrates (in comparison to the values for a thick AlN layer on Al_2O_3)

	E_2 (high), ω, cm^{-1}	FWHM, cm^{-1}	T_{growth}, °C	t, min	h, nm
AlN/Si	654.5	12.4	1000	10	~1650
AlN/Si	652.4	11.3	900	10	1000
AlN/Si	651.2	12.6	800	10	870
AlN/Al_2O_3	657.6	3.5	–	–	–

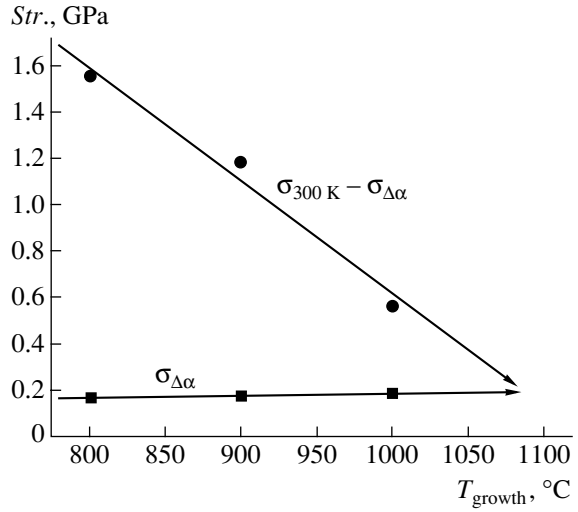

Fig. 2. Plots of the thermal stresses $\sigma_{\Delta\alpha}$ and elastic lattice-mismatch stresses $\sigma_{(300\ K)}$–$\sigma_{\Delta\alpha}$ versus growth temperature for AlN layers on Si(111) substrates.

of different values of the residual strain. The existence of residual stresses in AlN layers grown on Si(111) is quite natural, because the lattice parameter a in AlN is smaller, while its thermal expansion coefficient is greater than the corresponding values for Si(111). This difference results in the deformation of a growing layer at $T = T_{growth}$, which still increases upon cooling from T_{growth} to room temperature. We estimated the residual strain ε_{300} in AlN sublayers using a model of biaxial straining and assuming that the shift of the phonon peak is proportional to this strain: $\Delta\omega_\gamma = K_\gamma\varepsilon_{300}$ [10]. The coefficient of proportionality K_γ was taken from [11]. The resulting estimates of room-temperature stresses σ_{300} in AlN layers on Si(111) are given in Table 2.

Table 2 also presents the values of the elastic thermal stress $\sigma_{\Delta\alpha}$ calculated using the formula [12]

$$\sigma_{\Delta\alpha} = \frac{E_{AlN}}{1-\nu_{AlN}}\frac{\Delta\alpha\Delta T}{1+\dfrac{E_{AlN}(1-\nu_{Si})h}{E_{Si}(1-\nu_{AlN})H}},$$

where h and H are the thicknesses of the AlN layer and Si substrate, respectively; E and ν are the Young's moduli and the Poisson ratios of AlN and Si; $\Delta T = T_{growth} - 300$ is the temperature interval of cooling (°C); and $\Delta\alpha$

Table 2. The estimates of residual stresses in AlN layers grown at various temperatures on Si(111) substrates

T_{growth}, °C	$\sigma_{300\ K}$, GPa	$\sigma_{\Delta\alpha}$, GPa	σ_{growth}, GPa
800	1.71	0.16	1.55
900	1.35	0.17	1.18
1000	0.74	0.18	0.56

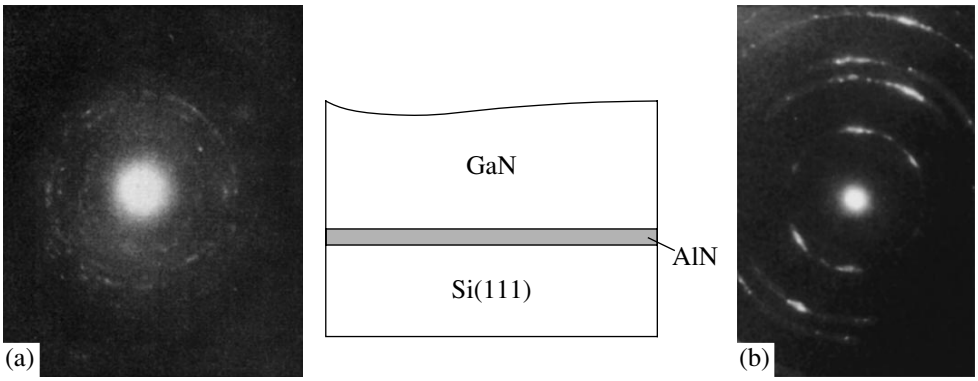

Fig. 3. The patterns of electron microdiffraction in the transmission mode showing the AlN sublayer structure in the regions of the (a) AlN/Si and (b) AlN/GaN interfaces of GaN/AlN/Si(111) heterostructures.

is the difference of the thermal expansion coefficients of AlN and Si. As is known, nucleation and multiplication of dislocations in crystals take place when the stresses exceed a certain critical level σ_{cr}. It is commonly accepted that thermal stresses in most heterostructures (at least, at temperatures below half of the melting temperature) exhibit no relaxation and are manifested by room-temperature elastic deformation [13]. Assuming this statement to be valid, we can estimate the residual stresses σ_{growth} for AlN/Si at the temperature of epitaxial growth as

$$\sigma_{growth} = \sigma_{300\,K} - \sigma_{\Delta\alpha}.$$

As can be seen, an increase in the temperature of epitaxial growth of AlN is accompanied by a decrease in the elastic stress σ_{growth}. As a result, the elastic strain caused by the lattice mismatch between the AlN layer and Si substrate exhibits almost complete relaxation for the layers grown at a temperature of about 1080°C (Fig. 2).

The crystal structure of GaN epilayers was studied by means of X-ray diffraction measured on a three-crystal X-ray diffractometer using CuK_α radiation. The X-ray rocking cures were obtained for two Bragg reflections—symmetric (0002) and asymmetric (1124)—in the regimes of two-crystal (ω scan) and three-crystal (ω–2ω scan) diffraction. The results of these measurements (including the reflection half-widths and the average lattice parameters $\langle a \rangle$ and $\langle c \rangle$) are presented in Table 3. The values of the crystal lattice deformation in the grown layer were determined by comparison to the parameters of nondeformed GaN [14].

Figure 3 shows the patterns of electron microdiffraction measured in the transmission mode for GaN/AlN/Si(111) heterostructures with different thicknesses of the AlN sublayer. As can be seen, the 30-nm-thick sublayer has a polycrystalline structure, while the pattern observed for the 300-nm thick sublayer (at the AlN/GaN interface) exhibits a coalescence texture characteristic of the azimuthal orientation of grains. For this reason, the GaN films in all heterostructures with AlN sublayer thicknesses below 100 nm also had a polycrystalline structure, whereas in the structures with AlN sublayer thicknesses above 250 nm, the GaN layers were oriented and had the lattice parameters indicated in Table 3.

The results of our investigation agree with the published data [15], according to which the AlN layers grown by MOCVD on sapphire initially possess a polycrystalline structure, but the subsequent annealing accompanied by coalescence leads to the formation of oriented films. In the case of high-temperature (T_{growth} = 1080°C) HVPE on a Si substrate, an almost polycrystalline AlN island film is also formed at the initial growth stage and then transforms (via island growth and coalescence) into a layer with a degree of crystal orientation sufficient for the subsequent growth of a substrate-oriented GaN epilayer.

Thus, we succeeded in obtaining HVPE-grown oriented GaN epilayers with a thickness of about 10 μm on

Table 3. Parameters of the X-ray diffraction pattern and the crystal structure of GaN epilayers grown by HVPE on Si(111) substrates with GaN sublayers

	$hk \cdot 1$	ω_θ	$\omega_{\theta/2\theta}$	θ_B, deg	c (5.1850 Å) a (3.1892 Å)	Δc (Å) Δa (Å)
GaN/AlN/Si	(0002)	660″	45″	17.2814	5.1859	+0.0009
	(1124)	780″	–	49.9694	3.1898	+0.0006

Si(111) substrates with intermediate thin elastically stressed AlN buffer layers.

Acknowledgments. This study was supported in part by the Russian Foundation for Basic Research (project nos. 03-03-32503 and 04-02-17635) and the Samsung Electro-Mechanics Co. Ltd. (contract N/66/1-2004). One of the authors (E.V.K.) also gratefully acknowledges financial support from the Russian Science Support Foundation.

REFERENCES

1. A. Strittmatter *et al.*, Appl. Phys. Lett. **74**, 1242 (1999).
2. R. Armitage, Q. Yang, H. Feick, *et al.*, Appl. Phys. Lett. **81**, 1450 (2002).
3. Ying-Ge Yang *et al.*, Physica B **325**, 230 (2003).
4. A. Wakahara *et al.*, J. Cryst. Growth **236**, 21 (2002).
5. B. S. Zhang *et al.*, J. Cryst. Growth **258**, 34 (2003).
6. Seong-Hwan Jang and Cheul-Ro Lee, J. Cryst. Growth **253**, 64 (2003).
7. K. Motoki *et al.*, Jpn. J. Appl. Phys. **40**, L140 (2001).
8. S. T. Kim, Y. J. Lee, S. H. Chung, and D. C. Moon, Semicond. Sci. Technol. **14**, 156 (1999).
9. P. W. Yu, C. S. Park, and S. T. Kim, J. Appl. Phys. **89**, 1692 (2001).
10. V. Yu. Davydov, N. S. Averkiev, I. N. Goncharuk, *et al.*, J. Appl. Phys. **82**, 5097 (1997).
11. M. Kuball, M. Hayes, A. D. Prins, *et al.*, Appl. Phys. Lett. **78**, 724 (2001).
12. P. R. Tavernier, B. Imer, S. P. DenBaars, and D. R. Clarke, Appl. Phys. Lett. **85**, 4630 (2004).
13. M. G. Mil'vidskiĭ and V. B. Osvenskiĭ, Kristallografiya **22**, 431 (1977) [Sov. Phys. Crystallogr. **22**, 246 (1977)].
14. T. Detchprohm *et al.*, Jpn. J. Appl. Phys. **31**, L1454 (1992).
15. I. Akasaki *et al.*, J. Cryst. Growth **98**, 209 (1998).

Translated by P. Pozdeev

Technical Physics Letters, Vol. 31, No. 11, 2005, pp. 919–921. Translated from Pis'ma v Zhurnal Tekhnicheskoĭ Fiziki, Vol. 31, No. 21, 2005, pp. 37–42.

Modeling the Instability of the Boundary of a Dielectric Liquid with a Free Surface Charge

K. E. Bobrov, N. M. Zubarev*, and V. G. Suvorov

Institute of Electrophysics, Ural Division, Russian Academy of Sciences, Yekaterinburg, Russia

** e-mail: nick@ami.uran.ru*

Received April 12, 2005

Abstract—We have numerically modeled the development of instability of the boundary of a nonviscous dielectric liquid with a free surface charge occurring in an external electric field and compared the behavior of this system in the two limiting cases, whereby the surface charge produces complete screening of the field above and below the surface. Although the linearized equations of motion in the two cases coincide, the scenarios of instability development are substantially different, which is indicative of the determining role of nonlinearity in this process. © *2005 Pleiades Publishing, Inc.*

As is known, the surface of a dielectric liquid bearing a free surface charge becomes unstable as soon as the control parameter (representing the sum of the energy densities of the electric field above and below the surface) exceeds a certain threshold [1, 2]. In the linear stage of the development of this instability, the system features exponential growth of the amplitude of periodic surface perturbations. A necessary condition of the applicability of the linearized equations of motion is that the perturbation amplitude is small as compared to the characteristic wavelength. Evidently, this condition is unavoidably violated within a finite time, after which the further evolution of the system will be determined by nonlinear processes.

This Letter presents the results of numerical modeling of the dynamics of the system in the nonlinear stage of the development of instability, that is, when the amplitude of perturbations on the initially flat surface becomes comparable with the characteristic wavelength (which can be more than ten times greater than the surface curvature radius).

Let us consider a dielectric liquid occurring in an external electric field between flat electrodes. The liquid surface in the unperturbed state is assumed to be flat, coinciding with the horizontal plane $z = 0$, and the electric field vector is normal to this surface (i.e., the field is directed along the z axis). Restricting consideration to the axisymmetric case, deviations of the liquid boundary from the initial flat surface can be described by the function $\eta(r, t)$, so that the shape of the perturbed surface is determined by the equation $z = \eta(r, t)$. For the sake of simplicity, the distance h from the upper electrode to the liquid surface is set equal to the depth of the liquid layer and to the distance from the axis of symmetry to the side boundaries of the region occupied by the liquid.

Assuming the liquid to be ideal (i.e., incompressible) and its motion to be potential, the Laplace equation describing the velocity field potential Φ for axisymmetric perturbations of the liquid surface can be written as

$$\Phi_{rr} + r^{-1}\Phi_r + \Phi_{zz} = 0. \tag{1}$$

This equation has to be solved jointly with the boundary conditions

$$\begin{gathered}\Phi_t = \frac{\Phi_r^2 + \Phi_z^2}{2} = \frac{P_E}{\rho} + \frac{\alpha/\rho}{\sqrt{1+\eta_r^2}}\left(\frac{\eta_{rr}}{1+\eta_r^2} + \frac{\eta_r}{r}\right), \\ z = \eta(r, t), \quad \Phi_z\big|_{z=-h} = 0, \quad \Phi_r\big|_{r=0} = 0, \\ \Phi_r\big|_{r=h} = 0,\end{gathered} \tag{2}$$

where α is the coefficient of surface tension, ρ is the density of the liquid, and P_E is the electrostatic pressure.

The temporal evolution of the free liquid surface is determined by the kinematic relation

$$\eta_t = \Phi_z - \eta_r\Phi_r, \quad z = \eta(r, t), \tag{3}$$

and the electrostatic pressure at the charged surface of the liquid is described by the expression

$$8\pi P_E = (\varphi_r^2 + \varphi_z^2)_{z=\eta+0} - \varepsilon(\varphi_r^2 + \varphi_z^2)_{z=\eta-0}, \tag{4}$$

where φ is the potential of the electric field and ε is the permittivity of the liquid.

Below, we will compare the two limiting cases. Case A corresponds to the limit whereby the liquid surface bears positive ions which produce complete

1063-7850/05/3111-0919$26.00

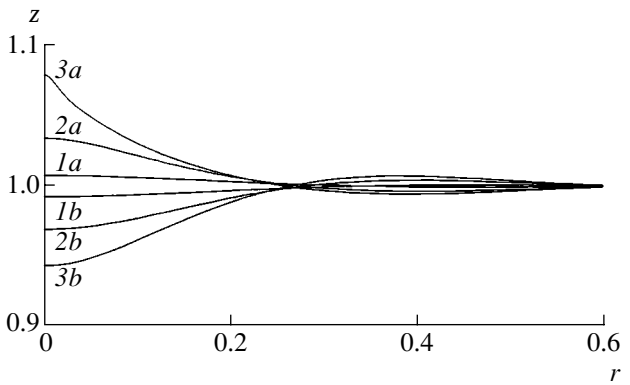

Fig. 1. The results of numerical modeling of the development of instability of a dielectric liquid surface in an external electric field in the two limiting cases, whereby the surface charge produces complete screening of the field below (case A, curves *1a*–*3a*) and above (case B, curves *1b*–*3b*) the surface, for the moments of dimensionless time t = 0.08 (*1a*, *1b*), 0.11 (*2a*, *2b*), and 0.11825 (*3a*, *3b*).

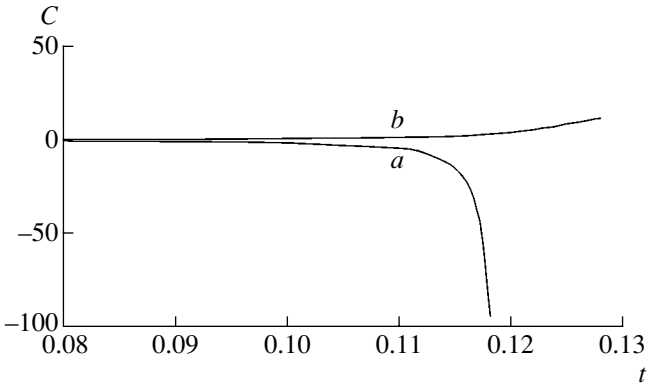

Fig. 2. Temporal evolution of the liquid surface curvature C at the axis of symmetry in the limiting cases A (curve *a*) and B (curve *b*).

screening of the field in the liquid (i.e., below the surface), whereas the limiting case B corresponds to the surface charged with electrons screening the field above the boundary. Such situations are realized, for example, in liquid helium and hydrogen with strongly charged surfaces [3, 4]. Note that, for these fluids, $\varepsilon \approx 1$ in Eq. (4). A situation analogous to case A also takes place in the ideal conducting liquid, since the field does not penetrate into such a medium because of screening by the induced surface charge. The influence of nonlinearity on the evolution of the surface of a liquid conductor was previously studied by analytical methods (see, e.g., [5, 6]).

The electric field potential φ in the axisymmetric case under consideration obeys the Laplace equation

$$\varphi_{rr} + r^{-1}\varphi_r + \varphi_{zz} = 0. \quad (5)$$

This equation has to be supplemented with the condition of equipotentiality of the liquid surface and solved together with the appropriate boundary conditions on the electrodes, the side boundaries, and the axis of symmetry:

$$\varphi|_{z=\eta} = U, \quad \varphi|_{z=+h} = 0, \quad \text{(case A)}$$

$$\varphi|_{z=\eta} = 0, \quad \varphi|_{z=-h} = U, \quad \text{(case B)}$$

$$\varphi_r|_{r=0} = 0, \quad \varphi_r|_{r=h} = 0,$$

where U is the potential difference.

The dispersion relation corresponding to the problem under consideration for the plane surface waves in the short-wavelength limit ($kh \gg 1$) is as follows:

$$\omega^2 = \frac{\alpha}{\rho}k^3 - \frac{U^2}{4\pi\rho h^2}k^2,$$

where ω is the circular frequency and k is the wavenumber. It should be noted that the form of this relation is independent of the sign of the surface charge—that is, this relation is valid in both limiting cases A and B. Therefore, the development of instability in the linear stage proceeds according to the sane scenario and the differences can be related only to the nonlinearities entering into the dynamic and kinematic boundary conditions (2) and (3), respectively.

For modeling the dynamics of the charged liquid surface, it is convenient to introduce dimensionless variables by using h as the unit of length and $\sqrt{h^3\rho/\alpha}$ at the unit of time. A numerical solution of the Laplace equations (1) and (5) with the corresponding boundary conditions was obtained by mapping the initial computational domain onto the rectangular domain

$$\{r, z\} \longrightarrow \{r, (z \pm 1)/(\eta(r, t) \pm 1)\},$$

and assuming that $U^2 = 144\pi\alpha h$ (which corresponds to an electric field strength above the critical value necessary for the development of instability).

The results of numerical calculations are presented in Fig. 1. In case A (curves *1a*–*3a*) the system exhibits a tendency to the formation of a cone-shaped cusp (see also [7], where the analogous model calculations were performed for a viscous conducting liquid). In accordance with the hypothesis formulated in [8], the formation of cone-shaped surface features with an apical angle of 98.6° is determined by self-similar solutions of the equations of hydrodynamics. In case B, for which the initial perturbation was set with the opposite sign, this tendency is not observed: the surface is "pulled" downward without forming a cusp (for linearized equations, the surface evolution would follow the scenario of case A to within the substitution $\eta \longrightarrow -\eta$). This asymmetry is emphasized in Fig. 2, which shows the

temporal evolution of the curvature of the liquid boundary at the axis of symmetry. In case A, this curvature tends to infinity within a finite time, whereas, in case B, the curvature exhibits slow growth without singularities.

We can suggest that case B is characterized by the growth of the surface depression toward the lower electrode. The possibility of this scenario in the development of instability was previously pointed out in [9], where exact partial solutions of the equations of motion obtained in the limiting case of a strong external field represented paraboloidal depressions in the charged surface of a dielectric liquid, which propagated into the liquid at a constant velocity.

The qualitative difference in behavior of the liquid boundary on the developed stages of instability development in the limiting cases A and B is indicative of a determining role of nonlinearity in electrohydrodynamic processes in the presence of supercritical electric fields.

Acknowledgments. This study was supported in part by the basic research program "Mathematical Methods in Nonlinear Dynamics" of the Presidium of the Russian Academy of Sciences and by the "Dynasty" Foundation of Noncommercial Programs.

REFERENCES

1. J. R. Melcher, *Field-Coupled Surface Waves* (MIT Press, Cambridge, 1963).
2. L. P. Gor'kov and D. M. Chernikova, Pis'ma Zh. Tekh. Fiz. **18**, 119 (1973) [Sov. Tech. Phys. Lett. **18**, 68 (1973)].
3. V. P. Volodin, M. S. Khaĭkin, and V. S. Edel'man, Pis'ma Zh. Éksp. Teor. Fiz. **26**, 707 (1977) [JETP Lett. **26**, 543 (1977)].
4. V. Shikin and P. Leiderer, Fiz. Nizk. Temp. **23**, 624 (1997) [Low Temp. Phys. **23**, 468 (1997)].
5. N. M. Zubareva and O. V. Zubarev, Zh. Tekh. Fiz. **71** (7), 21 (2001) [Tech. Phys. **46**, 806 (2001)].
6. A. I. Grigor'ev, S. O. Shiryaeva, D. F. Belonozhko, and A. V. Klimov, Zh. Tekh. Fiz. **75** (2), 19 (2005) [Tech. Phys. **50**, 158 (2005)].
7. V. G. Suvorov and N. M. Zubarev, J. Phys. D: Appl. Phys. **37**, 289 (2004).
8. N. M. Zubarev, Pis'ma Zh. Éksp. Teor. Fiz. **73**, 613 (2001) [JETP Lett. **73**, 544 (2001)].
9. N. M. Zubarev, Pis'ma Zh. Tekh. Fiz. **27** (8), 8 (2001) [Tech. Phys. Lett. **27**, 311 (2001)].

Translated by P. Pozdeev

Technical Physics Letters, Vol. 31, No. 11, 2005, pp. 922–924. Translated from Pis'ma v Zhurnal Tekhnicheskoĭ Fiziki, Vol. 31, No. 21, 2005, pp. 43–48.

Inversion of the Electron Energy Distribution in Hollow-Cathode Glow Discharge in Nitrogen–Sulfur Hexafluoride Gas Mixture

V. Yu. Bazhenov, A. G. Kalyuzhnaya, I. A. Soloshenko, A. F. Tarasenko, A. G. Terent'eva, V. V. Tsiolko, and A. I. Shchedrin*

Institute of Physics, National Academy of Sciences of Ukraine, Kiev, Ukraine

** e-mail: shched@iop.kiev.ua*

Received June 22, 2005

Abstract—The electron energy distribution function (EDF) in a hollow-cathode glow discharge in nitrogen–sulfur hexafluoride (N_2–SF_6) gas mixture has been studied by experimental and theoretical methods. On adding a small amount of SF_6 to N_2, the density of electrons in the energy interval (2–4 eV) of the EDF inversion increases by approximately one order of magnitude. © *2005 Pleiades Publishing, Inc.*

The phenomenon of inverse electron energy distribution in low-temperature plasma is of considerable interest because such media can be used for obtaining inverse populations of the atomic and molecular electron levels (see, e.g., [1] and references therein). The results of our previous experimental and theoretical investigations [2] showed that such distributions can be realized in hollow-cathode glow discharge in nitrogen. In such cases, the region of inversion of a stationary electron energy distribution function (EDF) occurs in the interval from 2 to 4 eV, which corresponds to characteristic thresholds of the electron excitation of gas molecules. The EDF inversion in pure nitrogen is related to certain features of the interaction of N_2 molecules with electrons. Indeed, electrons with the energies ε = 4–7 eV exhibit no inelastic collisions with N_2 molecules and rather slightly lose energy via inelastic collisions with these molecules. As a result, the density of electrons with energies in the indicated interval tends to increase. In the region of 2–4 eV, electrons quite rapidly lose their energy for the excitation of vibrational levels of N_2 molecules, which results in the appearance of a trough in the corresponding region of the EDF. Unfortunately, the absolute majority of electrons occur in the region of lower energies (ε < 2 eV), and their density in the region of EDF inversion is rather insignificant.

Previously [1], we theoretically predicted the possibility of increasing the fraction of electrons in the region of EDF inversion by adding a small amount of an electronegative gas (SF_6 of CCl_4) to nitrogen. It was suggested that the attachment of low-energy electrons to the electronegative molecules would lead to a decrease in the number of such electrons in the discharge and, accordingly, to an increase in the relative fraction of electrons with higher energies including those corresponding to the interval of inversion. Other inelastic interactions of electrons with the electronegative admixture do not significantly affect the EDF because of the low concentration of this gas.

This paper presents the results of experimental investigations of the EDF in a mixture of N_2 and SF_6 and theoretical calculations using parameters corresponding to the experimental conditions. It will be shown that adding a small amount of SF_6 to N_2 significantly increases the fraction of electrons in the interval of the EDF inversion.

The EDF was experimentally determined using a setup described in detail elsewhere [2]. The setup was based on a cylindrical vacuum chamber with a diameter of 280 mm and a height of 400 mm, which also played the role of a hollow cathode for the glow discharge. The chamber was evacuated with a mechanical pump to a minimum residual pressure of $\approx 2 \times 10^{-3}$ Torr. Since the pumping rate was virtually independent of the residual pressure in the interval from 2×10^{-3} to 2×10^{-1} Torr, the working mixture of N_2 and SF_6 in the chamber was prepared using the following procedure. Initially, the chamber was evacuated to the minimum residual pressure. Then, the necessary amount of SF_6 was introduced and the chamber was filled with nitrogen to a total pressure of 0.1 Torr. The partial pressure of SF_6 in our experiments was varied within $(1–10) \times 10^{-3}$ Torr, which amounted to 1–10% of the total gas pressure. The plasma density and the EDF were measured with the aid of Langmuir probes, which were made of a tungsten wire with a diameter of 50–100 μm and had a charge collector length of 10–12 mm. The probes could be moved in the radial and axial direction in the chamber. In order to eliminate the influence of surface contaminations on the current–voltage (*I–V*) characteristic

1063-7850/05/3111-0922$26.00

of the probe, it was cleaned after each measurement by heating to 800°C in vacuum.

The *I–V* curves were measured using an automated system controlled by a personal computer provided with special software. The system provided programmed variation of the probe current (which was set with an accuracy of 0.1 μA) and simultaneously measured the probe potential (relative to the anode), the anode voltage, and the discharge current. The current increment at each step was automatically calculated using a special algorithm so as to optimize the signal-to-noise ratio in the entire experimental range (the number of steps used for the measurement of each *I–V* curve was 1500–2000). The measurements in a stroboscopic regime were performed at a frequency of 100 Hz and synchronized with the power supply variations in order to eliminate their influence on the experimental results. The measured signals were gated over a 1-μs period of time. The delay of this period relative to the onset of the power supply voltage halfwave was selected so as to optimize the signal-to-noise ratio. The results of measurements were digitized and stored in the computer memory in the form of an *I–V* curve for a given discharge current and voltage. The measurements at a fixed set of parameters were repeated up to 30 times and the obtained data averaged. The plasma potential was determined as corresponding to the point where the second derivative of the probe current with respect to the voltage is zero, and the electron density in the plasma was calculated using the value of the saturation current of electrons to the probe. The density of negative ions in the plasma was determined using the method described in [3].

During the EDF measurements, the systematic error in the region of small electron energies (≤0.2–0.3 eV) was decreased using a method based on the combination of the first and second derivatives of the electron current to the probe [4]. In this case, the EFD had the following form:

$$f(eV) \approx \frac{1}{C_0}\left(j_e''(eV) - j_e'(eV)\frac{\Psi}{eV}\right), \qquad (1)$$

where C_0 is the normalization constant, j_e is the density of the electron current to the probe, V is the probe potential relative to the plasma potential, $\psi = ac_i/\gamma_0\lambda$ is the diffusion parameter of the probe, a is the probe diameter, λ is the electron mean free path, $c_i = \ln(\pi l/4a)$, l is the probe length, and $\gamma_0 = 4/3$ (for $a \ll \lambda$). For determining the derivatives, we used the total current to the probe instead of the electron current, because estimates showed that the contribution of ion current to the total probe current can be ignored in the range of electron energies up to ~10 eV.

The partial pressure of SF_6 in our experiments did not exceed 6×10^{-3} Torr. Higher densities of this gas in the discharge plasma led to the excitation of intense relaxation oscillations with frequencies in the range from 10^2 to 10^5 Hz, which hindered correct measurements of the plasma characteristics.

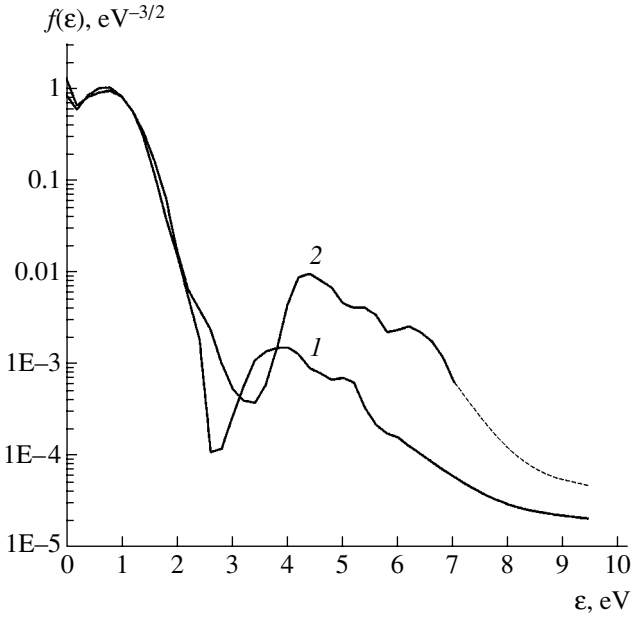

Fig. 1. The experimental EDFs measured in hollow-cathode glow discharge in (*1*) pure nitrogen and (*2*) an N_2–SF_6 mixture with the ratio of components 1 : 0.057 at a total pressure of 0.1 Torr.

The introduction of SF_6 into nitrogen led to an increase in the discharge voltage. In pure nitrogen, the voltage drop across the discharge was 520–540 V at a discharge current of 1 A. In a mixture of nitrogen with SF_6 at a partial pressure of 6×10^{-3} Torr, the discharge voltage for this current reached 700–800 V. The plasma density at this SF_6 pressure was about 2×10^{10} cm^{-3}, and the longitudinal inhomogeneity of this value did not exceed 10%. The density of negative ions in this case was several times greater than the electron density. The presence of SF_6 also led to an increase in the electric field strength in the plasma: at a partial pressure of SF_6 on the level of $(5–6) \times 10^{-3}$ Torr, the longitudinal electric field strength reached ~0.1 V/cm, which was almost ten times as strong as the value in the case of pure nitrogen. The radial electric field strength E_r also exhibited an increase, and the radial field profile became more complicated as compared to that in the pure nitrogen plasma. The maximum radial field strength (0.4–0.7 V/cm) was observed in the paraxial region and at the periphery of the discharge, whereas in the intermediate region this value did not exceed 0.1–0.2 V/cm.

Figure 1 (curve *2*) shows the EDF measured with a probe occurring at a distance of 70 mm from the chamber axis for a discharge in N_2–SF_6 mixture with an SF_6 partial pressure of about 5.7×10^{-3} Torr. For comparison, we also present an EDF measured under otherwise

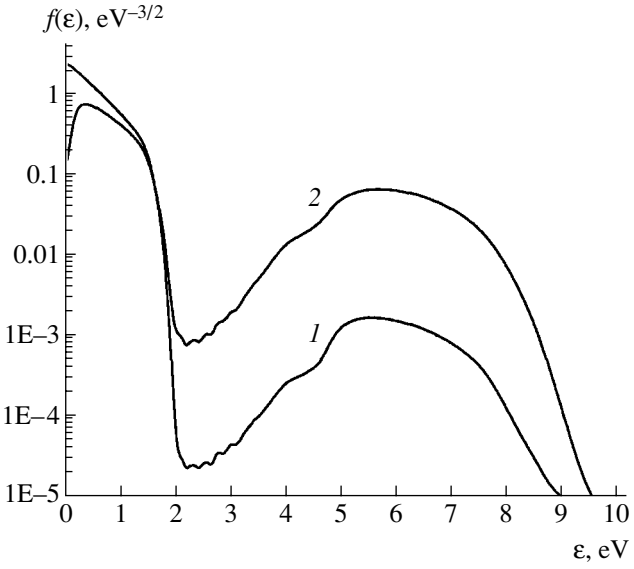

Fig. 2. Theoretical EDFs numerically calculated for a hollow-cathode glow discharge in (*1*) pure nitrogen and (*2*) an N_2–SF_6 mixture with the ratio of components 1 : 0.05 at a total pressure of 0.1 Torr.

identical conditions in pure nitrogen plasma (curve *1*). As can be seen from these data, the presence of the electronegative additive in the mixture leads to a significant increase in the electron density in the region of inversion, so that the number of electrons with energies in this interval increases by approximately one order of magnitude.

For a numerical calculation of the EDF, we solved the Boltzmann equation in a two-term approximation with allowance for the elastic and inelastic collisions of electrons with neutrals, the electron–electron scattering, and the gas ionization by a beam of high-energy electrons. Detailed description of the scheme of calculations and the interaction of electrons with molecules of the working gas mixture was presented in [1, 2]. The EDF was calculated for N_2–SF_6 mixtures with various ratios of components and a total pressure of 0.1 Torr. In agreement with experimental data, the electric field strength in the discharge region was set equal to 0.1 V/cm and the electron density was taken equal to $\sim 10^{10}$ cm^{-3}. Figure 2 shows the EDFs calculated for pure nitrogen and an N_2–SF_6 mixture with the ratio of components 1 : 0.05. As can be seen from a comparison of Figs. 1 and 2, the results of calculations qualitatively agree with the experimental data, according to which adding several percent of SF_6 to N_2 significantly increases the density of electrons in the energy interval of the EDF inversion.

REFERENCES

1. A. G. Kalyuzhnaya, A. V. Ryabtsev, and A. I. Shchedrin, Zh. Tekh. Fiz. **73** (1), 42 (2003) [Tech. Phys. **48**, 38 (2003)].
2. V. Yu. Bazhenov, A. V. Ryabtsev, I. A. Soloshenko, *et al.*, Fiz. Plazmy **27**, 859 (2001) [Plasma Phys. Rep. **27**, 813 (2001)].
3. M. Shindo, S. Uchino, and R. Ichiki, Rev. Sci. Instrum. **72**, 2288 (2001).
4. N. A. Gorbunov, A. N. Kopytov, and F. E. Latyshev, Zh. Tekh. Fiz. **72** (8), 7 (2002) [Tech. Phys. **47**, 940 (2002)].

Translated by P. Pozdeev

Technical Physics Letters, Vol. 31, No. 11, 2005, pp. 925–928. Translated from Pis'ma v Zhurnal Tekhnicheskoĭ Fiziki, Vol. 31, No. 21, 2005, pp. 49–57.

Analytical Solution of the Problem of Second-Order Thermal Slip with Allowance for the Rotational Degrees of Freedom of Gas Molecules

A. V. Latyshev, V. N. Popov*, and A. A. Yushkanov

Pomorskiĭ State University, Arkhangelsk, Russia

** e-mail: popov.vasily@pomorsu.ru*

Received June 6, 2005

Abstract—Exact analytical methods are applied to description of second-order thermal slip for a polyatomic gas (with the number of atoms in the molecule $N \geq 2$) with allowance for the rotational degrees of freedom of the gas molecules. The thermal slip coefficients are determined for some particular molecular gases. It is shown that the second-order thermal slip coefficients of polyatomic gases depend on the Prandtl number. *© 2005 Pleiades Publishing, Inc.*

The presence of gradients of hydrodynamic quantities (temperature, mass flow rate, concentration) in a rarefied gas leads to the phenomenon of gas slip along streamlined surfaces [1]. The problem of gas slip on a plane solid surface has been studied in sufficient detail using exact analytical methods for both mono- and polyatomic gases (with the number of atoms in the molecule $N \leq 2$). In contrast, the problem of obtaining exact analytical solutions in the case of a polyatomic gas slipping round a curved surface is still open.

The aim of this study was to obtain exact analytical solutions to the problem of second-order thermal slip for a polyatomic gas. The approach is based on the Bhatnagar–Gross–Kruck (BGK) model of the Boltzmann kinetic equation, which is generalized to include the rotational degrees of freedom of the gas molecules [2]. It is assumed that the vibrational degrees of freedom are frozen, while the rotational motions are described in terms of the classical kinetic theory of gases.

For monoatomic gases, exact analytical solutions of the problem under consideration have been obtained previously within the framework of the BGK [3] and ES [4] models of the Boltzmann kinetic equation and using the Williams model [5].

1. Formulation of the problem. Main equations. Consider a spherical aerosol particle suspended in a rarefied molecular gas with an inhomogeneous temperature field. Let a spherical coordinate system (r, θ, φ) be related to the center of curvature of the particle, with the polar axis oriented parallel to the temperature gradient in the region far from the particle surface. The inhomogeneity of the temperature distribution in the gas volume implies that the $\partial T/\partial r$ and $\partial T/\partial\theta$ values are nonzero. Let us assume that the temperature gradient component normal to the particle surface slowly varies along the surface. Then, the second-order derivative $\partial^2 T/\partial r\partial\theta$ is nonzero, which is just what accounts for the so-called second-order thermal slip.

In what follows, the above derivatives are assumed to be small. In this case, the problem admits linearization, whereby the distribution of gas molecules with respect to coordinates and velocities can be represented as

$$f = f^{(0)}[1 + Y(\mathbf{r}, \mathbf{C}, \nu)].$$

Here, $f^{(0)}$ is the equilibrium distribution function in the gas volume far from the aerosol particle surface; $\mathbf{r}_0 = 2\lambda\mathbf{r}/(\sqrt{\pi}\mathrm{Pr})$ is the dimensional radius vector; λ is the mean free path of gas molecules, which is related to the kinematic viscosity by the relation $\lambda = \nu_g(\pi m/2k_\mathrm{B}T)^{1/2}$; Pr is the Prandtl number; $\mathbf{C} = \mathbf{v}\sqrt{m/2k_\mathrm{B}T_\mathrm{w}}$; $\nu = \omega\sqrt{J/2k_\mathrm{B}T_\mathrm{w}}$; $\mathbf{v}$ and ω are the translational velocity and rotational frequency of the gas molecules, respectively; T_w is the particle (wall) surface temperature; k_B is the Boltzmann constant; m and J are the mass and the moment of inertia of a gas molecule, respectively; and $Y(\mathbf{r}, \mathbf{C}, \nu)$ is a solution of the following equation [2]:

$$C_r\frac{\partial Y}{\partial r} + Y(\mathbf{r}, \mathbf{C}, \nu) + C_\theta\frac{\partial Y}{\partial\theta} + \frac{C_\varphi}{\sin\theta}\frac{\partial Y}{\partial\varphi} + (C_\theta^2 + C_\varphi^2)\frac{\partial Y}{\partial C_r}$$
$$+ (C_\varphi^2\cot\theta - C_rC_\theta)\frac{\partial Y}{\partial C_\theta} - (C_\varphi C_\theta\cot\theta + C_rC_\varphi)\frac{\partial Y}{\partial C_\varphi}$$
$$= \int k(\mathbf{C}, \nu; \mathbf{C}', \nu')Y(\mathbf{r}, \mathbf{C}', \nu')d\Omega, \qquad (1.1)$$

where $l = 2$ and $d\Omega = 2\pi^{-3/2}\exp(-C^2 - \nu^2)\nu d\nu d^3C$ for a diatomic gas; $l = 5/2$ and $d\Omega = \pi^{-3}\exp(-C^2 - \nu^2)d^3\nu d^3C$

for a polyatomic gas ($N \geq 2$); $k = 4\mathrm{Kn}/(\sqrt{\pi}\mathrm{Pr})$ for the isothermal slip; $k = 2\mathrm{Kn}/(\sqrt{\pi}\mathrm{Pr})$ for the thermal slip; $\mathrm{Kn} = \lambda/R_0$ is the Knudsen number; R_0 is the dimensional radius of the aerosol particle, and

$$k(\mathbf{C}, \nu; \mathbf{C}', \nu') = 1 + 2\mathbf{C}\mathbf{C}' + \frac{1}{l+1/2}(C^2 + \nu^2 - l - 1/2)(C^2 + \nu'^{1/2} - l - 1/2).$$

Let us seek a solution to Eq. (1.1) in the form of an expansion with respect to the small parameter k:

$$Y(\mathbf{r}, \mathbf{C}, \nu) = Y_1(\mathbf{r}, \mathbf{C}, \nu) + kY_2(\mathbf{r}, \mathbf{C}, \nu) + \ldots. \quad (1.2)$$

With allowance for this expression, the tangential component U_θ of the dimensionless mass flow velocity can be also expanded into series with respect to k and written as

$$U_\theta = U_\theta^{(1)} + kU_\theta^2 + \ldots.$$

Substituting expression (1.2) into Eq. (1.1) and equating the coefficients at k, we eventually obtain the following equation for the function $Y_2(\mathbf{r}, \mathbf{C}, \nu)$:

$$C_r\frac{\partial Y_2}{\partial x} + Y_2(x, \mathbf{C}, \nu) = \int k(\mathbf{C}, \nu; \mathbf{C}', \nu')Y_2(x, \mathbf{C}', \nu')d\Omega - \left[(C_\theta^2 + C_\varphi^2)\frac{\partial Y_1}{\partial C_r} + (C_\varphi^2\cot\theta - C_rC_\theta)\frac{\partial Y_1}{\partial C_\theta} - (C_\varphi C_\theta\cot\theta + C_rC_\varphi)\frac{\partial Y_1}{\partial C_\varphi}\right] - C_\theta\frac{\partial Y_1}{\partial\theta}. \quad (1.3)$$

In this equation,

$$Y_1(x, \mathbf{C}, \nu) = [Z_1(x, C_r) + \gamma(C^2 + \nu^2 - l - 1/2)Z_2(x, C_r)]K_T, \quad (1.4)$$

$Z_1(x, C_r)$ and $Z_2(x, C_r)$ coincide with the distribution functions constructed in solving the problem of temperature jump [2],

$$Z(x, \mu) = \int_0^\infty \exp(-x/\eta)F(\eta, \mu)A(\eta)d\eta,$$

$$F(\eta, \mu) = \eta P\frac{1}{\eta - \mu}E + \exp(\eta^2)B(\eta)\delta(\eta - \mu),$$

$$B(\eta) = \lambda(\eta)E + \frac{1}{2l}\begin{bmatrix} 1/2 - \eta^2 & 1/2 + l - \eta^2 \\ 1 & 1 \end{bmatrix},$$

$$\lambda(z) = 1 + \frac{1}{\sqrt{\pi}}z\int_{-\infty}^\infty \frac{\exp(-\mu^2)d\mu}{\mu - z},$$

$$A(\eta) = [A_1(\eta), A_2(\eta)]^t,$$

$$Z(x, \mu) = [Z_1(x, \mu)Z_2(x, \mu)]^t.$$

Here, $\lambda(z)$ is the Cercignani dispersion function, E is the unit matrix, $x = r - R_0$, Px^{-1} is the distribution of the principal value of the integral of x^{-1}, $\delta(x)$ is the Dirac delta function, $\gamma^2 = 1/(l + 1/2)$, $K_T = (1/T_w)(\partial T/\partial r)$, and the symbol t denotes transposition.

Let us seek a solution to Eq. (1.3) in the form of the expansion

$$Y_2(x, \mathbf{C}, \nu) = C_\theta\psi(x, C_r, \nu) + \sum_k b_k(C_\theta, C_\varphi)\psi_k(x, C_r, \nu), \quad (1.5)$$

where C_θ together with $b_k(C_\theta, C_\varphi)$ form a complete set of orthogonal polynomials in the velocity space. By the orthogonality of $g(C)$ and $f(C)$ in velocity space, we imply zero of the integral $\int \exp(-C^2)g(C)f(C)d\mathbf{C}$.

Substituting expressions (1.4) and (1.5) into Eq. (1.3), multiplying the obtained relations by $\exp(-C_\theta^2 - C_\varphi^2)$, and integrating with respect to C_θ and C_φ from $-\infty$ to $+\infty$, we eventually arrive at the following equation for the function $\psi(x, \mu, \nu)$:

$$\mu\frac{\partial\psi}{\partial x} + \psi(x, x, \mu, \nu) = \int \exp(-\mu'^2 - \nu'^2)\psi(x, \mu', \nu')dgd\mu' - k_T[Z_1(x, \mu) + \gamma(\mu^2 + \nu^2 - l + 3/2)Z_2(x, \mu)], \quad (1.6)$$

where $dg = 2\pi^{-1/2}\nu d\nu$ for a diatomic gas, $dg = 2\pi^{-1/2}d^3\nu$ for a polyatomic gas, $\mu = C_r$, and $k_T = (1/T_w)(\partial^2 T/\partial r\partial\theta)$.

A solution to Eq. (1.6) will be found in the following form:

$$\psi(x, \mu, \nu) = \varphi(x, \mu) + (\nu^2 - l + 1)\varphi_1(x, \mu). \quad (1.7)$$

Upon substituting expression (1.7) into Eq. (1.6), we multiply the obtained relation by $\nu\exp(-\nu^2)$ and integrate the obtained relation with respect to ν from 0 to $+\infty$ for a diatomic gas; for a polyatomic gas, we multiply the result of substitution by $\exp(-\nu^2)$ and integrate the obtained relation with respect to ν_i from $-\infty$ to $+\infty$.

In both cases, we eventually arrive at the same set of equations for the functions $\varphi(x, \mu)$ and $\psi_1(x, \mu)$:

$$\mu\frac{\partial\varphi}{\partial x} + \varphi(x, \mu) = \frac{1}{\sqrt{\pi}}\int_{-\infty}^{\infty}\exp(-\tau^2)\varphi(x, \tau)d\tau - k_T[Z_1(x, \mu) + \gamma(\mu^2 + 1/2)Z_2(x, \mu)], \quad (1.8)$$
$$\mu\frac{\partial\varphi_1}{\partial x} + \varphi_1(x, \mu) = -k_T\gamma Z_2(x, \mu).$$

Assuming that the gas molecules exhibit diffuse reflection from the surface of the aerosol particle, we can write the boundary conditions for $\varphi(x, \mu)$ and $\psi_1(x, \mu)$ as follows:

$$\varphi(0, \mu) = -2U_0, \quad \mu \geq 0, \quad \varphi(+\infty, \mu) = 0, \quad (1.9)$$
$$\varphi_1(0, \mu) = 0, \quad \mu \geq 0, \quad \varphi_1(+\infty, \mu) = 0.$$

Since the unknown slip velocity enters only into the boundary conditions for $\varphi(x, \mu)$, we may restrict the consideration to Eq. (1.8) with the boundary conditions (1.9).

Introducing the notation

$$a(\eta, \mu) = a_1(\eta) + \mu^2 a_2(\eta), \quad (1.10)$$

$$a_1(\eta) = k_T\left[A_1(\eta) + \frac{1}{2}\gamma A_2(\eta)\right], \quad a_2(\eta) = k_T\gamma A_2(\eta), \quad (1.11)$$

$$b(\mu) = \left[a(\mu, \mu)\lambda(\mu) + \frac{1}{2l}k_T(A_1(\mu) + \gamma(l+1)A_2(\mu))\right]\exp(\mu^2), \quad (1.12)$$

we can rewrite Eq. (1.8) as follows:

$$\mu\frac{\partial\varphi}{\partial x} + \varphi(x, \mu) = \frac{1}{\sqrt{\pi}}\int_{-\infty}^{\infty}\exp(-\tau^2)\varphi(x, \tau)d\tau - \int_0^{\infty}\exp(-x/\eta)\frac{\eta a(\eta, \mu)}{\eta - \mu}d\eta - \exp(-x/\mu)b(\mu)\Theta_+(\mu). \quad (1.13)$$

Thus, the solution of the problem of determining the second-order thermal slip velocity of a rarefied polyatomic gas on a curved surface with allowance for the rotational degrees of freedom of the gas molecules reduces to the solution of Eq. (1.13) with the boundary condition (1.9).

2. Calculation of the second-order thermal slip velocity. Equation (1.13) with the boundary condition (1.9) fully coincides with an analogous equation and the corresponding boundary condition derived previously [3]. Using the solution found in [3], we obtain

$$U_0 = \frac{k_T}{2\sqrt{\pi}}\left[\int_0^{\infty}\eta^2 a_2(\eta)d\eta + 2\int_0^{\infty}\frac{\eta a_3(\eta)}{X(-\eta)}d\eta\right], \quad a_3(\eta) = a_1(\eta) + \left[\eta\lambda(\eta)a(\eta, \eta) - \frac{1}{\sqrt{\pi}}\eta b(\eta)\exp(-\eta^2)\right]'. \quad (2.1)$$

Then, taking into account relations (1.10)–(1.12) and calculating the second integral in Eq. (2.1) by parts, we eventually obtain

$$U_0 = \frac{k_T}{2\sqrt{\pi}}\left[\gamma\int_0^{\infty}\eta^2 A_2(\eta)d\eta + 2\int_0^{\infty}\eta[(1 + 1/l)A_1(\eta) + \gamma(3/2 + 1/l)A_2(\eta)]\frac{d\eta}{X(-\eta)} + \frac{1}{l}\int_0^{\infty}\eta^2[A_1(\eta) + \gamma(l+1)A_2(\eta)]\frac{d\eta}{X(-\eta)}\frac{1}{\pi}\times\int_0^{\infty}\frac{\theta(\tau) - \pi}{(\tau + \eta)^2}d\tau\right]. \quad (2.2)$$

Here [2],

$$\mu A_j(\mu) = \frac{1}{2\sqrt{\pi}}\left[(X_{j1}^+(\mu) - X_{j1}^-(\mu))\left(\alpha_1\mu + \alpha_0 + \frac{\alpha - 1}{\mu - \mu_0}\right) + (X_{j2}^+(\mu) - X_{j2}(\mu))\left(\beta_1\mu + \beta_0 + \frac{\beta_{-1}}{\mu - \mu_0}\right)\right], \quad i = 1, 2,$$

$$X_{11}^+(\mu) - X_{11}^-(\mu) = \mp\left[\left(1 - \frac{\mu^2 + 1/2}{r(\mu)}\right)U_1(\mu)\sin\theta_1(\mu) + \left(1 + \frac{\mu^2 + 1/2}{r(\mu)}\right)U_2(\mu)\sin\theta_2(\mu)\right],$$

$$X_{12}^+(\mu) - X_{12}^-(\mu) = \pm\frac{2\gamma(\mu^2 - l - 1/2)}{r(\mu)} \times [U_1(\mu)\sin\theta_1(\mu) - U_2(\mu)\sin\theta_2(\mu)],$$

$$X_{21}^+(\mu) - X_{21}^-(\mu) = \mp\frac{2}{\gamma r(\mu)}[U_1(\mu)\sin\theta_1(\mu) - U_2(\mu)\sin\theta_2(\mu)],$$

$$X_{22}^{+}(\mu) - X_{22}^{-}(\mu)$$
$$= \mp\left[\left(1 + \frac{\mu^2 + 1/2}{r(\mu)}\right)U_1(\mu)\sin\theta_1(\mu)\right.$$
$$\left. + \left(1 + \frac{\mu^2 - 1/2}{r(\mu)}\right)U_2(\mu)\sin\theta_2(\mu)\right]$$

(where the upper sign refers to the interval $0 \le \mu \le \mu_0$ and the lower sign, to the interval $\mu > \mu_0$),

$$U_j(z) = \exp[-A(z) + (-1)^j r(z)(B(z) + R(z))],$$
$$j = 1, 2,$$
$$A(z) = \frac{1}{2\pi}\int_0^\infty \frac{a(\tau)d\tau}{\tau - z}, \quad B(z) = \frac{1}{2\pi}\int_0^\infty \frac{b(\tau)}{r(\tau)}\frac{d\tau}{\tau - z},$$
$$R(z) = \int_0^{\mu_0} \frac{d\tau}{r(\tau)(\tau - z)},$$
$$a(\tau) = \theta_1(\tau) + \theta_2(\tau) - 2\pi, \quad b(\tau) = \theta_1(\tau) - \theta_2(\tau),$$
$$\theta_\alpha(\mu) = \frac{\pi}{2} - \arctan\frac{\Omega_\alpha(\mu)}{\sqrt{\pi}\mu\exp(-\mu^2)}, \quad \alpha = 1, 2,$$
$$\Omega_\alpha(z) = \lambda(z) - \frac{1}{10}\left[z^2 - \frac{3}{2} + (-1)^\alpha r(z)\right], \quad \alpha = 1, 2,$$
$$r(z) = \sqrt{q(z)}, \quad q(z) = \left(z^2 - \frac{3}{2}\right)^2 + 4l,$$

μ_0 is determined from the equation

$$\frac{1}{2\pi}\int_0^\infty \frac{b(\tau)d\tau}{r(\tau)} + \int_0^{\mu_0}\frac{d\tau}{r(\tau)} = 0,$$
$$\alpha_1 = q_0, \quad \beta_1 = -q_0/\gamma, \quad \beta_{-1} = \mu_0^2\frac{\alpha_1 - \delta\beta_1}{\alpha - \delta},$$
$$\alpha_{-1} = \alpha\beta_{-1}, \quad \alpha = -\frac{1}{2}\gamma[r(\mu_0) + \mu_0^2 + 1/2],$$
$$\beta_0 = -\mu_0\beta_1 + \frac{2\mu_0(\alpha_1 - \delta\beta_1) - \alpha'\beta_{-1}}{\alpha - \delta},$$
$$\delta = \frac{1}{2}\gamma[r(0) - 1/2], \quad \alpha' = -\mu_0\gamma\frac{\mu_0^2 - 3/2 + r(\mu_0)}{\alpha - \delta},$$
$$\alpha_0 = \delta\beta_0 + \mu_0(\alpha_1 - \delta\beta_1),$$
$$X(z) = \frac{1}{z}\exp\left\{-\frac{1}{\pi}\int_0^\infty \frac{(\theta(\tau) - \pi)d\tau}{\tau - z}\right\},$$
$$\theta(\tau) = \frac{\pi}{2} - \arctan\frac{\lambda(\tau)}{\sqrt{\pi}\tau\exp(-\tau^2)},$$
$$q_0 = \exp\left[-\frac{1}{2\pi}\int_0^\infty \frac{\tau b(\tau)d\tau}{r(\tau)} - \int_0^{\mu_0}\frac{\tau d\tau}{r(\tau)}\right].$$

The results of our numerical calculations gave $U_0 = 0.5740k_T$ for diatomic gases and $U_0 = 0.5873k_T$ for polyatomic gases.

Passing to dimensional variables and using the form commonly accepted in the theory of rarefied gases (see, e.g., [3]), we can write

$$u_\theta|_S = K_{Ts}\beta_R \mathrm{Kn}\,\nu_g\frac{1}{T_w}\frac{\partial^2 T}{\partial r_0 \partial\theta}\bigg|_S.$$

Taking into account that $K_{Ts} = 0.7662/\mathrm{Pr}$ for polyatomic gases [2], we obtain $\beta_R = 1.6934/\mathrm{Pr}$ for diatomic gases and $\beta_R = 1.7299/\mathrm{Pr}$ for polyatomic gases. In particular, for Cl_2 (Pr = 0.64) and CO (Pr = 0.74), the second-order thermal slip coefficients are 2.64459 and 2.2884, respectively. For monoatomic gases, β_R is independent of the Prandtl number and, for example, in the BGK model this value is 2.3524 [3]. The scatter of results is on the order of 2.7–11.1%.

Conclusions. Using exact analytical methods, we have calculated the second-order thermal slip velocity for polyatomic gases with allowance for the rotational degrees of freedom of the gas molecules. It is established that the second-order thermal slip coefficient of such gases substantially depend on the Prandtl number. The results obtained with allowance for the rotational degrees of freedom significantly differ from those obtained with neglect of the internal structure of molecules

REFERENCES

1. E. M. Lifshitz and L. P. Pitaevskii, *Physical Kinetics* (Nauka, Moscow, 1979; Pergamon Press, Oxford, 1981).
2. A. V. Latyshev and A. A. Yushkanov, Prikl. Mat. Mekh. **66**, 845 (2002).
3. A. V. Latyshev, V. N. Popov, and A. A. Yushkanov, Izv. Ross. Akad. Nauk, Mekh. Zhidk. Gaza, No. 3, 183 (2003).
4. A. V. Latyshev, V. N. Popov, and A. A. Yushkanov, Sib. Zh. Industrial. Mat. **6** (13), 60 (2003).
5. A. V. Latyshev, V. N. Popov, and A. A. Yushkanov, Teplofiz. Vys. Temp., No. 6, 132 (2003).

Translated by P. Pozdeev

Technical Physics Letters, Vol. 31, No. 11, 2005, pp. 929–931. Translated from Pis'ma v Zhurnal Tekhnicheskoĭ Fiziki, Vol. 31, No. 21, 2005, pp. 58–63.

Ultra-Wideband Data Transmission with Double Spectral Processing of Noise Waveforms

V. I. Kalinin

Institute of Radio Engineering and Electronics (Fryazino Branch), Russian Academy of Sciences, Fryazino, Moscow oblast, Russia

e-mail: val.kalinin@mail.ru

Received May 17, 2005

Abstract—The process of ultra-wideband (UWB) data transmission with double spectral processing of noise waveforms is considered. A new method of code spectral modulation based on the interference of perfectly incoherent noise waveforms is proposed. The possibility of compressing UWB noise waveforms by means of real-time double spectral processing with subsequent extraction of transmitted data has been experimentally demonstrated. © *2005 Pleiades Publishing, Inc.*

Investigations into new methods of modulation, encoding, and spectral compression of ultra-wideband (UWB) signals are of considerable importance for the development of high-speed data transmission systems [1–3]. Wireless UWB communication systems possess high potential information capacity [1] and are characterized by highly reliable data transmission under the conditions of multibeam propagation [2, 4, 5]. An increase in the number of active channels and a decrease in the level of mutual interference are achieved due to the orthogonal chaotic coding in multiaddress systems with spread spectrum [5]. A promising approach to hidden data transmission is based on the nonlinear systems with chaotic dynamics [6–8].

This Letter presents the results of experimental investigations into a new method of UWB data transmission with code spectral modulation.

According to the proposed method, the data are transmitted with continuous noise waveforms of low power spectrum density in the 3.1–4.1 GHz frequency band. The UWB signal $n(t)$ from a noise generator is separated into two parts, one of which is used as a reference signal. The other part of the $n(t)$ signal is delayed in a two-section delay line either for the time T_1 = 33.7 ns upon arrival of the informative symbol (binary code) "1" or for the time T_0 = 18 ns upon arrival of the binary code "0." It is assumed that the transmission coefficients $H_{1,0} = h_{1,0}\exp(i\theta_{1,0})$ and the delay times $T_{1,0}$ in the sections of the delay line are independent of the noise frequency f in a frequency band Δf. The delayed and reference signals are subjected to mutual interference in the transmitter. In a linear summator, the reference signal $n(t)$ is added to the noise signal delayed for T_1 or T_0, depending on the binary code (1 or 0, respectively):

$$z_{1,0}(t) = n(t) + H_{1,0}n(t - T_{1,0}). \quad (1)$$

The power spectrum of signal (1) over the period of arrival t_a of the binary codes is calculated as

$$\hat{S}_z(f) = \hat{S}_n(f)[1 + h_{1,0}^2 + 2h_{1,0}\cos(2\pi f T_{1,0} + \theta_{1,0})], \quad (2)$$

where $\hat{S}_n(f)$ is the estimated power spectrum of the initial noise signal $n(t)$ over the time of analysis equal to t_a.

The summation of perfectly incoherent noise waveforms takes place when the relative delay (T_1 or T_0) between the reference and delayed signals is significantly greater than the coherence time $\tau_c \approx 1/(\Delta f)$ of the UWB signal $n(t)$:

$$T_{1,0} \gg \tau_c \quad \text{or} \quad T_{1,0}\Delta f \gg 1. \quad (3)$$

In the case of the interference of perfectly incoherent noise waveforms [2, 10, 11] under conditions (3), the spectral density (2) is modulated by a harmonic function of frequency f with periodicity scale $\delta f_{1,0}(t) = 1/T_{1,0}$.

Figures 1a and 1b show examples of the power spectra of noise waveforms entering the transmission line upon the arrival of binary codes 0 and 1. In the experiment, the spectra were measured by a panoramic spectrum analyzer with a high-frequency resolution of 1.0 MHz. The frequency band of the continuous noise signal was Δf = 1000 MHz and the coherence time was on the order of $\tau_c \approx 1/(\Delta f)$ = 1 ns. The noise signal was subjected to spectral modulation with a period of δf_0 in the case of binary code 0 (Fig. 1a) and with a period of δf_1 in the case of binary code 1 (Fig. 1a). The nonuniform depth of spectral modulation as a function of the current frequency in Figs. 1a and 1b results from the

1063-7850/05/3111-0929$26.00 © 2005 Pleiades Publishing, Inc.

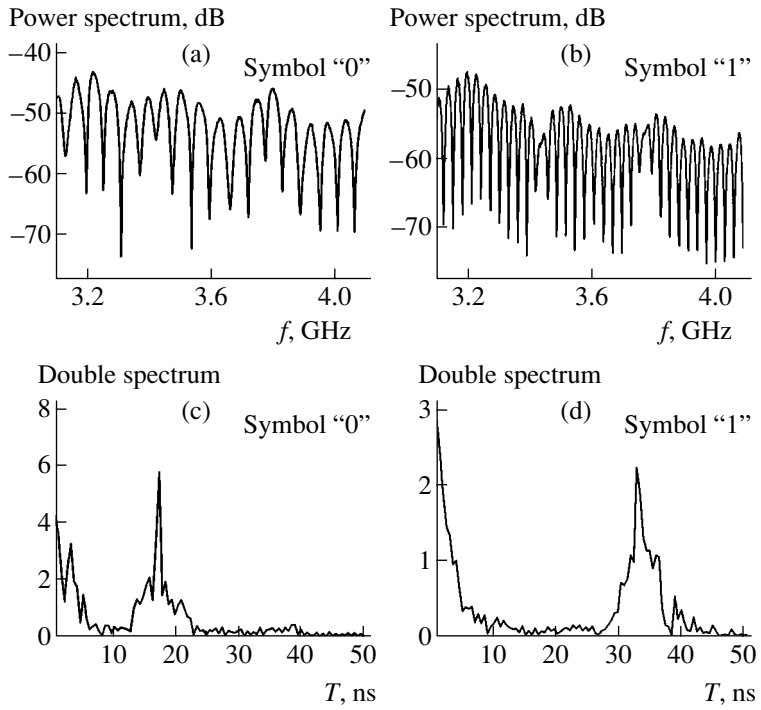

Fig. 1. Double spectral processing of UWB noise waveforms with code spectral modulation: (a, b) experimental power spectra with the spectral modulation periods δf_0 = 55.56 MHz and δf_1 = 29.67 MHz corresponding to the transmitted binary codes 0 and 1, respectively; (c, d) secondary UWB noise waveforms containing correlation peaks with the shifts T_0 = 18 ns and T_1 = 33.7 ns for the reproduction of data bits 0 and 1, respectively.

frequency and dispersion distortions of the UWB signal in the experimental circuit.

It should be noted that a wide frequency band ($\Delta f \gg \delta f_{1,0}$) of the noise waveforms is a necessary condition for realization of the proposed method of digital data transmission [2, 11]. The interference of perfectly incoherent noise waveforms is accompanied by the appearance of numerous interference maxima and minima in the resulting spectra (Figs 1a and 1b). The UWB noise waveforms with a periodic code spectral modulation (2) enter the wireless transmission line in accordance with the sequence of binary codes.

The optimal receipt of the continuous noise waveforms consists in the measurement of the function of mutual correlation with the reference signal over a period of one data bit [8]. An alternative method consists in the measurement of the mutual correlation function for the delayed noise waveforms in the frequency domain by means of the double spectral processing described in [2, 4, 10, 11].

According to this method, the received noise waveforms are subjected to spectral compression via double spectral processing. Using a panoramic spectrum analyzer, the estimated power spectrum (2) is measured over a finite time of analysis t_a for each binary code (Figs. 1a and 1b). The spectral estimate (2) is a random value whose dispersion is inversely proportional to the length t_a of the period of signal averaging [2]. The interval t_a of the arrival of binary codes determines the rate $U = 1/t_a$ of data transmission in the channel. An increase in the data transmission rate $U = 1/t_a$ leads to the corresponding growth of the dispersion of the estimated spectrum (2). The maximum possible data transmission rate is determined by the frequency band Δf of the carrier noise signal and by the permissible dispersion of the estimated spectrum [1, 2].

Determination of the correlation function with allowance for expression (2) for the spectrum of received signals is performed by a high-speed digital Fourier processor [2, 4]. Using the inverse Fourier transform of the power spectrum (2), the autocorrelation function of the received UWB signal is calculated according to the Wiener–Khinchin theorem as

$$\hat{R}_z(\tau) = 4\pi k^2 \int_0^\infty \hat{S}_z(f)\cos(2\pi f\tau)df$$
$$= 2k^2[\hat{R}_n(\tau) + \hat{R}_n(\tau - T_{1,0}) + \hat{R}_n(\tau + T_{1,0})]. \quad (4)$$

Here, k is the coefficient of signal attenuation in the transmission line and $R_n(\tau)$ is the autocorrelation function of the initial UWB noise signal $n(t)$. The estimate (4) is valid for the equal transmission coefficients $h_1 = h_0 = 1$ of the two-section T_1 and T_0 delay line.

The autocorrelation function determined in the course of the double spectral processing of the received signal contains an informative peak at a delay time of T_1 = 33.7 ns or T_0 = 18 ns depending on the binary code 1 or 0, respectively (Figs 1c and 1d). A decision concerning the presence of a binary code is taken based on the shift (T_1 or T_0) of the informative peak in the autocorrelation function. In this way, the transmitted information is unambiguously recovered. The spectral compression coefficient $B = \Delta f t_a$ of the received UWB signals is determined by a product of the frequency band Δf and the period of signal averaging, which is equal to the data bit length t_a. For data transmission at a rate of $U = 1/t_a$ = 200 Kb/s based on continuous noise with a bandwidth of Δf = 1000 MHz, the compression coefficient is $B = \Delta f t_a$ = 5000. The data transfer with such a coefficient of coherent compression of the noise signal is characterized by high immunity to arbitrary disturbances [9].

The results of experiments have confirmed the possibility of using UWB continuous noise waveforms for the reliable digital data transmission with high interference immunity. According to the proposed method, the code spectral modulation is realized using interference of the delayed noise signals with a shift according to the sequence of transmitted data bits. The spectral compression of received UWB signals is performed via real-time double spectral processing. The secondary spectrum contains an informative peak in the form of a correlation function of the received UWB signal. The sequence of data bits is unambiguously recovered based on the shift of the informative peak in the secondary spectrum.

Acknowledgments. This study was supported by the Russian Foundation for Basic Research, project nos. 04-02-16536 and 04-07-08013.

REFERENCES

1. C. E. Shannon, Bell Syst. Tech. J. **27**, 379 (1948).
2. V. I. Kalinin, Radiotekh. Élektron. (Moscow) **41**, 488 (1996).
3. *Ultra-Wideband Radar Technology*, Ed. by J. D. Tylor (CRC Press, Boca Raton, 2000).
4. V. I. Kalinin, in *Proceedings of the 6th International Conference and Exhibition on Digital Signal Processing and Applications, Moscow, 2004*, Vol. 1, pp. 225–228.
5. Yu. V. Gulyaev, V. Ya. Kislov, V. I. Kalinin, *et al.*, Radiotekhnika, No. 10, 3 (2002).
6. A. S. Dmitriev and A. I. Panas, *Dynamical Chaos: New Information Media for Communication Systems* (Fizmatlit, Moscow, 2002) [in Russian].
7. A. R. Volkovskiĭ and N. V. Rul'kov, Pis'ma Zh. Tekh. Fiz. **19** (3), 71 (1993) [Tech. Phys. Lett. **19**, 97 (1993)].
8. E. V. Kal'yanov, Pis'ma Zh. Tekh. Fiz. **27** (16), 1 (2001) [Tech. Phys. Lett. **27**, 701 (2001)].
9. N. T. Petrovich and M. K. Razmakhnin, *Communication Systems with Noiselike Signals* (Sov. Radio, Moscow, 1969) [in Russian].
10. J. L. Poirier, Radio Sci. **3**, 881 (1968).
11. V. I. Kalinin, in *Proceedings of the PIERS Workshop on Advances in Radar Methods, Baveno, 1998*, pp. 222–224.

Translated by P. Pozdeev

Technical Physics Letters, Vol. 31, No. 11, 2005, pp. 932–933. Translated from Pis'ma v Zhurnal Tekhnicheskoĭ Fiziki, Vol. 31, No. 21, 2005, pp. 64–67.

Self-Organization in a Layer of Magnetic Fluid in Strong Electric Fields

V. M. Kozhevnikov*, I. Yu. Chuenkova, M. I. Danilov, and S. S. Yastrebov

North-Caucasus State Technical University, Stavropol, Russia

** e-mail: kvm@stv.runnet.ru*

Received April 20, 2005

Abstract—The effect of a polarizing voltage on the electrical properties of a magnetic fluid confined between the plates of a plane capacitor connected to a series resonance circuit has been studied. The magnetic fluid layer features the formation, development, and self-organization of aggregates with dimensions on the order of several millimeters. These processes influence the physical properties of the magnetic fluid layer. *© 2005 Pleiades Publishing, Inc.*

The phenomenon of a change in the physical properties of magnetic fluids as a result of their structuring under the action of external electric fields has been extensively studied in recent years [1–3]. In particular, we have investigated the formation of structures in magnetic fluids exposed to relatively weak electric fields with a strength not exceeding 400 kV/m. It was established that the average size of observed structural elements did not exceed several microns, and their formation was attributed to an increase in the concentration of a disperse phase near electrodes and the subsequent aggregation processes in this phase. As is known, strong external actions on various media may lead to the appearance of substantially new structures as a result of the phenomenon of self-organization.

This Letter presents the results of investigations into the physical properties of a layer of magnetic fluid exposed to strong electric fields.

The experiments were performed using a setup based on a series resonance circuit comprising a standard coil with an induction of $L = 0.22$ H and a plane capacitor. The capacitor represented a cell formed by two plane-parallel glass plates with transparent conducting coatings and a layer of magnetic fluid confined between these plates [3]. The thickness of the magnetic fluid layer was determined by dielectric spacers. The cell allowed a polarizing electric field with a strength of up to $E_p = 5000$ kV/m to be generated between the capacitor plates. The magnetic fluid was based on kerosene and represented a suspension of magnetite particles (with a total solid phase content of about 2%) stabilized by oleic acid.

The series resonance circuit was excited by a sinusoidal signal from a generator with an effective voltage amplitude of $U = 1.5$ V and a variable frequency. The resonance was achieved by finding the signal frequency corresponding to a maximum of the alternating current in the circuit, which was determined by measuring the voltage drop on a shunting resistor $R_s = 100\ \Omega$. The polarizing voltage was applied to the cell from a source of controlled dc voltage and measured by a voltmeter.

Observations in the transmitted light revealed the formation of structures in the magnetic fluid, with the characteristic dimensions of the elements varying from 0.1 to 5 mm. The observed patterns and the size of their elements depended on the polarizing voltage and the duration of its application. When the polarizing field strength was increased, the structural elements increased in size and the pattern changed from a cellular structure to labyrinth and to fractal clusters (Figs. 1a and 1b). Simultaneous observations of interference patterns at the cell surface in reflected light revealed the presence of autowave processes in the magnetic fluid layer.

Figure 2 shows plots of the resonance current versus polarizing voltage for various thicknesses of the magnetic fluid layer. The observed variations are related to changes in the conductivity of the cell, which are caused by the formation of aggregates, their structuring, and self-organization. The smaller the thickness of the magnetic fluid layer, the more pronounced the field-induced changes in the resonance current. The structures formed in 20- to 40-μm-thick layers under the action of a polarizing voltage of 20–30 V have the form of vortices with spiral waves outgoing from the center (Fig. 1c). The appearance of a maximum of resonance current for magnetic fluid layers with thicknesses in the range from 80 to 220 μm at a polarizing voltage of 20–30 V reflects the synchronization of autowave processes. As can be seen from Fig. 2, an increase in the layer thickness from 80- to 220 μm does not change the character of variation of the resonance current as a function of the polarizing voltage. The results were reproduced well and the random errors did not exceed 1.5%.

It was established that the resonance current in the cell circuit (and, hence, the cell conductivity) in the

1063-7850/05/3111-0932$26.00

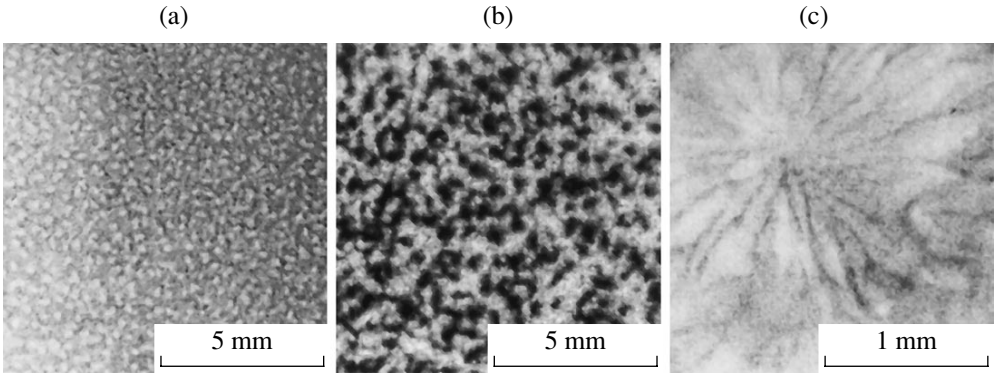

Fig. 1. Dissipative structures observed in the transmitted light in magnetic fluid layers of different thicknesses for various polarizing field strengths E_P = 100 (a), 300 (b) and 1000 kV/m (c).

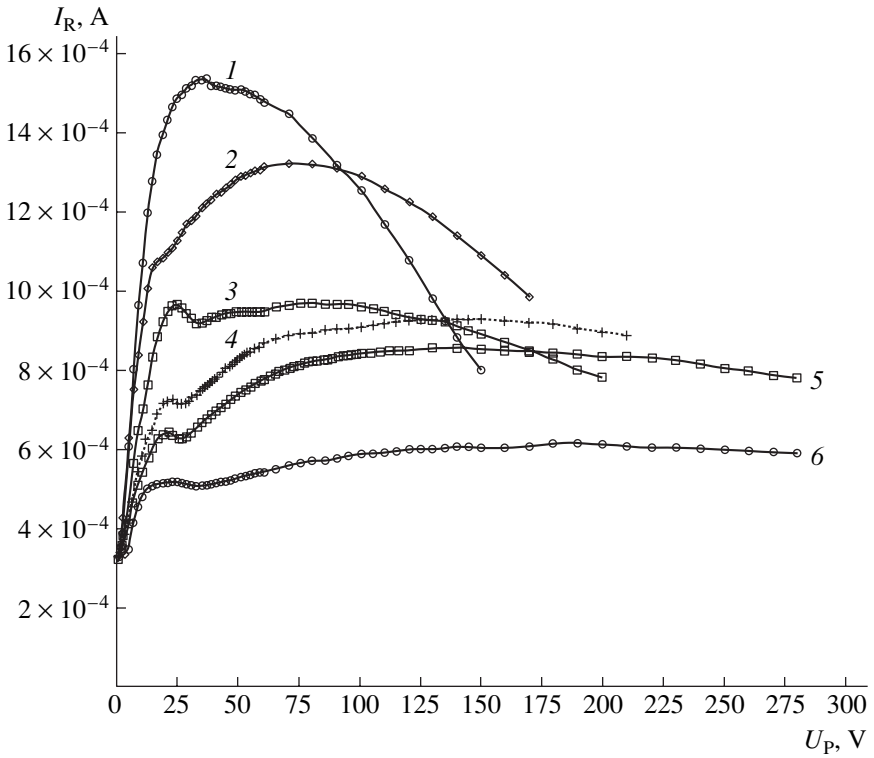

Fig. 2. Experimental plots of the resonance current I_R versus polarizing voltage U_P for magnetic fluid layers with a solid phase (magnetite) content of 2% and various thicknesses (μm): (*1*) 20; (*2*) 40; (*3*) 80; (*4*) 110; (*5*) 150; (*6*) 220.

absence of a polarizing voltage is independent of the magnetic fluid layer thickness. Therefore, the electrical properties of this layer under such conditions are determined by the near-electrode regions, which are characterized by low conductivity. The application of a polarizing voltage to the cell with the magnetic fluid gives rise to correlated motions of the charge carriers, which is manifested by the observed macroscopic structures. The behavior of the resonance current in the circuit as a function of the polarizing voltage changes when the magnetic fluid layer thickness is decreased below a certain level, which is explained by a decrease in the number of magnetite particles in the interelectrode space, which are involved in the formation of dissipative structures.

REFERENCES

1. V. M. Kozhevnikov and T. F. Morozova, Magnetohydrodynamics **37**, 383 (2001).
2. Yu. I. Dikansky and O. A. Nechaeva, Magnetohydrodynamics **38**, 287 (2002).
3. V. M. Kozhevnikov, J. A. Larionov, I. J. Chuenkova, *et al.*, Magnetohydrodynamics **40**, 269 (2004).

Translated by P. Pozdeev

Technical Physics Letters, Vol. 31, No. 11, 2005, pp. 934–935. Translated from Pis'ma v Zhurnal Tekhnicheskoĭ Fiziki, Vol. 31, No. 21, 2005, pp. 68–72.

The Limiting Charge of a Subnanosecond Electron Beam Generated in a Dense Gas

A. N. Tkachev and S. I. Yakovlenko*

Institute of General Physics, Russian Academy of Sciences, Moscow, Russia

** e-mail: syakov@kapella.gpi.ru*

Received June 15, 2005

Abstract—The charge of a subnanosecond beam of runaway electrons generated in a dense gas is principally limited by decreasing strength of the applied electric field. The field decreases because a positive charge appears in the plasma, which compensates for the charge of runaway electrons. The dependence of the limiting beam charge on the voltage applied to the electrodes is determined using the calculated electron runaway curves. The potential of increasing the electron beam intensity is demonstrated. © *2005 Pleiades Publishing, Inc.*

Recently, we reported on the generation of high-current (hundreds of amperes) subnanosecond pulsed beams of runaway electrons in diodes filled with gases at atmospheric pressures [1, 2]. The most important aspects in the mechanism of formation of such beams are as follows. The electron beam is generated when a nonlocal criterion of electron runaway [2–4] is satisfied, since plasma formed at the cathode approaches the anode to a distance comparable with the inverse Townsend ionization coefficient. Thus, plasma effectively decreases the interelectrode gap, which ensures validity of the electron runaway criterion. The plasma propagates due to the multiplication of background electrons, rather than due to the electron transport [5, 6]. The background ionization is provided by high-energy electrons emitted from inhomogeneities on the cathode surface. For effective electron beam generation at atmospheric pressure, it is necessary to use voltage generators with a nanosecond pulse front width and to match the arrival of the electron multiplication wave at the anode to the moment the maximum voltage is reached.

It is obvious that physical limitations of the maximum current transferred by such electron beans must exist, similar to the limitations imposed by the well-known "3/2" law on the dc current value (see, e.g., [7–9]). This Letter is devoted to an analysis of such limitations.

Electron runway curve. Let us assume that the electron multiplication wave [5] approaching the anode has a sufficiently steep front. At a given voltage U between the electrodes, the electron beam generation takes place when this wave front occurs at a certain distance from the anode. This distance d can be determined from the aforementioned nonlocal criterion of electron runaway [2–4],

$$pd\xi(U/pd) = 1, \qquad (1)$$

where p is the gas pressure and $\xi(E/p)$ is a certain function of the reduced field strength E/p characteristic of a given working gas. The latter function determines the Townsend ionization coefficient for the given gas: $\alpha_i(E, p) = p\xi(E/p)$.

The function $U(pd)$, which is determined by Eq. (1), is called the electron loss curve [2, 4]. This is a two-valued function, which separates the region of parameters corresponding to the intense electron multiplication in the volume of discharge and the region of parameters for which electrons leave the discharge without significant multiplication. The existence of two branches in the electron loss curve $U(pd)$ is related to the presence of a maximum in the $\xi(E/p)$ function. The electron loss curves for some gases are presented in recent reviews [2, 4]. The lower branch of the runaway curve, separating the regions of multiplication and the electron loss via drift, is called the electron drift curve. The upper branch, which separates the region of multiplication and the region corresponding to the formation of a bean of runaway electrons, is called the electron runaway curve. The consideration below is devoted to the latter curve.

Limiting electron beam charge. The phenomenon of limitation of the charge carried by the electron beam is related to the appearance of an excess positive charge at the electron multiplication wave front approaching the anode, which compensates for the charge of runaway electrons. This positive charge effectively decreases the field pulling out the electrons, which leads to the violation of criterion (1). This situation is analogous to the stationary case, whereby the space charge of particles pulled by the field accounts for a limitation imposed by the well-known "3/2" law [7–9].

In the space between the multiplication wave front and the anode, the electric field strength is $E = U/d$. Accordingly, the charge density compensating this field is $q = E/2\pi = U/2\pi d$. Expressing d from Eq. (1), we determine the dependence of the limiting charge density q of runaway electrons on the applied voltage U (Fig. 1c).

1063-7850/05/3111-0934$26.00 © 2005 Pleiades Publishing, Inc.

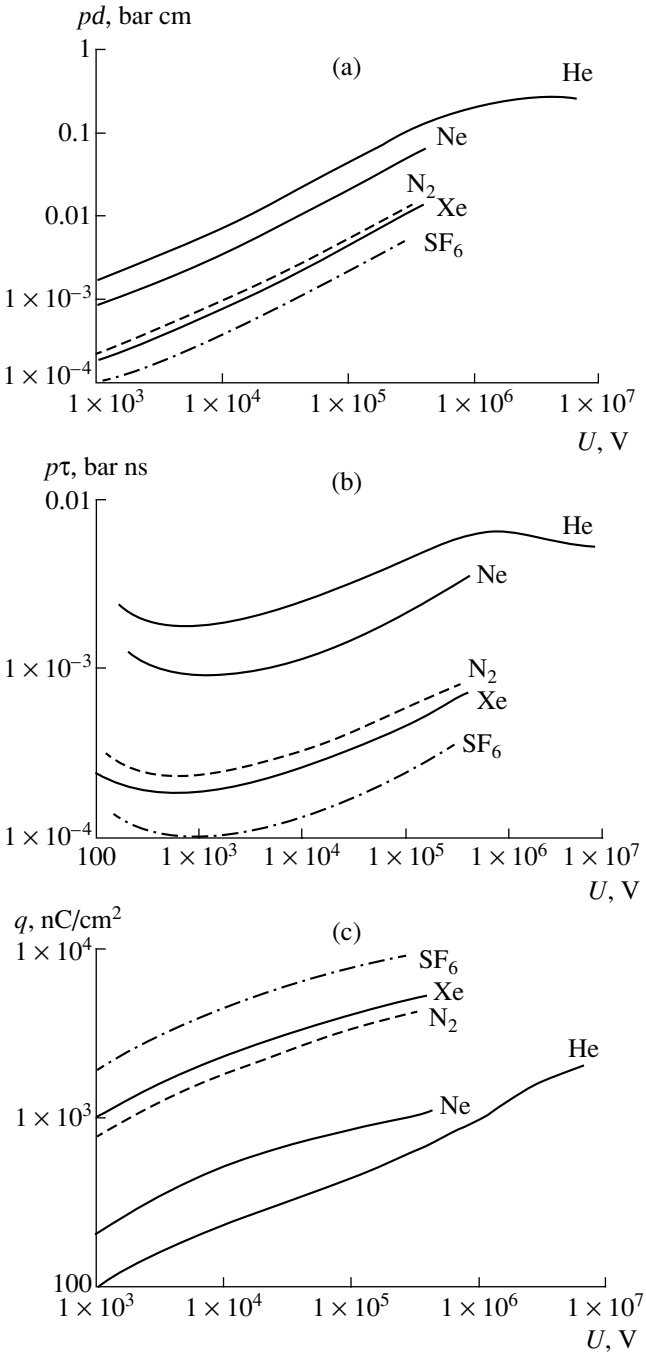

Fig. 1. Plots of the quantities characterizing limitations imposed on the runaway electron beam intensity versus interelectrode voltage U for high-pressure discharges in helium, neon, nitrogen, xenon, and sulfur hexafluoride: (a) the product of gas pressure p and the distance d from the multiplication wave front to anode; (b) the product of gas pressure p and the time of charged layer formation $\tau = d(2m_e/eU)^{1/2}$; (c) the limiting charge density q carried by the beam of runaway electrons.

The time of formation of the aforementioned charged layer can be evaluated as $\tau = d(2m_e/eU)^{1/2}$ (Fig. 1b).

Discussion. The limiting charge density q depicted in Fig. 1c is never reached in experiment. For example, a beam with a current of 200 A and a duration of 0.3 ns obtained in helium at a peak voltage of 200 kV for an electrode area of about 1 cm^2 corresponds to a charge density of 60 nC/cm^2, whereas the limiting charge density for a beam in helium at this voltage is q = 550 nC/cm^2 (Fig. 1c). For the other gases, the limiting beam charge density exceeds the experimental values to an even greater extent.

The reason for this difference is probably related to the fact that the multiplication wave front is usually smeared as compared to the extremely small d value determined from Eq. (1). An increase in the distance at which the runaway electrons are generated is accompanied by a decrease in the field strength and, hence, in the limiting charge density. It should also be noted that, in order to suppress the beam generation, it is sufficient to somewhat reduce the field strength rather than to fully compensate the charge of runaway electrons.

Refinement of the limiting beam charge current values and determination of the time variation of the beam current are very difficult problems, which require solving the kinetic equations (e.g., the Vlasov equation) jointly with the Poisson equation.

Conclusion. The above considerations show that the intensity of subnanosecond electron beams generated in dense gases can be, in principle, increased. Since a further decrease in the multiplication wave front duration encounters extremely complicated technical problems, it would be expedient to optimize the conditions of electron beam generation with respect to the gas pressure.

REFERENCES

1. V. F. Tarasenko, S. I. Yakovlenko, V. M. Orlovskiĭ, *et al.*, Pis'ma Zh. Éksp. Teor. Fiz. **77**, 737 (2003) [JETP Lett. **77**, 611 (2003)].
2. V. F. Tarasenko and S. I. Yakovlenko, Usp. Fiz. Nauk **174**, 953 (2004) [Phys. Usp. **47**, 887 (2004)].
3. A. N. Tkachev and S. I. Yakovlenko, Pis'ma Zh. Éksp. Teor. Fiz. **77**, 264 (2003) [JETP Lett. **77**, 221 (2003)].
4. A. N. Tkachev and S. I. Yakovlenko, Cent. Eur. J. Phys. **2**, 579 (2004); www.cesj.comp/physics.htm.
5. S. I. Yakovlenko, Zh. Tekh. Fiz. **74** (9), 47 (2004) [Tech. Phys. **49**, 1150 (2004)].
6. I. D. Kostyrya, V. M. Orlovskiĭ, V. F. Tarasenko, *et al.*, Zh. Tekh. Fiz. **74** (9), 47 (2004) [Tech. Phys. **49**, 457 (2004)].
7. P. A. Kaptsov, *Electronics* (Gostekhizdat, Moscow, 1954) [in Russian].
8. V. L. Granovskiĭ, *Electric Current in a Gas* (Nauka, Moscow, 1971) [in Russian].
9. A. T. Forrester, *Large Ion Beams: Fundamentals of Generation and Propagation* (Wiley, New York, 1988).

Translated by P. Pozdeev

Technical Physics Letters, Vol. 31, No. 11, 2005, pp. 936–938. Translated from Pis'ma v Zhurnal Tekhnicheskoĭ Fiziki, Vol. 31, No. 21, 2005, pp. 73–78.

Screening of the Disclination Elastic Field by a System of Dislocations

G. F. Sarafanov* and V. N. Perevezentsev**

Blagonravov Mechanical Engineering Research Institute (Nizhni Novgorod Branch), Russian Academy of Sciences, Nizhni Novgorod, Russia

*e-mail: *sarafanov@sinn.ru; **pevn@uic.nnov.ru*

Received June 20, 2005

Abstract—An effective Airy stress function of a disclination is constructed with allowance for the screening effect of a system of distributed dislocation charges. The spatial distributions of the stress tensor of a screened disclination and the dislocation charge density are determined. The elastic energy of a screened disclination is calculated. © *2005 Pleiades Publishing, Inc.*

In the stage of developed plastic deformation, the collective modes of the motion of dislocations lead to the appearance of a large-scale order in the distribution of dislocations in the applied stress field. Such ordered dislocation structures are called mesodefects [1–3]. The characteristic mesodefects formed in the stage of developed plastic deformation have been established and classified, the most typical of them representing broken dislocation boundaries [4]. From the theoretical standpoint, it is interesting to understand why the formation of such boundaries in the bulk of grains is energetically favorable. This problem is especially important, since the existence of broken dislocation boundaries is prohibited by the classical theory of crystal lattice defects [5, 6].

According to [7, 8], broken subboundaries can be interpreted in many cases as partial disclinations. As is known, the elastic fields of disclinations grow with distance. In the existing models [8, 9], the screening of the elastic fields of disclinations is provided by allowance for the existence of disclinations of the opposite sign. Therefore, it is assumed that the disclination systems of real crystals always comprise dipoles, quadrupoles, and other compensated configurations. It should be noted, however, that (i) experiments show evidence for the existence of uncompensated broken dislocation boundaries (branching small-angle boundaries, subboundaries terminating with a "torch" of lattice dislocations of a deformed grain, etc.) [2] and (ii) it is evident that both nucleation and propagation of broken subboundaries (partial disclinations) in the bulk of grains proceeds as a result of the collective motion of dislocations.

In view of the above considerations, it is expedient to evaluate the elastic fields of disclination configurations taking into account the contribution due to surrounding dislocations, since their redistribution in the elastic field of disclinations can reduce the total elastic energy of the system. This Letter presents the results of the development of this approach.

Let us consider a wedge disclination (situated at the origin of a coordinate system) surrounded by an ensemble of edge dislocations, which realize plastic deformation in an external stress field σ_e. The dislocations are characterized by the density $\rho_a(\mathbf{r}, t)$ and the Burgers vector b_a (oriented in the dislocation slip direction $(0_x(\mathbf{b}_a \parallel \mathbf{e}_x)$). The dislocation ensemble has a zero total Burgers vector $\sum_a b_a\rho_{a0} = 0$, where $\rho_{a0} = \rho_0/2$ is the density of a homogeneous distribution of dislocations in the given stress field σ_e and $a = \pm$. The total elastic field due to the disclination and the ensemble of dislocations is determined by the effective Airy stress function

$$\begin{aligned}\psi^{\Sigma}(\mathbf{r}) &= \psi(\mathbf{r}) + \sum_a \int \rho_a(\mathbf{r}')\psi_a^e(|\mathbf{r}-\mathbf{r}'|)d\mathbf{r}' \\ &= \psi(\mathbf{r}) + Db\int I(\mathbf{r}')(y-y')\ln\frac{r_0}{|\mathbf{r}-\mathbf{r}'|}dr',\end{aligned} \quad (1)$$

where $\psi(\mathbf{r}) = D\omega/2(r^2\ln(r/R) - r^2/2)$ is the Airy stress function for the wedge disclination [8], R is the radius of truncation of the elastic field (e.g., the characteristic crystal size), ω is the disclination power, $\psi_a^e(\mathbf{r}) = -b_aDy\ln(r/r_0)$ is the Airy stress function for the edge dislocation [5], $I(\mathbf{r}) = \rho_+(\mathbf{r}) - \rho_-(\mathbf{r})$ is the excess dislocation density (dislocation charge), $D = G/2\pi(1 - \nu)$, G is the shear modulus, and ν is the Poisson ratio.

A consistent analysis of the problem related to the determination of the effective Airy stress function $\psi^{\Sigma}(\mathbf{r})$ can be performed within the framework of a self-consistent field approximation which has been developed in plasma physics and is known as the Debye approxi-

mation [10]. A characteristic feature of this approximation is that, in the state of thermodynamic equilibrium, both electrons (e) and ions (i) in a self-consistent field ($U_{\text{eff}} = e\varphi_{\text{eff}}$) are distributed according to the Boltzmann law. Under the condition of electroneutrality ($n_{0e} = n_{0i} = n_0/2$), the charged particles obey the relation $(n_i - n_e)/n_0 = \sinh(-e\varphi_{\text{eff}}/kT) \simeq -U_{\text{eff}}/kT$ characteristic of the given approximation [10].

In a Coulomb plasma, the equilibrium distribution of charged particles is established as a result of their thermal motion (and, accordingly, temperature plays the role of an external parameter determining the process of relaxation toward the equilibrium state). In the problem under consideration, a stationary state of the dislocation system under the conditions of plastic deformation is attained as a result of the generation and annihilation of dislocations. Here, an analog of the temperature is offered by the work of plastic deformation $T_{\text{ext}} \simeq b\sigma_e \bar{L}$, which corresponds to the propagation of a dislocation over a mean free path length $\bar{L}$.

Thus, applying the logic of the self-consistent field approximation to the problem under consideration, we may suggest that

$$I(\mathbf{r}) = -\rho_0 \frac{U_{\text{eff}}(\mathbf{r})}{T_{\text{ext}}} = -\frac{\rho_0 b}{T_{\text{ext}}} \frac{\partial \psi^{\Sigma}(\mathbf{r})}{\partial y}, \qquad (2)$$

where $U^a_{\text{eff}}(\mathbf{r}) = b_a \partial \psi^{\Sigma}(\mathbf{r})/\partial y$ is the energy of interaction of a separate dislocation with the self-consistent elastic field. Passing to the Fourier components in Eqs. (1) and (2), we obtain

$$\psi^{\Sigma}(\mathbf{k}) = \frac{4\pi D\omega}{|\mathbf{k}|^4 + 4k_y^2 r_d^{-2}}, \quad I(\mathbf{k}) = \frac{ik_y 4\omega b^{-1} r_d^{-2}}{|\mathbf{k}|^4 + 4k_y^2 r_d^{-2}}, \quad (3)$$

where $r_d^{-2} = \pi\rho_0 b^2 D/T_{\text{ext}}$. Using relations (3), we can determine the stationary spatial distribution of the dislocation charge (see figure) in the elastic field of a disclination:

$$I(\mathbf{r}) = \frac{1}{(2\pi)^2} \int \frac{ik_y 4\omega b^{-1} r_d^{-2}}{|\mathbf{k}|^4 + 4k_y^2 r_d^{-2}} e^{-i\mathbf{kr}} d\mathbf{k} = I_e \sinh(y/r_d) K_0(r/r_d), \qquad (4)$$

where $I_c = \omega/\pi b r_d$ and $K_0(r/r_d)$ is the zero-order Macdonald function [11]. Finally, applying the inverse Fourier transformation and taking into account the unknown function $\psi^{\Sigma}(\mathbf{k})$, we obtain expressions for the stress tensor of the defect system under consideration:

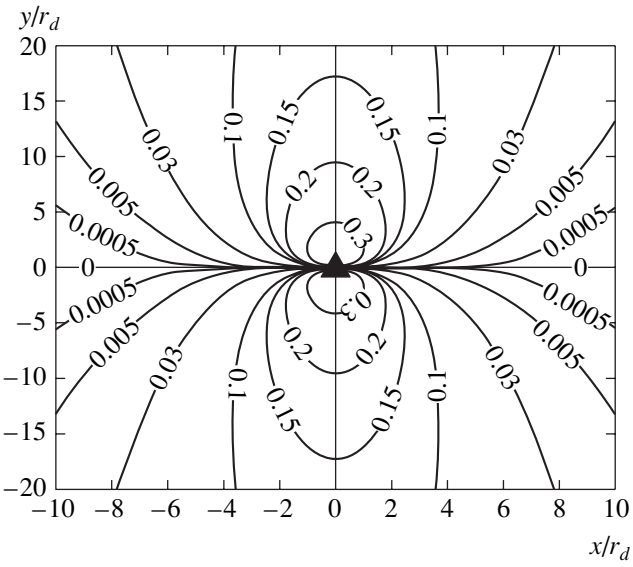

Stationary spatial distribution of the normalized excess dislocation density $I(x, y)/I_c$ in the field of a disclination situated at the origin of coordinates. The maximum dislocation charge $I = \pm 0.5 I_c$ is observed at the points with $x = 0$, $y = \pm 0.8 r_d$.

$$\sigma^{\Sigma}_{yy}(\mathbf{r}) = \frac{\partial^2 \psi^{\Sigma}(\mathbf{r})}{\partial x^2} = -D\omega\left[\cosh(y/r_d) K_0(r/r_d) + \sinh(y/r_d)\frac{y}{r} K_1(r/r_d)\right], \qquad (5)$$

$$\sigma^{\Sigma}_{xx}(\mathbf{r}) = \frac{\partial^2 \psi^{\Sigma}(\mathbf{r})}{\partial y^2} = -D\omega\left[\cosh(y/r_d) K_0(r/r_d) - \sinh(y/r_d)\frac{y}{r} K_1(r/r_d)\right], \qquad (6)$$

$$\sigma^{\Sigma}_{xy}(\mathbf{r}) = -\frac{\partial^2 \psi^{\Sigma}(\mathbf{r})}{\partial x \partial y} = -D\omega \sinh(y/r_d)\frac{x}{r} K_1(r/r_d), \qquad (7)$$

where $K_1(z) = -K_0'(z)$ is the first-order Macdonald function.

Equations (5)–(7) show that the elastic fields σ^{Σ}_{ij} decay with distance and become very small at $r \gg r_d$ ($K_0(r/r_d) \sim \sqrt{\pi r_d/2r}\, e^{-r/r_d}$ [11]). For this reason, the parameter r_d can be considered as the radius of screening of the elastic field of a disclination in the dislocation slip direction $0x$ (in the $0y$ direction, the elastic field

decays according to a hyperbolic law). It should also be noted that the spatial scale r_d coincides with the screening radius introduced in [12].

Using expressions (5)–(7), we can readily determine the energy W^Σ of the elastic field of the disclination–surrounding dislocations system:

$$W^\Sigma = \frac{D^2\omega^2}{2G}\int_0^R r dr \int_0^{2\pi} [\sinh^2(y/r_d)K_1^2(r/r_d) + (1-2\nu)\cosh^2(y/r_d)K_0^2(r/r_d)]d\varphi \simeq \frac{\sqrt{\pi}}{4}D\omega^2 r_d^2\sqrt{\frac{R}{r_d}}. \quad (8)$$

Comparing this formula to the energy $W = D\omega R^2/8$ of an unscreened disclination [8], we obtain

$$W^\Sigma/W = 2\sqrt{\pi}(r_d/R)^{3/2}. \quad (9)$$

Let us obtain some estimates. The screening radius according to [12] is on the order of an average distance between dislocations. In the stage of developed plastic deformation, the density of dislocations is $\rho \sim 10^{10}$ cm^{-2} [1], so that $r_d \sim \rho^{-1/2} \simeq 10^{-5}$ cm. Taking the characteristic scale R equal to the grain size $D = 2$ μm, we obtain $W^\Sigma/W = 3 \times 10^{-2}$, whereas for $D = 10$ μm the screening effect is $W^\Sigma/W \sim 3 \times 10^{-3}$. Thus, a system of excess dislocations distributed according to the law (4) established for mesodefects produces effective screening of a disclination and significantly decreases the elastic energy of the disclination.

In the initial formulation, the problem was considered in infinite space. However, taking into account that the characteristic scale r_d of decay of the elastic field is rather small (except for the direction perpendicular to the slip system), we may suggest that the obtained results can be generalized to the case of grains with dimensions $d \gg r_d$.

REFERENCES

1. V. V. Rybin, *Large Plastic Deformations and Failure of Metals* (Metallurgiya, Moscow, 1986) [in Russian].
2. V. V. Rybin, Vopr. Materialoved., No. 4 (32), 11 (2002).
3. V. N. Perevezentsev and V. V. Rybin, Vopr. Materialoved., No. 4 (32), 113 (2002).
4. A. N. Vergazov, V. A. Likhachev, and V. V. Rybin, Fiz. Met. Metalloved. **42**, 146 (1976).
5. J. P. Hirth and J. Lothe, *Theory of Dislocations* (McGraw-Hill, New York, 1967; Atomizdat, Moscow, 1972).
6. A. M. Kosevich, *Physical Mechanics of Real Crystals* (Naukova Dumka, Kiev, 1981) [in Russian].
7. R. De Wit, J. Res. Natl. Bur. Stand., Sect. A **77**, 49, 359, 607 (1973).
8. V. I. Vladimirov and A. E. Romanov, *Disclinations in Crystals* (Nauka, Leningrad, 1986) [in Russian].
9. A. E. Pomanov, in *Proceedings of the International Conference "Nanomaterials under Severe Plastic Deformation (NANOSPD2)," Vienna, 2002* (Wiley–VCH, Weinheim, 2004), pp. 215–225.
10. L. D. Landau and E. M. Lifshitz, *Course of Theoretical Physics*, Vol. 5: *Statistical Physics* (Nauka, Moscow, 1976; Pergamon, Oxford, 1980).
11. V. S. Vladimirov, *Equations of Mathematical Physics* (Nauka, Moscow, 1981; Dekker, New York, 1971).
12. G. F. Sarafanov, Fiz. Tverd. Tela (St. Petersburg) **39**, 1575 (1997) [Phys. Solid State **39**, 1403 (1997)].

Translated by P. Pozdeev

Technical Physics Letters, Vol. 31, No. 11, 2005, pp. 939–942. Translated from Pis'ma v Zhurnal Tekhnicheskoĭ Fiziki, Vol. 31, No. 21, 2005, pp. 79–86.

Estimating the Parameters of Semiconductor Optical-Feedback Lasers from Time Series

V. I. Ponomarenko[a,*], M. D. Prokhorov[a], and I. V. Koryukin[b]

[a] *Institute of Radio Engineering and Electronics (Saratov Branch), Russian Academy of Sciences, Saratov, Russia*
[b] *Institute of Applied Physics, Russian Academy of Sciences, Nizhni Novgorod, Russia*
* *e-mail: sbire@sgu.ru*

Received May 27, 2005

Abstract—A new method is proposed for estimating the control parameters of single-mode semiconductor optical-feedback lasers from experimentally measured time series of the laser intensity. The procedure is based on a statistical analysis of specially selected points of the time series and on the phenomenon of chaotic synchronization of unidirectionally coupled lasers with coinciding parameters. © *2005 Pleiades Publishing, Inc.*

In recent years, much attention has been devoted to the use of semiconductor optical-feedback lasers for secure data transmission [1–3]. The interest in these lasers as potential sources for data transmission systems with a high degree of information security is related to the fact that the laser intensity exhibits wideband chaotic oscillations of very high dimension. The extraction of transmitted data in communication systems employing chaotic signals is possible due to the phenomenon of synchronization of coupled chaotic dynamical systems [4–6]. Such a synchronization of the interacting chaotic systems is manifested for certain types of coupling between them and can be used to estimate the control parameters of the coupled systems [7–12]. Previously, several methods were proposed for the estimation of parameters of coupled dynamical systems, which were based on autosynchronization [7], adaptive control [8, 12], random optimization [9], error minimization [10], and iterative adaptation of parameters [11].

This Letter describes a new method for sequential refinement of the control parameters of semiconductor optical-feedback lasers, which is based on the phenomenon of chaotic synchronization.

Let us consider a single-mode semiconductor optical-feedback laser whose operation is described by the Lang–Kobayashi equations [13]. After appropriate normalization, these equations can be written in the following form [14]:

$$\begin{aligned} \dot{E}(t) &= (1 + i\alpha)F(t)E(t) \\ &+ \eta E(t - \tau_0)\exp(-i\Omega\tau_0), \\ T\dot{F}(t) &= P - F(t) - (1 + 2F(t))|E(t)|^2, \end{aligned} \tag{1}$$

where $E(t)$ is the complex amplitude of the electric field, which exhibits slow variation (on the time scale of optical oscillations); F is the density of nonequilibrium charge carriers; $T = \tau_s/\tau_p$ is the ratio of the carrier lifetime τ_s to the photon lifetime τ_p in the laser cavity; P is the pumping parameter (in excess of the generation threshold); τ_0 is the delay time in the optical feedback chain; η is the feedback gain; α is the factor of nonisochronicity; Ω is the laser frequency in the absence of the feedback; and the upper dot denotes differentiation with respect to dimensionless time t (expressed in units of the photon lifetime τ_p).

Writing the complex field amplitude as $E(t) = \rho(t)\exp(i\phi(t))$ [where $\rho(t)$ and $\phi(t)$ are the modulus and phase of $E(t)$], denoting $\rho = \rho(t)$, $\rho_\tau = \rho(t - \tau_0)$, $\phi = \phi(t)$, $\phi_\tau = \phi(t - \tau_0)$, and $F = F(t)$, and taking into account that the complex constant $\exp(-i\Omega\tau_0)$ determining the phase shift in the feedback chain does not qualitatively influence the procedure proposed below for evaluation of the delay time (and, hence, can be omitted), we can rewrite system of equations (1) as follows:

$$\begin{aligned} \dot{\rho} &= F\rho + \eta\rho_\tau\cos(\phi - \phi_\tau), \\ \rho\dot{\phi} &= F\alpha\rho - \eta\rho_\tau\sin(\phi - \phi_\tau), \\ T\dot{F} &= P - F - (1 + 2F)\rho^2. \end{aligned} \tag{2}$$

Previously, we demonstrated that the time series of delay systems of the type $\dot{x}(t) = F(x(t), x(t - \tau))$ possess virtually no extrema separated from each other by τ [15] and developed a method employing this circumstance for determining τ. Now we will show that this method, after appropriate modification, can also be applied to a time-delay system of the type described by Eqs. (2). Differentiating the first equation in system (2) with respect to time t, we obtain

$$\begin{aligned} \ddot{\rho} &= \dot{F}\rho + F\dot{\rho} + \eta\dot{\rho}_\tau\cos(\phi - \phi_\tau) \\ &- \eta\rho_\tau\sin(\phi - \phi_\tau)(\dot{\phi} - \dot{\phi}_\tau). \end{aligned} \tag{3}$$

1063-7850/05/3111-0939$26.00 © 2005 Pleiades Publishing, Inc.

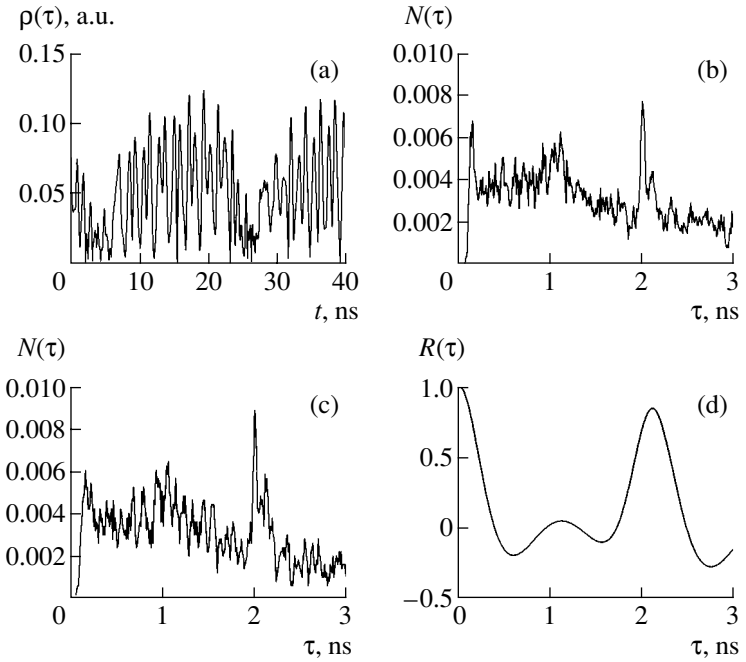

Fig. 1. Estimation of the parameters of a Lang–Kobayashi system (2): (a) typical experimental time series for the system with parameters $P = 1.1 \times 10^{-3}$, $\tau_0 = 2$ ns, $\eta = 5 \times 10^{-3}$, $T = 10^3$, and $\alpha = 5$; (b, c) plots of $N(\tau)$ for the time series of variables ρ and I normalized to the total number of points simultaneously obeying conditions (4) and (6); (d) autocorrelation function $R(\tau)$ for the laser intensity oscillations.

The typical time series of oscillations of the variable $\rho = |E|$ for a single-mode semiconductor optical-feedback laser described by Eqs. (2) with a small value of parameter P exhibits a large number of extrema in which ρ is close to zero (Fig. 1a). Such points are characterized by simultaneously obeying two conditions:

$$\dot{\rho} = 0, \quad \rho < \varepsilon, \tag{4}$$

where ε is a certain small quantity. According to Eq. (3), these points also obey the relation

$$\frac{\dot{\rho}_\tau}{\rho_\tau} \approx \frac{\ddot{\rho} + \eta\rho_\tau \sin(\phi - \phi_\tau)(\dot{\phi} - \dot{\phi}_\tau)}{\eta\rho_\tau \cos(\phi - \phi_\tau)}. \tag{5}$$

In the typical case of quadratic extrema, we have $\dot{\rho} = 0$ and $\ddot{\rho} \neq 0$. From this we infer that, for small ρ_τ, the ratio $\dot{\rho}_\tau/\rho_\tau$ must be quite large. Taking this fact into account, we can use the following method of processing of the time series of ρ to determine the delay time τ_0 in a system described by equations (2). First, we consider the points satisfying conditions (4) and select those also meeting the conditions

$$\rho_\tau < \varepsilon, \quad \dot{\rho}_\tau/\rho_\tau > \Theta, \tag{6}$$

for sufficiently large Θ. Since τ_0 is unknown, we try various τ and count the number N of the pairs of points simultaneously satisfying conditions (4) and (6). Then, the function $N(\tau)$ represents the number of the pairs of points for which conditions (4) are satisfied at the time t and conditions (6) at $t - \tau$. For τ equal to the true delay time τ_0, the number of points $N(\tau_0)$ must be greater than that for arbitrary τ, where the conditions (6) may not be satisfied. Therefore, the position of the maximum in the $N(\tau)$ curve gives us an estimate for the delay time τ_0. The same considerations are applicable to the experimental time series of oscillations of the laser intensity $I = |E|^2$.

Figure 1b shows the $N(\tau)$ curve constructed as described above for a time series of the variable ρ in Eqs. (2) with $\tau_0 = 2$ ns, $P = 1.1 \times 10^{-3}$, $\eta = 5 \times 10^{-3}$, $T = 10^3$, $\alpha = 5$, $\varepsilon = \sigma_1/k_1$, and $\Theta = \sigma_2 k_2$, where σ_1 is the rms deviation of ρ, σ_2 is the rms deviation of $\dot{\rho}_\tau/\rho_\tau$, $k_1 = 1$, and $k_2 = 7$. This plot was constructed using a series of 400000 points, which contained about 4000 points satisfying conditions (4). As the values of k_1 and k_2 are increased, the number of points used for the construction of the $N(\tau)$ curve decreases. When τ was varied at a step of 0.01 ns, the absolute maximum of $N(\tau)$ is observed at $\tau = 2.00$ ns, which is precisely the actual delay time. Figure 1c presents a plot of $N(\tau)$ constructed using time series of the intensity I for system (2) with the same control parameters as in Fig. 1b, but with $k_1 = k_2 = 4$. In this case, the procedure of delay time estimation based on the search for a maximum of the autocorrelation function yields $\tau_0 = 2.10$ ns (Fig. 1d).

For estimating the other parameters of the system under consideration, we suggest the phenomenon of chaotic synchronization observed for two semiconductor lasers with unidirectional coupling be used. Such unidirectionally coupled systems (1) are described by the following equations [16]:

$$\dot{E}^{\mathrm{T,R}} = (1 + i\alpha^{\mathrm{T,R}})F^{\mathrm{T,R}}E^{\mathrm{T,R}} + \eta^{\mathrm{T,R}}E^{\mathrm{T,T}}(t-\tau^{\mathrm{T,R}})\exp(-i\Omega^{\mathrm{T,R}}\tau^{\mathrm{T,R}}),$$
$$T^{\mathrm{T,R}}\dot{F}^{\mathrm{T,R}} = P^{\mathrm{T,R}} - F^{\mathrm{T,R}} - (1 + 2F^{\mathrm{T,R}})\left|E^{\mathrm{T,R}}\right|^2, \quad (7)$$

where the variables and parameters of the drive system (transmitter) are indicated by superscript "T" and those of the response system (receiver) are indicated by superscript "R." When the parameters of two coupled systems are sufficiently close, these systems exhibit synchronization [16].

Since the α and T values in real lasers of the same type are fixed and close, we assume these parameters for the transmitter and receiver to be same: $\alpha^{\mathrm{T}} = \alpha^{\mathrm{R}}$ and $T^{\mathrm{T}} = T^{\mathrm{R}}$. The other parameters of the transmitter (P^{T}, η^{T}, and τ^{T}) will be estimated by providing its synchronization with the receiver, whose parameters (P^{R}, η^{R}, and τ^{R}) can be tuned. A convenient quantitative measure of synchronization is provided by the correlation function

$$C(\tau) = \frac{\langle I^{\mathrm{T}}(t)I^{\mathrm{R}}(t+\tau)\rangle}{\sqrt{\langle I^{\mathrm{T}}(t)^2\rangle\langle I^{\mathrm{R}}(t)^2\rangle}}, \quad (8)$$

where $I^{\mathrm{T,R}} = |E^{\mathrm{T,R}}|^2$ and the angle brackets indicate averaging with respect to time. In the case of compete synchronization, this function has a maximum value at the origin, and this maximum reaches unity when all parameters of the transmitter and receiver are identical. If the analogous parameters of the transmitter and receiver are slightly different, the maximum value of $C(\tau)$ differs from unity, while its shift from the origin gives an estimate of the difference of delay times in the transmitter and receiver.

Let us set the same transmitter parameters as those used above for a single system and select the initial approximation as $\tau^{\mathrm{R}} = 2.00$ ns (which corresponds to the absolute maximum of $N(\tau)$) and $\eta^{\mathrm{R}} = 1 \times 10^{-3}$. The third parameter ($P^{\mathrm{R}}$) will be estimated by plotting the maximum value ($C_{\max}$) of the correlation function (8) versus the parameter P^{R} (Fig. 2a). As can be seen, $C_{\max}$ reaches the absolute maximum at $P^{\mathrm{R}} = 1.8 \times 10^{-3}$. Then, we plot $C_{\max}$ as a function of η^{R} for $P^{\mathrm{R}} = 1.8 \times 10^{-3}$ (Fig. 2b). This curve has the absolute maximum at $\eta^{\mathrm{R}} = 5.2 \times 10^{-3}$. In the next step, we again plot $C_{\max}$ versus P^{R}, but with the just refined value of η^{R} (Fig. 2c), and so on. The next step (Fig. 2d) already gives the true value of the feedback gain, $\eta^{\mathrm{R}} = \eta^{\mathrm{T}} = 5.0 \times 10^{-3}$, for which the P^{R} value no longer varies in subsequent iteration steps. The correlation function exhibits maximum at the origin and this maximum is $C_{\max} = 1$. This result confirms that the plot of $N(\tau)$ constructed as described above provides exact estimation of the delay time, since $\tau^{\mathrm{R}} = \tau^{\mathrm{T}} = 2$ ns.

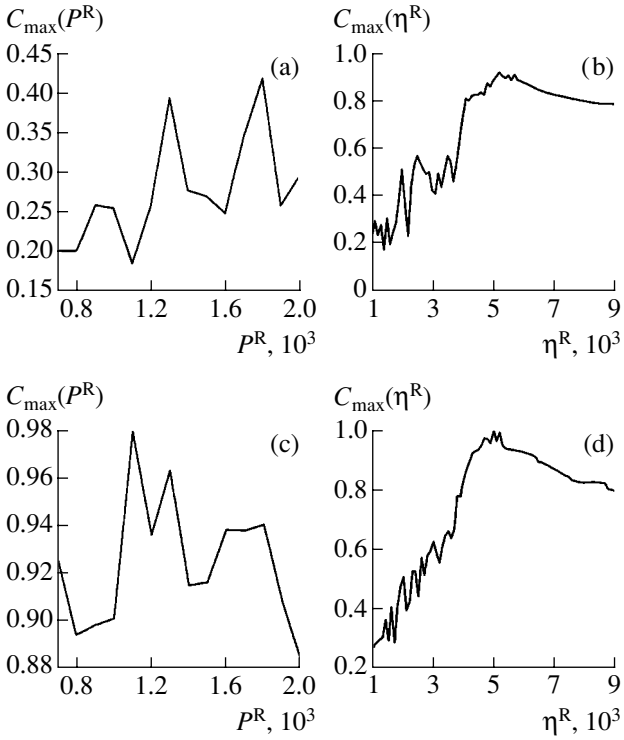

Fig. 2. Sequential refinement of the transmitter parameters based on the chaotic synchronization of unidirectionally coupled lasers as illustrated by plots of the maximum ($C_{\max}$) of the correlation function (8) versus the receiver parameters P^{R} and η^{R}: (a) $\eta^{\mathrm{R}} = 1 \times 10^{-3}$, $C_{\max}(P^{\mathrm{R}})$ is maximum at $P^{\mathrm{R}} = 1.8 \times 10^{-3}$; (b) $P^{\mathrm{R}} = 1.8 \times 10^{-3}$, $C_{\max}(\eta^{\mathrm{R}})$ is maximum at $\eta^{\mathrm{R}} = 5.2 \times 10^{-3}$; (c) $\eta^{\mathrm{R}} = 5.2 \times 10^{-3}$, $C_{\max}(P^{\mathrm{R}})$ is maximum at $P^{\mathrm{R}} = 1.1 \times 10^{-3}$; (d) $P^{\mathrm{R}} = 1.1 \times 10^{-3}$, $C_{\max}(\eta^{\mathrm{R}})$ is maximum at $\eta^{\mathrm{R}} = 5.0 \times 10^{-3}$.

Applying the proposed method for the numerical investigation of system (7), it is also possible to estimate the other parameters of the transmitter, for example, α^{T} and T^{T}, under the conditions $\eta^{\mathrm{R}} = \eta^{\mathrm{T}}$ and $P^{\mathrm{R}} = P^{\mathrm{T}}$. If all parameters of the transmitter in the numerical experiment are unknown, the procedure converges to the true values only provided that the initial values are selected close to the corresponding true parameters.

We have also evaluated the robustness of the above procedure of sequential refinement of the control parameters by introducing an additive noise into the communication channel between the transmitter and receiver. It was established that the proposed method provides correct estimation of the parameters P^{T} and η^{T} even in the presence of significant noise on a level of 10%.

Conclusion. We have developed a new method for the sequential refinement of parameters of single-mode semiconductor optical-feedback lasers described by the Lang–Kobayashi equations. The proposed procedure employs the phenomenon of chaotic synchronization of unidirectionally coupled lasers. We also described a procedure for the initial estimation of the delay time in the feedback chain, which is based on the statistical analysis of specially selected points of a measured time series of the laser intensity. The efficiency of the proposed method is confirmed by the results obtained for unidirectionally coupled Lang–Kobayashi systems.

The possibility of estimating the parameters of semiconductor optical-feedback lasers provides a means of useful signal extraction in communication systems employing chaotic signals for masking the transmitted data. Therefore, the level of security provided by such communication systems based on single-mode semiconductor lasers can be insufficient, despite the very high dimension and the large number of positive Lyapunov exponents for chaotic attractors in these dynamical systems.

Acknowledgments. This study was supported by the Russian Foundation for Basic Research (project nos. 03-02-17593 and 03-02-17243), the U.S. Civilian Research and Development Foundation for the Independent States of the Former Soviet Union (CRDF Award no. REC-006), and by the INTAS Foundation (grant no. 03-55-920).

REFERENCES

1. V. Ahlers, U. Parlitz, and W. Lauterborn, Phys. Rev. E **58**, 7208 (1998).
2. S. Sivaprakasam and K. A. Shore, Opt. Lett. **24**, 466 (1999).
3. I. Fisher, Y. Liu, and P. Davis, Phys. Rev. A **62**, 011801 (2000).
4. L. M. Pecora and T. L. Carroll, Phys. Rev. Lett. **64**, 21 (1990).
5. L. Kocarev, K. S. Halle, K. Eckert, *et al.*, Int. J. Bifurcation Chaos Appl. Sci. Eng. **2**, 709 (1992).
6. L. M. Pecora, T. L. Carroll, G. A. Johnson, *et al.*, Chaos **7**, 520 (1997).
7. U. Parlitz, Phys. Rev. Lett. **76**, 1232 (1996).
8. A. Maybhate and R. E. Amritkar, Phys. Rev. E **59**, 284 (1999).
9. H. Sakaguchi, Phys. Rev. E **65**, 027201 (2002).
10. R. Konnur, Phys. Rev. E **67**, 027204 (2003).
11. C. Tao, Y. Zhang, G. Du, and J. J. Jiang, Phys. Rev. E **69**, 036204 (2004).
12. D. Huang, Phys. Rev. E **69**, 067201 (2004).
13. R. Lang and K. Kobayashi, IEEE J. Quantum Electron **16**, 347 (1980).
14. P. M. Alsing, V. Kovanis, A. Gavrielides, and T. Erneux, Phys. Rev. A **53**, 4429 (1996).
15. B. P. Bezruchko, A. S. Karavaev, V. I. Ponomarenko, and M. D. Prokhorov, Phys. Rev. E **64**, 056216 (2001).
16. I. V. Koryukin and P. Mandel, Phys. Rev. E **65**, 026201 (2002).

Translated by P. Pozdeev

Technical Physics Letters, Vol. 31, No. 11, 2005, pp. 943–946. Translated from Pis'ma v Zhurnal Tekhnicheskoĭ Fiziki, Vol. 31, No. 21, 2005, pp. 87–94.

Effect of the Ratio of Differently Charged Ions on the Integral Parameters of Stationary Plasma Thrusters of the ATON Type

A. I. Bugrova[a,*], A. S. Lipatov[a], A. I. Morozov[a], and S. V. Baranov[b]

[a] *Moscow Institute of Radio Engineering, Electronics, and Automatics (Technical University), Moscow, Russia*

[b] *"Kurchatov Institute" Russian Research Center, Moscow, Russia*

** e-mail: bgrova@mirea.ru*

Received June 9, 2005

Abstract—The main integral parameters of stationary plasma thrusters (SPTs) of the ATON type with the outer channel diameters 60 mm (model A-3) and 100 mm (model A-5) are presented. The SPT characteristics have been studied for the propellant (Xe) consumption rates $\dot{m}$ = 2 and 1 mg/s for A-3 and $\dot{m}$ = 4 and 1.5 mg/s for A-5. Special attention has been devoted to the operation of SPT models at high voltages and low propellant consumption rates. An increase in the voltage has to be accompanied by a corresponding change in the magnetic field topograph and by an increase in the magnetic field intensity at the channel edge, which leads to a decrease in the discharge current and its oscillations. Model A-3 operating at $\dot{m}$ = 1 mg/s and a voltage somewhat below 1000 V exhibited a specific momentum of ~3400 s. The integral characteristics of SPTs depend on the ratio of differently charged ions in the plasma. The most efficient operation of the plasma source is observed in the case of equal concentrations of singly and doubly charged xenon ions. A new method is proposed for evaluation of the limiting SPT efficiency using only the current–voltage and propulsion characteristics of discharge. © *2005 Pleiades Publishing, Inc.*

The physical processes in stationary plasma accelerators with closed electron drift, also called stationary plasma thrusters (SPTs), have been described in considerable detail [1–3]. Since monitoring of the degree of ionization of the propellant (xenon) at the SPT output encounters certain technical difficulties, the development of methods for the rapid and reliable evaluation of the charged state of plasma is among currently important tasks. Previously, we proposed a method [1, 2] for determining the charged state of plasma using the results of measurements of several integral characteristics, including the propellant consumption rate ($\dot{m}$), discharge current (J_d), and propulsion (F).

A series of SPT models of the second generation (ATON type) operating on xenon have been developed at the Moscow Institute of Radio Engineering, Electronics, and Automatics (MIREA). These models have various dimensions of discharge chambers and operate in different ranges of propellant consumption. As is known [3–5], SPTs with different geometries working on the same propellant are characterized by a certain range of the main parameters (propellant consumption rate, $\dot{m}$; discharge voltage, U_d) in which the accelerators operate in a similar manner from the standpoint of physical processes. In this regime, the minimum consumption of the working gas is determined by the similarity criterion $\alpha = (\dot{m}/S)b \approx 2 \times 10^{-2}$ mg/(s mm), where b and S are the channel width and the output cross section area, respectively.

This paper presents the results of investigation into the working characteristics of two SPT models with the outer channel diameters 60 mm (model A-3) and 100 mm (model A-5). Special attention has been devoted to the operation of SPT models at high voltages. The current–voltage (J_d–U_d) characteristics were measured in the range of discharge voltages from 200 up to about 1000 V. At each point, the model operation was optimized with respect to the magnetic field. The results of these experiments showed that an increase in the voltage has to be accompanied by a change in the magnetic field topograph in the channel, so as to increase the magnetic field intensity at the channel edge. This leads to a decrease in the discharge current and its oscillations. The J_d–U_d curves and propulsion characteristics were measured in a broad range of working gas consumption rates (below, the data are presented for two values of $\dot{m}$ characteristic of each SPT model).

Figures 1 and 2 show the integral characteristics of SPT models A-3 and A-5 as functions of the discharge voltage for two propellant consumption rates. As can be seen from Fig. 1a, the J_d–U_d curves are practically hor-

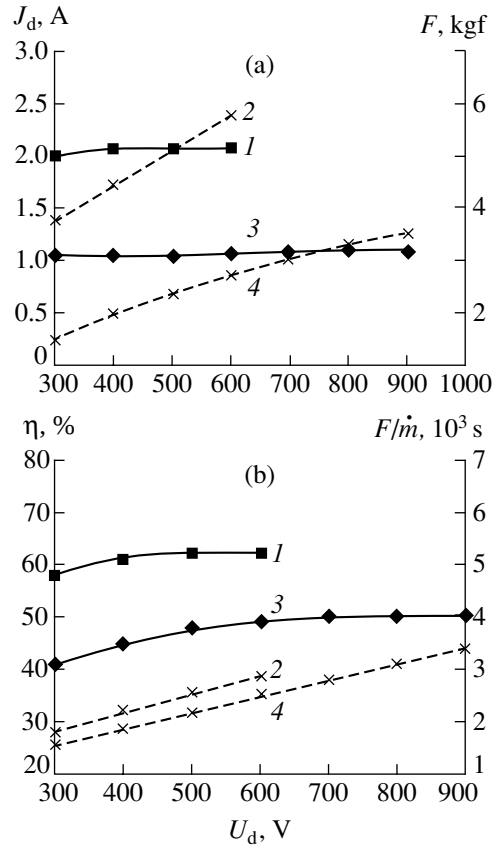

Fig. 1. The experimentally measured integral parameters of SPT model A-3 operating at a propellant consumption rate of $\dot{m}$ = 2 mg/s (*1*, *2*) and 1 m/s (*3*, *4*): (a) current voltage characteristics (*1*, *3*) and propulsion F (*2*, *4*); (b) efficiency η (*1*, *3*) and specific momentum (*2*, *4*).

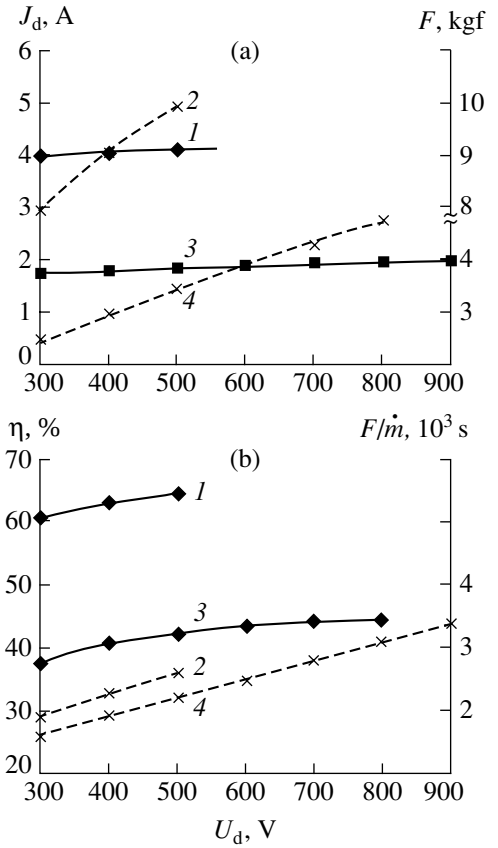

Fig. 2. The experimentally measured integral parameters of SPT model A-5 operating at a propellant consumption rate of $\dot{m}$ = 4 mg/s (*1*, *2*) and 1.5 mg/s (*3*, *4*): (a) current voltage characteristics (*1*, *3*) and propulsion F (*2*, *4*); (b) efficiency η (*1*, *3*) and specific momentum (*2*, *4*).

izontal in the entire discharge voltage range studied, while the propulsion F grows with the voltage and the rate of this growth increases with the rate of working gas consumption. For $\dot{m}$ = 1 mg/s, the efficiency of A-3 attains a plateau at U_d ~ 700–900 V and the specific momentum reaches a level of ~3400 s. The main parameters of A-5 generally exhibit the same behavior as functions of the discharge voltage. However, the efficiency of this SPT at $\dot{m}$ = 1.5 mg/s is somewhat lower than that of A-3, because this consumption rate is too low for a wide-channel thruster.

According to the notions formulated in [1], the SPT output plasma jet is considered as a completely ionized medium consisting of three fractions, which represent the singly and doubly charged ions and the particles not subjected to acceleration (nonionized, lost on the walls, converted into neutrals, etc.). We have studied the influence of the ratio of these fractions of particles on the efficiency of SPT operation in a broad range of parameters.

Let us assume that the first and second ionization events take place in the same region of the system. In this case, we have $\varepsilon_2 \geq 2\varepsilon_1$, where $\varepsilon_{1,2}$ are the corresponding ion rates. The flows of ions of the three types obey the following system of equations:

$$\begin{aligned} \dot{m} &= \dot{m}_1 + \dot{m}_2 + \dot{m}_*, \\ F &= \sqrt{\frac{2e}{M}(U_d - \Delta U)}(\dot{m}_1 + \sqrt{2}\dot{m}_2), \\ J_d &= \frac{e}{M}(1+k)(\dot{m}_1 + 2\dot{m}_2 + \varepsilon\dot{m}_*), \end{aligned} \qquad (1)$$

where $\dot{m}$ is the total gas flow rate; $\dot{m}_1$, $\dot{m}_2$, and $\dot{m}_*$ are the consumption rates of the singly and doubly charged ions and the lost particles, respectively; e/M is the ratio of the electron charge to the xenon atom mass; ΔU is the potential with allowance for losses; k is the coefficient determining the contribution of the "through" current to the discharge current ($k \approx 0.1$); and $\varepsilon \approx 1$ is the number of ionization events. As can be seen from Eqs. (1), only the ions (both singly and doubly charged) contribute to the propulsion, whereas the discharge current depends on the flow rates of all particles.

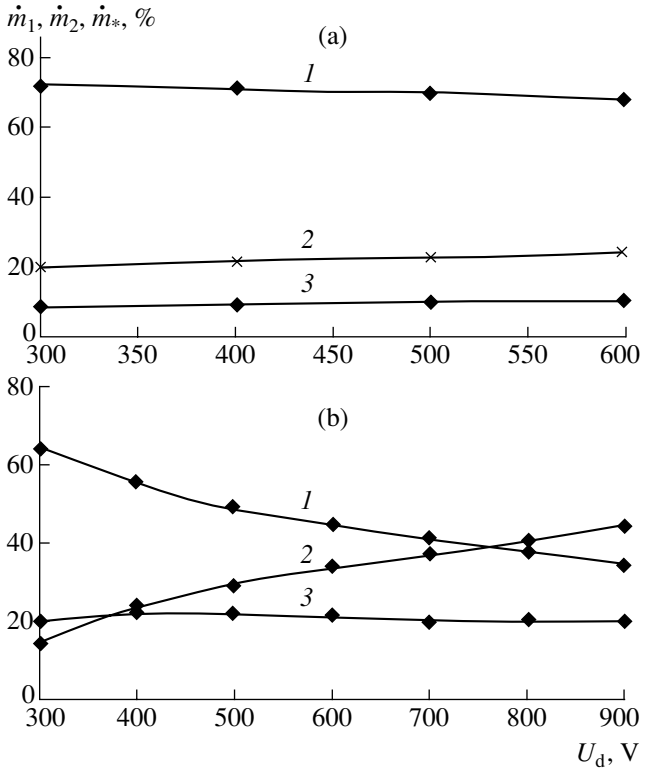

Fig. 3. The plots of (*1*) $\dot{m}_1$, (*2*) $\dot{m}_2$, and (*3*) $\dot{m}_*$ versus U_d for SPT model A-3 operating at a propellant consumption rate of (a) 2 and (b) 1 mg/s.

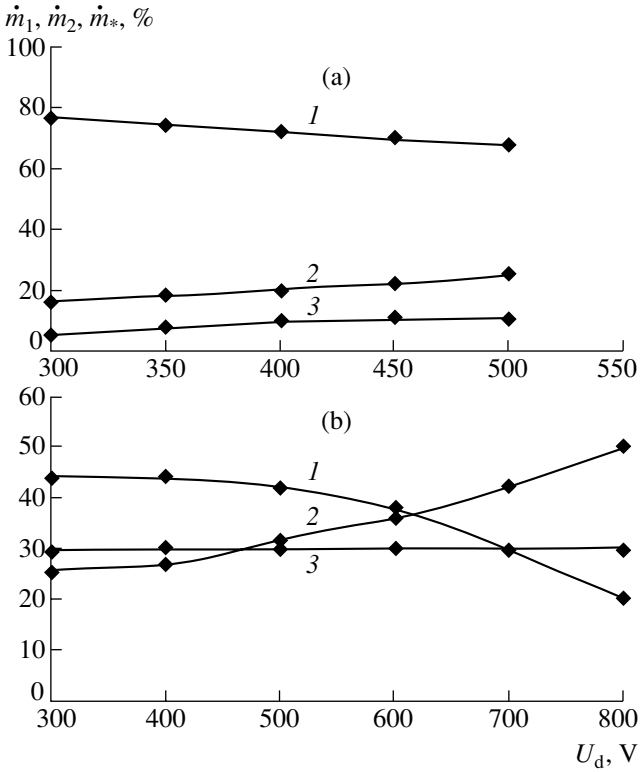

Fig. 4. The plots of (*1*) $\dot{m}_1$, (*2*) $\dot{m}_2$, and (*3*) $\dot{m}_*$ versus U_d for SPT model A-5 operating at a propellant consumption rate of (a) 4 and (b) 1.5 mg/s.

Equations (1) yield the following expressions for the flow components:

$$\dot{m}_1 = \frac{-\sqrt{2}A + (2-\varepsilon)B + \sqrt{2}\varepsilon C}{(\sqrt{2}-1)(\sqrt{2}+\varepsilon)},$$
$$\dot{m}_2 = \frac{A + (\varepsilon-1)B - \varepsilon C}{(\sqrt{2}-1)(\sqrt{2}+\varepsilon)}, \quad (2)$$
$$\dot{m}_* = \frac{(\sqrt{2}-1)A - B + (2-\sqrt{2})C}{(\sqrt{2}-1)(\sqrt{2}+\varepsilon)},$$

where

$$A = \frac{J}{e/M(1+k)}, \quad B = \frac{F}{\sqrt{2e\dot{M}(U-\Delta U)}}, \quad C = \dot{m}.$$

J_d is the discharge current, F is the propulsion, and $U_d - \Delta U$ is the effective accelerating voltage.

Figures 3 and 4 show the values of $\dot{m}_1$, $\dot{m}_2$, and $\dot{m}_*$ calculated using formulas (2) with the values of integral parameters determined for the SPT regimes studied. As can be seen from these data, the growth of the discharge voltage leads to a decrease in the fraction of singly charged ions and to an increase in the fraction of doubly charged ions. For small propellant consumptions ($\dot{m}$ = 1 mg/s for A-3 and 1.5 mg/s for A-5) these fractions become equal at U_d ~ 600–700 V. In the operation regimes with higher propellant consumptions, the flow rates of singly and doubly charged ions become equal at a much higher discharge voltage (see Figs. 3a and 4a).

A comparison of the dynamics of variation of the fractions of singly and doubly charged ions (Figs. 3 and 4) to the dynamics of the SPT efficiency η (Figs. 1 and 2) shows that η reaches maximum when the fractions of singly and doubly charged ions become equal (i.e., at a discharge voltage of ~600–700 V). This result implies that the SPT efficiency in the optimum operation regime can be determined without conducting detailed investigations of the plasma source. Indeed, using the experimentally measured J_d–U_d curves and propulsion characteristics, we can determine the discharge voltage U_d^* at which $\dot{m}_1(U_d^*) = \dot{m}_2(U_d^*)$ from the following relation:

$$F(U_d^*)/\sqrt{\frac{2e}{M}(U_d^* - \Delta U)}$$
$$= (1+\sqrt{2})\left(J(U_d^*)/\frac{e}{M}(1+k) - \dot{m}\right). \quad (3)$$

Then the maximum efficiency can be evaluated as

$$\eta_{max} = \eta(U_{d0}) + \left[\frac{\partial \eta_d(\dot{m}, U_d)}{\partial U_d}\right]_{U_d = U_{d0}} (U_d^* - U_{d0}), \quad (4)$$

where $\eta(U_{d0})$ is the efficiency at $U_{d0} < U_d^* \approx 600$ V.

Conclusions. The obtained experimental results lead to the following conclusions:

(i) Within the framework of the three-component model, the maximum efficiency of operation of a plasma source of the SPT type is achieved in the regimes corresponding to equal fractions of singly and double charged ions in the plasma.

(ii) The limiting efficiency of a classical SPT of the ATON type operating at a relatively low level of power supplied to the discharge can be evaluated using formula (4) and the results of measurements of only the current–voltage and propulsion characteristics.

Acknowledgments. This study was supported by the INTAS Foundation, grant no. 0353-3358.

REFERENCES

1. A. I. Morozov, A. I. Bugrova, A. V. Desyatskov, *et al.*, Fiz. Plazmy **23**, 635 (1997) [Plasma Phys. Rep. **23**, 587 (1997)].
2. A. I. Bugrova, A. S. Lipatov, A. I. Morozov, and L. V. Solomatina, Fiz. Plazmy **28**, 118 (2002) [Plasma Phys. Rep. **28**, 1032 (2002)].
3. A. I. Bugrova, A. S. Lipatov, A. I. Morozov, and D. V. Churbanov, Pis'ma Zh. Tekh. Fiz. **28** (19), 73 (2002) [Tech. Phys. Lett. **28**, 821 (2002)].
4. A. I. Bugrova, N. A. Maslennikov, and A. I. Morozov, Zh. Tekh. Fiz. **61** (6), 45 (1991) [Sov. Phys. Tech. Phys. **36**, 612 (1991)].
5. I. V. Melikov, Zh. Tekh. Fiz. **44**, 549 (1974) [Sov. Phys. Tech. Phys. **19**, 343 (1974)].

Translated by P. Pozdeev

Technical Physics Letters, Vol. 31, No. 11, 2005, pp. 947–950. Translated from Pis'ma v Zhurnal Tekhnicheskoĭ Fiziki, Vol. 31, No. 22, 2005, pp. 1–8.

Structural and Magnetic Characteristics of Fe/Si Bilayer and Multilayer Films Obtained by Thermal Deposition in Ultrahigh Vacuum

S. N. Varnakov[a], A. S. Parshin[b], S. G. Ovchinnikov[a], D. Rafaja[c], L. Kalvoda[d], A. D. Balaev[a], and S. V. Komogortsev[a]

[a] *Kirensky Institute of Physics, Siberian Division, Russian Academy of Sciences, Krasnoyarsk, 660036 Russia*

[b] *Siberian State Aerospace University, Krasnoyarsk, 660041 Russia*

[c] *Institute of Physical Metallurgy, TU Bergakademie Freiberg, D-09599 Freiberg, Germany*

[d] *Czech Technical University, 16636 Prague 6, Czech Republic*

Received June 17, 2005

Abstract—The structural and magnetic characteristics of Fe/Si bilayer and multilayer films with nanometer-thick layers obtained by thermal deposition in ultrahigh vacuum have been studied by methods of small-angle X-ray scattering, electron spectroscopy, and magnetometry. It is established that the mechanisms involved in the formation of Fe/Si and Si/Fe interfaces are different. © *2005 Pleiades Publishing, Inc.*

In recent years, increasing attention has been devoted to multilayer magnetic structures in view of their unique physical properties and good prospects for practical applications [1, 2]. In particular, the phenomenon of colossal magnetoresistance, which had originally been discovered in metal superlattices, was later also observed in multilayer structures composed of alternating metal and semiconductor layers [3]. Investigations into the properties of multilayer structures with semiconductor interlayers (spacers) open the way to the creation of novel materials possessing unique properties for micro- and nanoelectronics [4]. In the technology of multilayer structures consisting of ultrathin layers, there are special requirements related to precise control over the composition of each layer, which implies that the deposition of layers has to be performed under ultrahigh vacuum (UHV) conditions.

This Letter presents the results of investigation of the structural and magnetic characteristics of Fe/Si bilayer and multilayer films with nanometer-thick layers obtained by thermal deposition in UHV on silicon substrates.

We have studied multilayer structures comprising iron layers with silicon spacers obtained by thermal evaporation in vacuum with deposition on single crystal Si(100) and Si(111) substrates at room temperature. The samples were prepared on a modified molecular beam epitaxy setup of the Angara type with a residual vacuum in the UHV technological chamber 10^{-7} Pa. The component materials were evaporated from refractory (boron nitride) crucibles. The evaporation rate could be controlled by varying the crucible temperature, so that the deposition rates were equal to 0.16 nm/min for iron and 0.9 nm/min for silicon. The control over the temperatures of Fe and Si evaporators and their shutters used for the formation of multilayer structures was provided by an automated programmed complex [5].

The compositions of deposited layers were studied by Auger electron spectroscopy (AES) and electron energy loss spectroscopy (EELS). These measurements

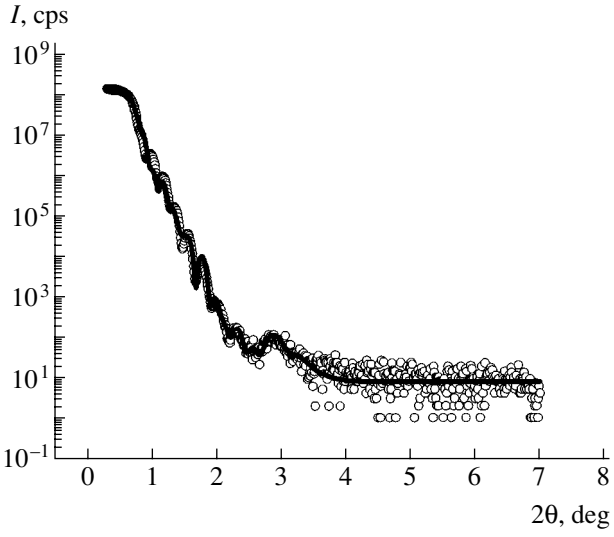

Fig. 1. The typical experimental SAXS data (open symbols) and the results of model calculations (solid curves) for a 20-layer [Fe(2 nm)/Si(2 nm)] × 9/Fe(10 nm)/Si(10 nm) structure.

1063-7850/05/3111-0947$26.00 © 2005 Pleiades Publishing, Inc.

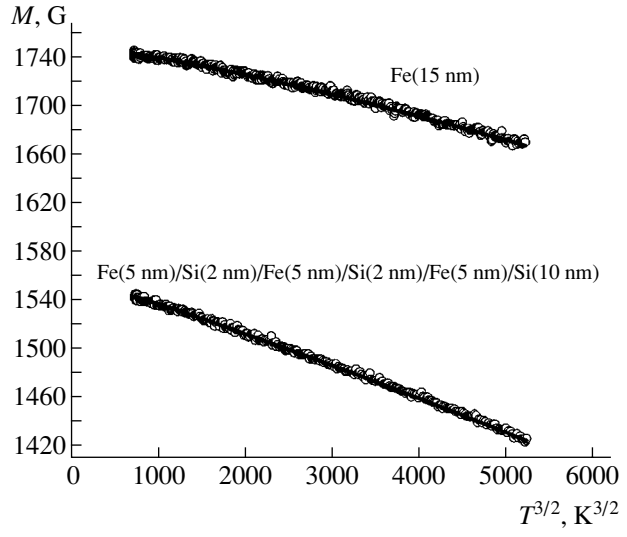

Fig. 2. The typical curves of the magnetization M versus temperature T (on the $T^{3/2}$ scale) for a [Fe(5 nm)/Si(2 nm)] × 2/Fe(5 nm)/Si(10 nm) superlattice measured in an external magnetic field of H = 1 kOe in the temperature range from 4.2 to 250 K: open circles present the experimental data and solid curves show the results of their approximation using expression (1).

were performed *in situ* in the UHV technological system. The structural characteristics (layer thickness, interface roughness) of [Fe(2 nm)/Si(2 nm)] × 9/Fe(10 nm)/Si(10 nm) superlattices were determined from the results of small-angle X-ray scattering (SAXS) measurements [6]. Figure 1 presents the typical experimental SAXS data (open symbols) and the results of model calculations (solid curves) for this structure. Table 1 gives the characteristics of Fe and Si layers obtained from the model calculations, which provided for the best fit to the experimental SAXS data for a 20-layer [Fe(2 nm)/Si(2 nm)] × 9/Fe(10 nm)/Si(10 nm) structure, in comparison to the values determined using technological parameters. The values of the surface roughness determined by fitting the model SAXS intensity profiles to the measured data were comparable with the thicknesses of the component layers. The absolute values of roughness were independent of the thicknesses of adjacent Fe and Si layers and of the order (Fe/Si or Si/Fe) of their deposition. These data characterize the inhomogeneity of multilayer structures with respect to the thicknesses of Fe and Si layers.

Table 1. Data on the layer thickness determined from the deposition time ($d_{technol}$) and the thickness (d_{calcd}) and roughness (h_{calcd}) calculated from the SAXS data for a 20-layer [Fe(2 nm)/Si(2 nm)] × 9/Fe(10 nm)/Si(10 nm) structure

Layer	$d_{technol}$, nm	d_{calcd}, nm	h_{calcd}, nm
Si	10	9.87	2.16
Fe	10	13.71	1.94
Si	2	1.46* ± 0.27	1.34* ± 0.16
Fe	2	1.51* ± 0.27	1.46* ± 0.21
Si	Substrate	–	1.62

* Average for 9 bilayers.

The magnetic properties of Fe/Si multilayers were studied on an automated vibrating-sample magnetometer with a superconducting coil [7]. Figure 2 shows the typical curve of the magnetization M versus temperature T (on the $T_3/2$ scale) for a [Fe(5 nm)/Si(2 nm)] × 2/Fe(5 nm)/Si(10 nm) superlattice measured in an external magnetic field of H = 1 kOe in the temperature range from 4.2 to 250 K. The general character of this $M(T)$ curve is indicative of the absence of paramagnetic and superparamagnetic responses. As can be seen from Fig. 2, the experimental data are well described in terms of a theoretical relation known as the Bloch law (depicted by solid lines) [8]:

$$M(T) = M_0(1 - BT^{3/2} - CT^{5/2}), \quad (1)$$

where M_0 is the zero-temperature magnetization and B and C are temperature-independent coefficients. A relation of the B value to the main magnetic characteristics of the material is described by the empirical formula

$$A = \frac{k}{8\pi}\left(\frac{M_0}{g\mu_B}\right)^{1/3}\left(\frac{2.612}{B}\right)^{2/3}, \quad (2)$$

where A is the exchange coupling constant and μ_B is the Bohr magneton.

Table 2 presents the A, B, and C constants for the multilayer Fe/Si structures under consideration in comparison to the data for body-centered cubic (bcc) α-Fe crystals and a single iron film on silicon. The coincidence of the values of magnetization for a single Fe layer and a bulk bcc α-Fe crystal shows that this Fe layer was also composed of pure bcc iron. A decrease in the effective exchange constant A for this single-layer iron film (with a thickness of d = 15 nm) as determined from the Bloch $T^{3/2}$ law in comparison to the value for bcc α-Fe is consistent with the well-known effect of decreasing effective exchange predicted for thin films within the framework of the spin wave theory [9].

The decrease in M_0 and A values observed for a [Fe(5 nm)/Si(2 nm)] × 2/Fe(5 nm)/Si(10 nm) multilayer film is related to the mutual penetration of Fe and Si atoms into the neighboring layers of this structure [10]. This interdiffusion results in the formation of an interfacial region composed of a Fe–Si solid solution or iron silicides. The observed increase in B (or a decrease in A) and a decrease in M_0 for iron layers of smaller thickness can be readily explained. These changes are related to the formation of a magnetic het-

erophase system and, hence, correspond to an increase in the volume fraction of the interfacial region with lower values of the exchange constant and magnetization. The magnetization of the iron layer with such an interfacial region can be described as

$$M_0 = M_b n_b + M_a n_a = M_b - (M_b - M_a)\frac{2\Delta}{d_{\mathrm{Fe}}}, \quad (3)$$

where n_a and n_b are the fractions of Fe atoms in the interfacial regions and iron layers, respectively, and M_a and M_b and the corresponding magnetizations; Δ is the thickness of the interfacial region; and d_{Fe} is the iron layer thickness. Relation (3) corresponds to a simplified model, whereby a concentration profile characteristic of the real Fe–Si interface is replaced by a stepwise profile [11] including a transition layer with a constant composition and the thickness Δ. In terms of such a model Fe–Si interface with a constant composition and the effective magnetic parameters M_a and A_a, it is convenient to evaluate Δ characterizing the thickness or volume fraction of the interfacial region.

An analysis of the phase diagram of the Fe–Si system [12, 13] showed that the interfacial regions of a multilayer Fe/Si structure can feature the formation of a ferromagnetic solid solution or Fe_3Si and FeSi compounds. For obtaining estimates, we suggested that $M_a = M(Fe_3Si = 1270$ G [12] (nonmagnetic silicide was rejected, since its presence could not account for the observed decrease in the exchange coupling constant A). Within the framework of this model, we have evaluated the thickness of weakly-magnetic interfacial regions formed in a six-layer [Fe(5 nm)/Si(2 nm)] × 2/Fe(5 nm)/Si(10 nm) structure. The total thickness of interfaces in this structure was estimated at 6Δ = 5.4 nm.

Assuming that the thicknesses of transition layers at the Fe/Si and Si/Fe interfaces are the same, the thickness of each interfacial region in the six-layer [Fe(5 nm)/Si(2 nm)] × 2/Fe(5 nm)/Si(10 nm) structure under consideration is Δ = 0.9 nm. In this case, a single Si/Fe interface for the aforementioned 15-nm-thick Fe film on a silicon substrate must, according to formula (3), decrease the magnetization by 30 G. However, the data in Table 2 show that no such decrease takes place for a real iron film on silicon substrate. This discrepancy can be related to a difference in the parameters of Fe/Si and Si/Fe junctions, which, in turn, is caused by the different mechanisms of formation of such interfaces in the course of sample preparation by means of thermal deposition.

In order to elucidate the mechanism of the Fe–Si interface formation, we have studied by EELS the bilayer structures of two types, Fe(10 nm)/Si(1.5 nm) and Si(10 nm)/Fe(1.5 nm), which were specially prepared for this purpose. It was found that the electron energy loss spectrum of a Si(10 nm)/Fe(1.5 nm) sample with the upper layer of iron is virtually the same as that of a single 10-nm-thick iron film on a silicon substrate. In contrast, the spectrum of a sample with the upper layer of silicon exhibited peaks with energy positions (21.9 eV for the first bulk plasmon) corresponding to those reported for iron Fe_3Si silicide [14]. Our results also agree with the conclusions made by Klasges *et al.* [15] upon a comparison of the electronic structures of iron silicides formed in a Fe film on Si substrate and a Si film on Fe substrate. According to the data of spin-resolved photoemission spectroscopy, it was concluded that the mechanisms of formation of Si/Fe and Fe/Si interfaces are different [15]: in one case, a metal-like interface with a thickness of ~2 nm and a composition close to Fe_3Si was formed, whereas the photoemission spectrum in the other case corresponded to an amorphous layer of bulk silicon or a Fe_xSi_{1-x} so lid solution with small x.

Table 2. The main magnetic characteristics of multilayer Fe/Si structures

Material	M_0, G	B, 10^{-5} K$^{-3/2}$	C, 10^{-8} K$^{-5/2}$	A, 10^{-6} erg/cm
α-Fe (fcc)	1740	0.34	0.1	2.1
Single Fe layer	1750	0.49	0.1	1.7
Multilayer Fe/Si structure	1560	1.38	1.0	0.9

In conclusion, the results of our complex study of the structural and magnetic characteristics of Fe/Si multilayer films obtained by thermal deposition in UHV on single crystal silicon substrates show evidence for a significant influence of the transition region with a modified chemical composition formed at the Fe–Si interface on the magnetic properties of the system. The possible difference in the mechanisms of formation of the Fe/Si and Si/Fe interfaces must be taken into consideration in the interpretation of physical properties of multilayer Fe–Si systems.

Acknowledgments. This study was supported within the framework of the "Spintronics" Program of the Department of Physics of the Russian Academy of Sciences.

REFERENCES

1. M. N. Baibich, J. M. Broto, A. Fert, *et al.*, Phys. Rev. Lett. **61**, 2472 (1988).
2. R. E. Cambley and R. L. Stamps, J. Phys.: Condens. Matter. **5**, 3727 (1993).
3. A. E. Berkowitz, J. R. Mitchell, M. J. Carey, *et al.*, Phys. Rev. Lett. **68**, 3745 (1992).
4. V. P. Dragunov, I. G. Neizvestnyĭ, and V. A. Gridchin, *Grounds of Nanoelectronics: A Textbook* (Izd. NGTU, Novosibirsk, 2004) [in Russian].

5. S. N. Varnakov, A. A. Lepeshev, S. G. Ovchinnikov, *et al.*, Prib. Tekh. Éksp. **6**, 252 (2004).
6. E. E. Fullerton, I. K. Schuller, H. Vanderstraeten, and Y. Bruynserade, Phys. Rev. B **45**, 9292 (1992).
7. A. D. Balaev, *Physics of Magnetic Films: Collection of Scientific Works* (Irkutsk, 1980), Vol. 14, p. 171 [in Russian].
8. F. Keffer, in *Handbuch der Physik*, Vol. XVIII.2: *Ferromagnetism*, Ed. by H. P. J. Wijn (Springer, Berlin, 1966).
9. D. L. Mills and A. A. Maradudin, J. Phys. Chem. Solids **28**, 1855 (1967).
10. G. J. Strijkers, J. T. Kohlhepp, H. J. M. Swagten, and W. J. M. de Jonge, Phys. Rev. B **60**, 9583 (1999).
11. R. S. Iskhakov, N. A. Shepeta, S. V. Komogortsev, *et al.*, Fiz. Met. Metalloved. **95** (3), 37 (2003).
12. *Magnetic Properties of Metals: D-Elements, Alloys and Compounds*, Ed. by H. P. J. Wijn (Springer, Berlin, 1991), p. 190.
13. C. J. Smithells, *Metals Reference Book* (Butterworths, London, 1967), Vol. 2.
14. J. M. Gallego and R. Miranda, J. Appl. Phys. **69**, 1377 (1991).
15. R. Klasges, C. Carbone, W. Eberhardt, *et al.*, Phys. Rev. B **56**, 10801 (1997).

Translated by P. Pozdeev

Technical Physics Letters, Vol. 31, No. 11, 2005, pp. 951–954. Translated from Pis'ma v Zhurnal Tekhnicheskoĭ Fiziki, Vol. 31, No. 22, 2005, pp. 9–16.

Generalized Synchronization in Autooscillatory Media

A. A. Koronovskiĭ, P. V. Popov, and A. E. Hramov*

Saratov State University, Saratov, Russia

** e-mail: aeh@cas.ssu.runnet.ru*

Received May 30, 2005

Abstract—The phenomenon of generalized chaotic synchronization has been found in autooscillatory media described by the Ginzburg–Landau equations. A mechanism responsible for the establishment of generalized synchronization regimes in one-way coupled autooscillatory media exhibiting chaotic spatiotemporal behavior is proposed. The mechanism of generalized synchronization is described based on an analysis of a modified Ginzburg–Landau equation with an additional dissipative term. *© 2005 Pleiades Publishing, Inc.*

The process of the synchronization of chaotic oscillations in dynamical systems has been extensively studied in recent years [1, 2]. This phenomenon is both of basic importance and of considerable practical significance, in particular, for biology [3], hidden data transfer using chaotic carrier signals [4–6], control of microwave electronic systems [7], etc. According to the modern classification, there are several types of synchronous behavior in a system of coupled chaotic oscillators, including phase synchronization (PS) [2], generalized synchronization (GS) [8], intermittent lag (LS) [9] and GS regimes [10], and complete synchronization (CS) [12]. In recent years, it has been established that various types of chaotic synchronization can be considered as different forms of manifestation of the same laws governing the synchronous dynamics in coupled chaotic oscillators (see, e.g., [13, 14]). In particular, previously we have considered a new type of the synchronous behavior of chaotic oscillators called the time scale synchronization, which allows the aforementioned different types of synchronization to be generalized [15, 16].

One type of synchronous behavior that has received much attention is the GS of one-way coupled chaotic oscillators [8]. This type of synchronization implies that there exists a certain function $\mathbf{F}[\cdot]$ relating the states of the response ($\mathbf{x}_r(t)$) and drive ($\mathbf{x}_d(t)$) chaotic oscillators (with either continuous or discrete time) upon termination of the transient process, whereby these states are related as $\mathbf{x}_r(t) = \mathbf{F}[\mathbf{x}_d(t)]$. The form of the $\mathbf{F}[\cdot]$ function can be quite complicated, which means that a nontrivial procedure may be required for establishing this relation.

A convenient approach to the diagnostics of GS between the drive and response systems under consideration is offered by the auxiliary system method [17]. According to this method, an additional response system $\mathbf{x}_a(t_0)$ identical to the response system $\mathbf{x}_r(t)$ is introduced whose initial conditions $\mathbf{x}_a(t_0)$ are different from $\mathbf{x}_r(t_0)$. If the GS is absent, the vectors of both the response $\mathbf{x}_r(t)$ and auxiliary $\mathbf{x}_a(t)$ systems belong to the same chaotic attractor, but they are always different. In contrast, when the GS takes place, the relations $\mathbf{x}_r(t) = \mathbf{F}[\mathbf{x}_d(t)]$ and $\mathbf{x}_a(t) = \mathbf{F}[\mathbf{x}_d(t)]$ are valid and, hence, the states of the response and auxiliary systems upon termination of the transient process must be identical: $\mathbf{x}_r(t) \equiv \mathbf{x}_a(t)$. Thus, the identity of states of the response and auxiliary systems upon the termination of the transient process is a criterion of the existence of GS between the drive and response systems.

The GS phenomenon was previously studied in sufficient detail for the systems with small numbers of the degrees of freedom [8, 17, 18]. Recently, we described a method of GS diagnostics in such systems by considering a modified system with additional dissipation. At the same time, the GS in distributed systems is still insufficiently studied, although the phenomenon of synchronization in spatially distributed autooscillatory media exhibiting spatiotemporal chaos is of considerable general interest. Other types of synchronous behavior in spatially distributed systems have been studied and it was established that CS and PS can take place in coupled systems described by the Ginzburg–Landau and Kuramoto–Sivashinsky equations [1, 20–25], while the time scale synchronization was found in coupled electron-wave media [26]. Boccaletti *et al.* studied the chaotic synchronization in discrete distributed autooscillatory systems. As for the GS in distributed systems, this type of synchronous behavior was only revealed in a model describing chemical reactions [27]. Questions concerning the mechanisms by which the GS regime is established in coupled distributed autooscillatory systems remain open.

This Letter addresses the phenomenon of GS in one-way coupled active media described by the Ginzburg–Landau equations, which are standard models for investigations into the spatiotemporal chaos and the formation of structures in distributed systems.

1063-7850/05/3111-0951$26.00 © 2005 Pleiades Publishing, Inc.

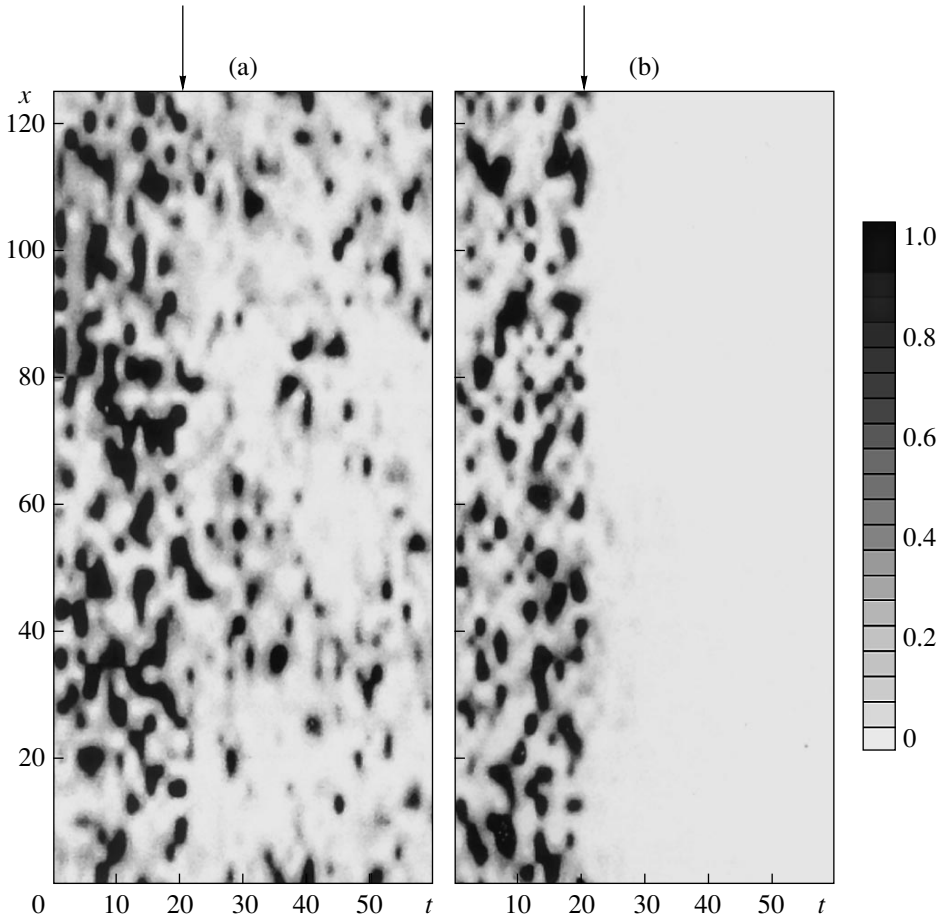

Fig. 1. Spatiotemporal evolution of the distribution of the difference of states of the response and auxiliary systems, $|u(x, t) - u_a(x, t|$, for two values of the coupling parameter: (a) $\varepsilon = 0.5 < \varepsilon_{GS}$, the GS is absent; (b) $\varepsilon = 1.0 > \varepsilon_{GS}$, the GS is present. The arrow indicates the switch-on ($t = 20$) of the coupling between the two systems.

Let us consider a model system of two active media described by the Ginzburg–Landau equations with one-way dissipative coupling,

$$\frac{\partial v}{\partial t} = v - (1 - i\alpha_d)|v|^2 v + (1 + i\beta_d)\frac{\partial v}{\partial x}, \quad v \in [0, L], \tag{1}$$

$$\frac{\partial u}{\partial t} = u - (1 - i\alpha_r)|u|^2 u + (1 + i\beta_r)\frac{\partial u}{\partial x} + \varepsilon(v - u), \quad u \in [0, L], \tag{2}$$

with the periodic boundary conditions. Here, Eq. (1) describes the distributed drive system, Eq. (2) refers to the distributed response system, and ε is the parameter characterizing the intensity of dissipative coupling with which the drive system acts upon every point of the response system. For this study, the parameters of systems under consideration are selected as follows: $\alpha_d = 1.5$, $\beta_d = 1.5$. $\alpha_r = 4.0$, $\beta_r = 4.0$, and $L = 40\pi$. It is known that autonomous distributed systems with such control parameters occur in a state of spatiotemporal chaos. The initial conditions were set randomly, and the numerical modeling of Eqs. (1) and (2) was carried out using an explicit computational scheme with the $\Delta t = 0.0002$ and $\Delta r = L/1024$.

GS probing using the method of an auxiliary system showed that, as the coupling parameter increases to a certain value $\varepsilon = \varepsilon_{GS}$, the two subsystems exhibit the GS regime. In this investigation, the auxiliary system was represented by Eq. (2) also coupled to Eq. (1), but with the initial conditions different from those for the original system. The observed behavior is illustrated in Fig. 1, which shows the spatiotemporal distributions of the difference of states of the response and auxiliary systems, $|u(x, t) - u_a(x, t)|$, for two coupling parameters. For $\varepsilon = 0.5 < \varepsilon_{GS}$, the GS is absent (Fig. 1a), while for $\varepsilon = 1.0 > \varepsilon_{GS}$, the GS is present (Fig. 1b). As can be seen, the difference of states of the response and auxiliary systems in the second case tends to zero in the entire space, which implies the establishment of the GS regime.

In order to elucidate the mechanism of the GS development, let us follow the approach described in [19] and consider a modified spatially distributed response system

$$\frac{\partial u_m}{\partial t} = u_m - (1 - i\alpha_r)|u_m|^2 u_m + (1 + i\beta_r)\frac{\partial u_m}{\partial x} - \varepsilon u_m, \quad u_m \in [0, L], \tag{3}$$

where $\varepsilon u(x, t)$ is the external action. Note that the term $\varepsilon u_m(x, t)$ introduces an additional dissipation into the modified Ginzburg–Landau equation.

An increase in the coupling parameter ε corresponds to an increase, on the one hand, in the amplitude of the external action on the response system and, on the other hand, in the dissipation in this active medium. The second factor results in a decrease in the amplitude of oscillations in the modified system and, at $\varepsilon = \varepsilon_0 = 1$, this distributed system features a stationary spatiotemporal regime (this ε value corresponds to vanishing of the u_m term in Eq. (3)). Figure 2 (curve *1*) shows a plot of the average square amplitude of oscillations $\langle u_m^2 \rangle$ described by the modified Ginzburg–Landau equation as a function of the coupling parameter. As can be seen, the amplitude exhibits a linear decrease with increasing the dissipative term εu_m (i.e., with increasing ε).

Previously, we demonstrated [19] that there are two possible mechanisms of the GS establishment in such one-way coupled systems. The first mechanism is related to the introduction of additional dissipation described by the dissipative term εu_m. In this case, the modified system either exhibits periodic oscillations or passes to a stationary regime. This mechanism is realized for $\varepsilon > \varepsilon_0 = 1$. However, in the system under consideration, the GS regime appears for $\varepsilon_{GS} = 0.72$ (as indicated by an arrow in Fig. 2), which is smaller than the value of $\varepsilon_0 = 1$ corresponding to a stationary regime: $\varepsilon_{GS} < \varepsilon_0$.

This behavior is related to the second possible mechanism of the GS establishment. Figure 2 (curve *2*) shows the dependence of the average square amplitude of an external (drive) signal $\langle(\varepsilon v)^2\rangle$, which is introduced into the response system, on the coupling parameter. As can be seen, the power of this signal increases with ε, and at $\varepsilon = \varepsilon_{GS}$ it is about three times as large as the amplitude of intrinsic oscillations in the response system. Evidently, the external action shifts the spatiotemporal state of the response system in the phase space toward the regions corresponding to strong dissipation. As a result, the intrinsic spatiotemporal chaotic dynamics of the response system described by the modified Ginzburg–Landau equation is suppressed and the GS regime is established at $\varepsilon_{GS} < \varepsilon_0$. It should be noted that, in the interval of $\varepsilon_{GS} < \varepsilon < \varepsilon_0$, the GS regime is established under the action of both mechanisms.

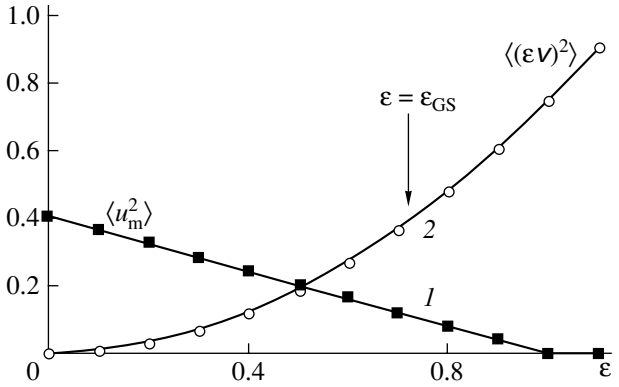

Fig. 2. Plots of the average power of (*1*) oscillations of the modified response system and (*2*) signal acting upon the response system versus coupling parameter ε.

To summarize, we have revealed the establishment of the GS regime in a system of one-way coupled Ginzburg–Landau equations and described mechanisms of the establishment of this synchronization in distributed autooscillatory systems. These mechanisms are based on the suppression of the intrinsic spatiotemporal chaotic dynamics as a result of the introduction of an additional dissipation into the spatially distributed response medium. The additional dissipation, first, directly leads to a decrease in the amplitude of intrinsic oscillations in the active medium and, second, shifts the spatiotemporal state of the response system in the phase space toward the regions corresponding to strong dissipation. The latter factor leads to an increase in the amplitude of the drive signal introduced into the response system, thus also suppressing the intrinsic signal dynamics. At a relatively large value of the coupling parameter, the former mechanism of the GS establishment predominates. There is a certain interval of coupling parameters featuring the joint action of both mechanisms.

Acknowledgments. This study was supported in part by the Russian Foundation for Basic Research (project no. 05-02-16273), the US Civilian Research and Development Foundation for the Independent States of the Former Soviet Union (CRDF award no. REC-006), and the "Dynasty" Foundation for Noncommercial Programs.

REFERENCES

1. S. Boccaletti, J. Kurths, G. Osipov, *et al.*, Phys. Rep. **366**, 1 (2002).
2. A. Pikovsky, M. Rosenblum, and J. Kurths, *Synchronization: Universal Concept in Nonlinear Sciences* (Cambridge Univ. Press, Cambridge, 2001; Tekhnosfera, Moscow, 2003).
3. L. Glass, Nature **410**, 277 (2001).
4. K. Murali and M. Lakshmanan, Phys. Rev. E **48**, R1624 (1993).

5. T. Yang, C. W. Wu, and L. O. Chua, IEEE Trans. Circuits Syst. **44**, 469 (1997).
6. A. S. Dmitriev and A. I. Panas, *Dynamical Chaos: New Information Media for Communication Systems* (Fizmatlit, Moscow, 2002) [in Russian].
7. D. I. Trubetskov, A. A. Koronovskiĭ, and A. E. Hramov, Izv. Vyssh. Uchebn. Zaved., Radiofiz. **47**, 343 (2004).
8. N. F. Rulkov, M. M. Sushchik, L. S. Tsimring, and H. D. I. Abarbanel, Phys. Rev. E **51**, 980 (1995).
9. M. G. Rosenblum, A. S. Pikovsky, and J. Kurths, Phys. Rev. Lett. **78**, 4193 (1997).
10. S. Boccaletti and D. L. Valladares, Phys. Rev. E **62**, 7497 (2000).
11. A. E. Hramov and A. A. Koronovskii, Europhys. Lett. **70**, 169 (2005).
12. L. M. Pecora and T. L. Carroll, Phys. Rev. Lett. **64**, 821 (1990).
13. S. Boccaletti, L. M. Pecora, and A. Pelaez, Phys. Rev. E **63**, 066219 (2001).
14. R. Brown and L. Kocarev, Chaos **10**, 344 (2000).
15. A. E. Hramov and A. A. Koronovskii, Chaos **14**, 603 (2004).
16. A. E. Hramov, A. A. Koronovskii, M. K. Kurovskaya, and O. I. Moskalenko, Phys. Rev. E **71**, 056204 (2005).
17. H. D. I. Abarbanel, N. F. Rulkov, and M. Sushchik, Phys. Rev. E **53**, 4528 (1996).
18. K. Pyragas, Phys. Rev. E **54**, R4508 (1996).
19. A. E. Hramov and A. A. Koronovskii, Phys. Rev. E **72** (2005) (in press).
20. Z. Tasev, L. Kocarev, L. Junge, and U. Parlitz, Int. J. Bifurcation Chaos Appl. Sci. Eng. **10**, 869 (2000).
21. L. Junge and U. Parlitz, Phys. Rev. E **62**, 438 (2000).
22. L. Kocarev, Z. Tasev, T. Stojanovski, and U. Parlitz, Chaos **7**, 635 (1997).
23. S. Boccaletti, J. Bragard, F. T. Arecchi, and H. Mancini, Phys. Rev. Lett. **83**, 536 (1999).
24. J. Bragard, S. Boccaletti, C. Mendoza, *et al.*, Phys. Rev. E **70**, 036219 (2004).
25. L. Kocarev, Z. Tasev, and U. Parlitz, Phys. Rev. Lett. **79**, 51 (1997).
26. A. E. Hramov, A. A. Koronovskii, P. V. Popov, and I. S. Rempen, Chaos **15**, 013705 (2005).
27. P. Parmananda, Phys. Rev. E **56**, 1595 (1997).

Translated by P. Pozdeev

Technical Physics Letters, Vol. 31, No. 11, 2005, pp. 955–958. Translated from Pis'ma v Zhurnal Tekhnicheskoĭ Fiziki, Vol. 31, No. 22, 2005, pp. 17–23.

A New Method for Estimating the Electroluminescence Parameters of ZnS:Mn Thin-Film Emitters

N. T. Gurin* and O. Yu. Sabitov

Ul'yanovsk State University, Ul'yanovsk, Russia

** e-mail: ido@ulsu.ru*

Received June 14, 2005

Abstract—We describe a new method for estimating the electroluminescence parameters of ZnS:Mn thin-film emitters based on an analysis of the experimental kinetic curves of the instantaneous internal quantum yield in the first half-period of the excitation voltage at a low-frequency for which the current buildup rate does not exceed the luminance growth rate. Using the proposed method, it is possible to evaluate (i) the probability of radiative relaxation in Mn^{2+} centers upon their electron-impact excitation, (ii) the time variation of the electron multiplication coefficient, (iii) the number of ionization events per electron escaped from the ionization region, and (iv) the length of the impact excitation of the emitting centers. *© 2005 Pleiades Publishing, Inc.*

The operation of electroluminescent thin-film (ELTF) emitters employing metal–insulator–semiconductor–insulator–metal (MISIM) structures based on manganese-doped zinc sulfide (ZnS:Mn) is related to the tunneling of charge carriers from the surface states at the cathode insulator–semiconductor (phosphor) interface in a strong electric field, the subsequent electron-impact excitation of Mn^{2+} centers, and the avalanche multiplication of carriers due to the impact ionization of intrinsic structural defects and impurities [1]. The main parameter characterizing the efficiency of electroluminescence (EL) in this system is the internal quantum yield η_{int}, which, in turn, depends on the electron-impact excitation cross section σ of Mn^{2+} centers, their concentration profile $N(x)$ in the phosphor layer, the effective thickness d_{pe} of this layer featuring the impact excitation of Mn^{2+} centers, and the probability P_r of the radiative relaxation of Mn^{2+} centers [2].

The instantaneous internal quantum yield can be expressed as [2]

$$\eta_{int}(t) = \sigma(t)N(x, t)d_{pe}(t)P_r(t), \quad (1)$$

where t is the current time of variation of the ELTF emitter excitation voltage. The cross section $\sigma(t)$ relatively weakly increases from 3×10^{-16} to 4×10^{-16} cm^2 with increasing field strength in the phosphor layer [1, 3]. The $N(x, t)$ profile depends on the ELTF emitter technology and is usually unknown. The effective EL layer thickness d_{pe} is determined by the difference between the phosphor layer thickness d_p and the thickness $x_c(t)$ of a nonradiative cathode layer, which varies from 20 nm for ELTF emitters obtained by atomic epitaxy to 200 nm for the structures grown by electron-beam deposition [1]; this value depends on the electric field distribution in the phosphor layer and is also usually unknown. The radiative relaxation probability P_r is determined by the ratio of the luminescence decay constant τ^* to the radiative relaxation time constant τ_r of Mn^{2+} centers,

$$P_r = \frac{\tau^*}{\tau_r}. \quad (2)$$

This ratio decreases with increasing concentration of Mn^{2+} centers [4, 5] and does not depend on the amplitude U_m and frequency f of the excitation voltage $U(t)$ [6]. The exact value of P_r is also unknown and varies, according to various estimates, from 0.22 to 0.4–0.5 [1, 7, 8].

The process of impact ionization of the intrinsic structural defects and impurities is characterized by the electron multiplication coefficient:

$$M(t) = \frac{n_p(t)}{n_{p0}(t)}, \quad (3)$$

where $n_p(t)$ is the number of electrons escaped from the region of strong field and $n_{p0}(t)$ is the number of electrons tunneling from the surface states at the cathode insulator–phosphor interface. The multiplication coefficient $M(t)$ can be related to the number of ionization events per electron escaped from the ionization region, which is defined as

$$m(t) = 1 - \frac{1}{M(t)}. \quad (4)$$

The electron-impact ionization of defects is a process that is competitive with the electron-impact excita-

1063-7850/05/3111-0955$26.00 © 2005 Pleiades Publishing, Inc.

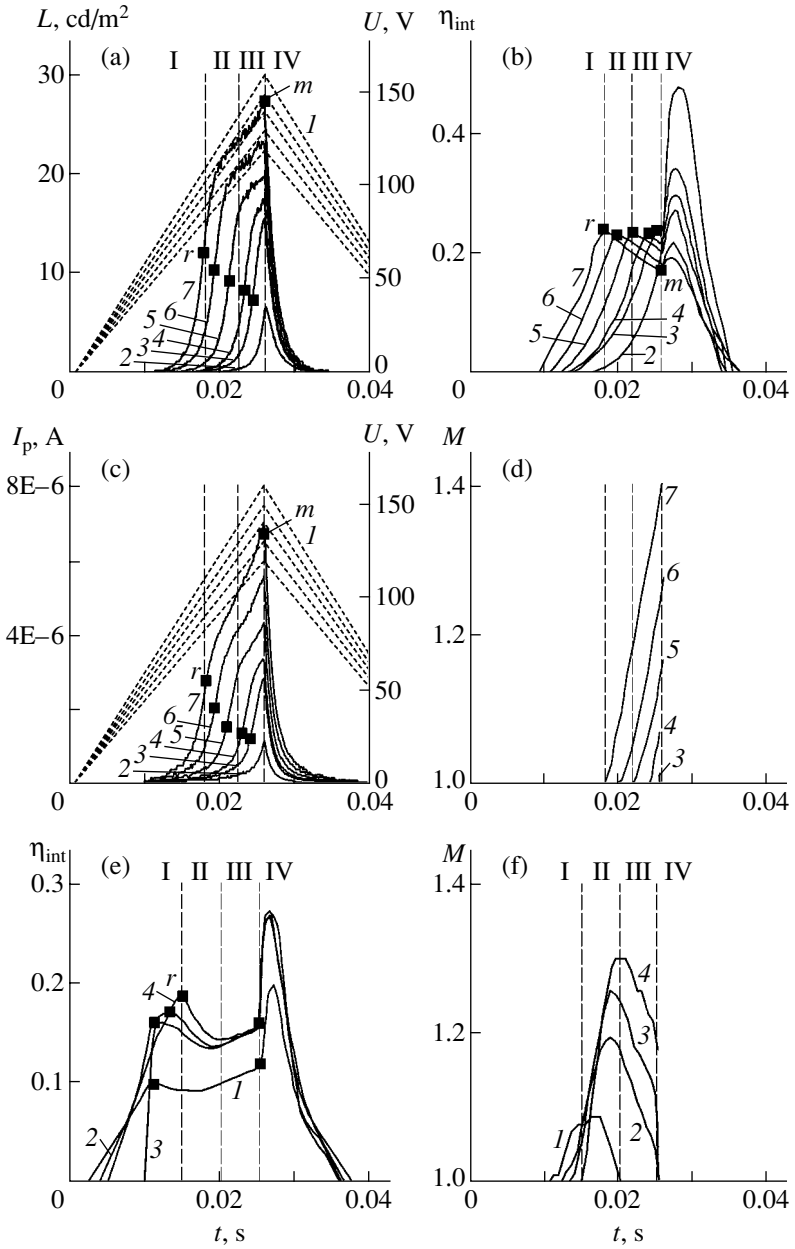

Fig. 1. The plots of (a) luminance $L(t)$, (b, e) intrinsic quantum yield $\eta_{int}(t)$, (c) phosphor layer current $I_p(t)$, and (d, f) electron multiplication coefficient $M(t)$ in ELTF emitters. (a–d) Sample 1, f = 10 Hz, T_s = 1 s (+Al variant): (*1*) $U(t)$, (*2–7*) U_m = 120, 125, 130, 140, 1540, 160 V, respectively (regions I–IV are indicated for U_m = 160 V); (e, f) sample 2, f = 10 Hz, U_m = 160 V (–Al variant): (*1–4*) T_s = 0.5, 5, 20, and 100 s, respectively (regions I–IV are indicated for T_s = 100 s).

tion of Mn^{2+} centers, which significantly limits the internal quantum yield η_{int} [8]. However, an exact description of the influence of impact ionization on the internal quantum yield η_{int} has not been developed thus far.

This study was aimed at estimating the values of P_r, $M(t)$, and $m(t)$ using the curves of $\eta_{int}(t)$ measured in experiment.

Let us consider the first half-period of the linearly increasing excitation voltage $U(t)$ applied to a MISIM structure (see Fig. 1a), in particular, the initial region I corresponding to a rapid buildup of the current $I_p(t)$ through the phosphor layer and of the luminance $L(t)$ (prior to the point "*r*," where the current growth rate begins to decrease). Previously, we demonstrated [2, 9] that the electric field strength in the phosphor layer in region I is homogeneously distributed due to the absence of the impact ionization of structural defects and impurities in this layer. In the subsequent regions II, III, and IV of the $I_p(t)$ profiles (Fig. 1a), the field in the

phosphor becomes inhomogeneous because of the space charge formation as a result of the ionization of defects in the phosphor, primarily of the intrinsic defects related to the sulfur vacancies (V_S^+) and zinc vacancies (V_{Zn}^{2-}) [8]. Denoting the concentration of ionized vacancies by $N_v(t)$ and assuming that each free electron participates on average in no more than one ionization event ($M < 2$), the number of electrons $n_p(t)$ escaped from the ionization region can be expressed as

$$n_p(t) = n_{p0}(t) + N_v(t). \quad (5)$$

We can neglect the electron recombination in the region of a strong electric field, since the electron flight time in the phosphor layer with a thickness of $d_p \approx 0.5$ μm at a drift velocity of 0.75×10^7 cm/s [10] is ~6.7×10^{-12} s, which is much shorter than the possible recombination time (3×10^{-3}–3.5×10^{-4} s [8]) at an excitation voltage frequency of 10 Hz. Therefore, all n_{p0} electrons escaped from the ionization region are involved in the impact excitation of Mn^{2+} centers. Taking into account relations (3)–(5), an expression for the instantaneous internal quantum efficiency can be written as

$$\eta_{int}(t) = \frac{N^*(t)P_r(t)}{n_p(t)} = \frac{N^*(t)P_r(t)}{M(t)n_{p0}(t)}, \quad (6)$$

where $N^*(t)$ is the number of excited Mn^{2+} centers. Equations (1) and (6) yield

$$\frac{N^*(t)}{n_{p0}(t)} = d_{pe}(t)\sigma(t)N(x, t). \quad (7)$$

The condition $N^*(t) = n_{p0}(t)$ determines the time t_r for which the length of the effectively emitting near-anode phosphor region $d_{pe}(t_r)$ is equal to the length l_{Mn} of the impact excitation of Mn^{2+} centers [5]:

$$d_{pe}(t_r) = l_{Mn} = \frac{1}{\sigma(t_r)N(x, t_r)}. \quad (8)$$

The time t_r corresponds to the maximum value of $\eta_{int}(t_r)$, whereby the impact ionization of defects in the phosphor layer is still absent, that is, to the boundary between regions I and II (Fig. 1a), where $M(t_r) = 1$ and

$$\eta_{int}(t_r) = P_r(t_r) = P_r = \text{const} \quad (9)$$

(it should be recalled that P_r is independent of U_m).

Assuming that $N^*(t) \approx n_{p0}(t)$ for $t > t_r$ in regions II and III (due to a relatively weak variation of the average field strength $F_p(t)$ in the phosphor layer [2, 9]), we obtain

$$\eta_{int}(t) \approx \frac{P_r}{M(t)} = P_r[1 - m(t)]. \quad (10)$$

Taking into account the homogeneous distribution of the electric field strength $F_p(t)$ in region I, the effective emission length in this region can be expressed as

$$d_{pe}(t) = d_p\left(1 - \frac{F_p(t_t)}{F_p(t)}\right) = d_p\left(1 - \frac{t_t}{t}\right), \quad (11)$$

where t_t is the threshold time of the field buildup at which the ELTP emitter begins to operate. Using expressions (8) and (11), we obtain the relation

$$d_{pe}(t_r) = l_{Mn} = d_p\left(1 - \frac{t_t}{t_r}\right), \quad (12)$$

where t_t and t_r are determined from the experimental $L(t)$ curve (Fig. 1a).

Thus, the values of P_r and $d_{pe}(t_r) = l_{Mn}$ at the point "*r*" (Fig. 1), as well as the $M(t)$ and $m(t)$ dependences in regions II and III, can be determined using the experimental kinetics of luminance $L(t)$ and current $I_p(t)$ and the $\eta_{int}(t)$ curves calculated as described in [8]:

$$\eta_{int}(t) = A\frac{L(t)}{I_p(t)}, \quad (13)$$

where A is a constant coefficient. In the approximation of monochromatic emission from an ELTP emitter surface uniformly radiating in all directions, this coefficient is given by the formula

$$A = \pi S_e q/k_0 f_\lambda h\nu,$$

where S_e is the emitter surface area (in our experiments, 1.77 mm^2), q is the electron charge, k_0 is the coefficient of radiation extraction (~0.17), f_λ is the luminous efficiency (~510 lm/W), and $h\nu$ is the photon energy (2.12 eV).

The experiments were performed using ELTP samples and methods described elsewhere [8]. The emitters were excited by the trains of two-period triangular pulses supplied from a generator at a repetition rate of 10 Hz, for which the current $I_p(t)$ buildup rate did not exceed the luminance $L(t)$ growth rate [8]. The time interval between excitation cycles was $T_s = 0.5$, 1, 5, 20, or 100 s and the pulse amplitude was varied within $U_m = 120$–160 V. In the first half-period, either positive or negative excitation half-waves can be applied to the upper electrode, which is referred to as the +Al and –Al regimes, respectively.

As can be seen from Figs. 1a and 1c, an increase in the excitation voltage amplitude to $U_m = 125$ V and above leads to the appearance of regions II and III in the $L(t)$ and $I_p(t)$ curves. The intrinsic quantum yield $\eta_{int}(t)$ reaches a maximum value at the point "*r*" (Fig. 1b) and then remains almost constant (being equal to P_r given by formula (9)) when U_m is increased from 125 to 160 V.

In regions II and III, the value of $\eta_{int}(t)$ decreases in accordance with Eq. (10). The values of P_r and l_{Mn} were found to be –0.24 and 0.27 μm in the +Al variant and ~0.11 and 0.26 μm for the –Al variant, respectively, being close to the data obtained in the experiments described in [8]. The maximum value of M at $t = t_m$ in the $M(t)$ curves (Fig. 1d) increases with U_m, reaching 1.48 (–Al) and 1.4 (+Al) at U_m = 160 V, also in agreement with the results obtained in [8]. The $m(t)$ curves have similar shapes with the absolute maxima of ~0.32 (–Al) and ~0.29 (+Al). A certain difference in P_r values is probably related to the nonuniform distribution of Mn^{2+} centers over the phosphor layer thickness, whereby their concentration is higher at the Al electrode. Figures 1e and 1f show the $\eta_{int}(t)$ and $M(t)$ curves measured for a different ELTP emitter (sample 2) using various excitation periods T_s. As can be seen from these data, the $M(t)$ curve measured in the –Al variant exhibits a maximum within regions II and III followed by decay, which can also be related to a nonuniform distribution of Mn^{2+} centers and structural defects in the phosphor layer, since the corresponding $M(t)$ curve observed in the +Al variant is analogous to the curves in Fig. 1d. The maximum values of $\eta_{int}(t)$ and $M(t)$ increase with T_s, which is explained by (i) the increasing degree of space charge neutralization in the phosphor layer in the pause between ELTP emitter excitations and (ii) the increasing homogeneity of field distribution in region I [2, 8, 9].

We believe that the proposed method can be used for determining the EL parameters of other phosphors featuring the intracenter emission.

Acknowledgments. This study was supported by the Presidential Program of Support for Leading Scientific Schools in Russia, project no. NSh-1482.2003.8.

REFERENCES

1. *Electroluminescence Sources*, Ed. by I. K. Vereshchagin (Énergoatomizdat, Moscow, 1990) [in Russian].
2. N. T. Gurin, A. V. Shlyapin, and O. Yu. Sabitov, Zh. Tekh. Fiz. **72** (2), 74 (2002) [Tech. Phys. **47**, 215 (2002)].
3. N. T. Gurin and Yu. V. Sabitov, Zh. Tekh. Fiz. **69** (5), 65 (1999) [Tech. Phys. **44**, 537 (1999)].
4. D. H. Smith, J. Lumin. **23**, 209 (1981).
5. R. Mach, in *Polycrystalline Semiconductors Physical Properties and Application*, Ed. by G. Harbeke (Springer, Berlin, 1985).
6. N. T. Gurin, A. V. Shlyapin, and O. Yu. Sabitov, Zh. Tekh. Fiz. **73** (4), 100 (2003) [Tech. Phys. **48**, 479 (2003)].
7. P. Mach and G. O. Mueller, Semicond. Sci. Technol. **6**, 305 (1991).
8. N. T. Gurin and D. V. Ryabov, Zh. Tekh. Fiz. **75** (1), 45 (2005) [Tech. Phys. **50**, 44 (2005)].
9. N. T. Gurin, O. Yu. Sabitov, and A. V. Shlyapin, Zh. Tekh. Fiz. **71** (8), 48 (2001) [Tech. Phys. **46**, 977 (2001)].
10. E. Bringuier, Philos. Mag. B **75**, 209 (1997).

Translated by P. Pozdeev

Technical Physics Letters, Vol. 31, No. 11, 2005, pp. 959–960. Translated from Pis'ma v Zhurnal Tekhnicheskoĭ Fiziki, Vol. 31, No. 22, 2005, pp. 24–28.

Measuring the Impedance of Magnetic Microwires in a Rectangular Waveguide

V. N. Berzhansky, V. I. Ponomarenko, V. V. Popov*, and A. V. Torkunov

Taurida National University, Simferopol, Ukraine

** e-mail: slava-popov@nextmail.ru*

Received June 20, 2005

Abstract—A method of determining the impedance of magnetic microwires in the microwave frequency range is proposed that is based on the measurement of a complex coefficient of microwave reflection from a sample placed into a shorted rectangular waveguide. The proposed method has been applied to the investigation of the effect of an external constant magnetic field on the impedance of a cobalt-rich microwire. *© 2005 Pleiades Publishing, Inc.*

Amorphous magnetic microwires (fibers) exhibit special physical properties that make such wires promising materials for numerous applications. For example, magnetic field sensors and radio-wave-absorbing structures make use of the natural ferromagnetic resonance and of the strong dependence of the impedance of ferromagnetic wires on an external dc magnetic field (giant magnetoimpedance effect) [1, 2]. In the microwave range, the impedance of microwires is usually measured with the aid of a coaxial line, where a sample of the microwire partly replaces the central conductor. The impedance is calculated in the quasi-static approximation from data on the complex reflection coefficient R measured using a vector network analyzer [3]. The requirement of obeying the quasi-static conditions implies that, for frequencies on the order of several GHz, the sample length must not exceed 1–2 mm, which makes the arrangement of samples in the coaxial cell a difficult task.

Previously, we proposed a waveguide method for impedance determination [4] that was based on the measurement, with the aid of a scalar network analyzer, of the moduli of the reflection and transmission coefficients of a microwire placed inside a matched rectangular waveguide. Unfortunately, the modulus of R amounted to several percent and was comparable with the intrinsic coefficient of reflection of the matched load, which resulted in a large relative error of determination of the reflection coefficient of the microwire and, hence, of its impedance.

This Letter describes a modified waveguide technique for determining the impedance of microwires that is free of the above disadvantage. The measurements are performed using a setup schematically depicted in Fig. 1. The system comprises a sweep generator, two identical 23 × 10-mm waveguide sections ($S1$ and $S2$, 0.425-m-long, each provided with a directional coupler, and separated by a 0.1-mm-thick symmetric inductive diaphragm with a 9-mm window), a sample holder consisting of two short waveguide sections ($D1$ and $D2$, 4.06- and 4.76-mm-long, respectively), and a shorted end section ($S3$, 10.02-mm-long). A glass-coated microwire sample fixed in the holder is perpendicular to the wide walls and spaced by x_0 = 11.5 mm from the narrow walls. This system is used to measure the multiresonance frequency dependence of the ratio $\Psi(\omega) = V_2/V_1$, where V_1 and V_2 are the output signals of scalar detectors of the directional couplers. The $\Psi(\omega)$ function can be processed using a method described in [5] to determine the reflection coefficient R. The microwire is positioned in the sample holder at x_0 = 11.5 mm with the aid of special grooves in $D1$ waveguide section and then clamped between $D1$ and $D2$ sections closely tightened with screws, whereby the glass shell is broken to ensure the electric contact of the wire with the waveguide. The magnetoimpedance mea-

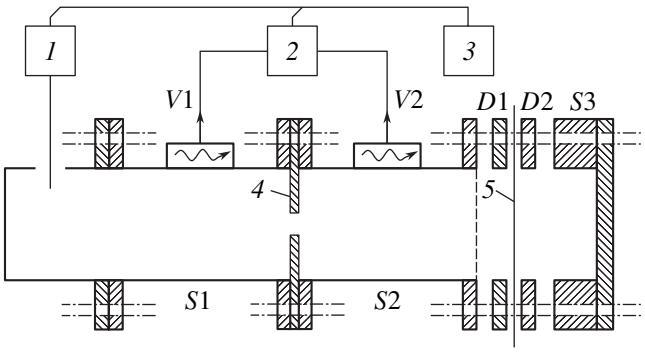

Fig. 1. Schematic diagram of the setup for the measurement of the impedance of microwires by the waveguide method: ($S1$, $S2$) identical waveguide sections; ($D1$, $D2$) sample holder; ($S3$) shorted end section; ($V1$, $V2$) directional couplers; (*1*) sweep generator; (*2*) scalar network analyzer; (*3*) computer; (*4*) inductive diaphragm; (*5*) microwire.

1063-7850/05/3111-0959$26.00 © 2005 Pleiades Publishing, Inc.

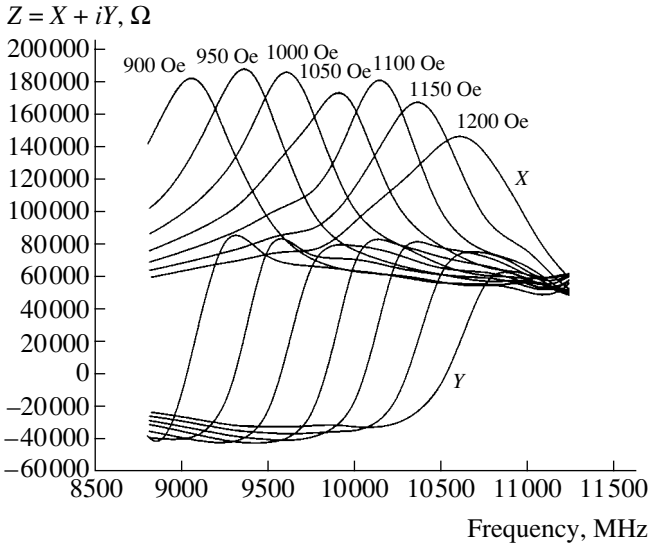

Fig. 2. Frequency dependences of the real (*X*) and imaginary (*Y*) parts of impedance *Z* for various values of the external constant magnetic field *H* (indicated at the curves).

surements are performed upon the application of an external constant magnetic field *H* along the wire axis, which is generated by a dc electromagnet.

In order to solve the problem of electromagnetic wave scattering on a microwire in a shorted rectangular waveguide, we have used an approach analogous to that described in [4, 6]. With a time-dependent factor selected in the form of $\exp(+i\omega t)$, the complex coefficient *R* of reflection in the plane of the waveguide cross section where the microwire is positioned has the following form:

$$R = -e^{2i\Gamma_1 l} - \frac{2(1-e^{2i\Gamma_1 l})^2 \sin^2\frac{\pi x_0}{a}}{\frac{2a\Gamma_1}{\omega\mu_0}Z + 2F(r) - F(2l+r) - F(2l-r)}, \quad (1)$$

$$F(s) = \sum_{n=1}^{\infty} \frac{\Gamma_1}{\Gamma_n} \sin^2\frac{n\pi}{a} x_0 \exp(i\Gamma_n s).$$

Here, Γ_m is the propagation constant for a wave of the H_{m0} type; *a* is the waveguide width; $r = d/2$, *d* is the wire diameter; *l* is the distance from the wire to the shorted section; $i = \sqrt{-1}$; μ_0 is the permeability of vacuum; and *Z* is the impedance. The absolute error of *R* determination in terms of formula (1) is estimated as described in [6]. By the order of magnitude, this error amounts to $(d/\lambda)^2$, where λ is the wavelength of radiation in the waveguide. For example, the relative error for $d \sim 10$ μm and $\lambda \sim 1$ cm is on the order of 10^{-6}. Using formula (1), it is possible to determine *Z* from the measured values of *R*. The convergence of series $F(s)$ can be improved through separation and analytical summation of the principal part.

The proposed method was used to measure the impedance of a $Co_{68.7}Fe_4Ni_1B_{13}Si_{11}Mo_{2.3}$ microwire with a diameter of $d = 8.2$ μm and a glass shell thickness of 2.5 μm. Figure 2 presents the frequency dependences of the real (*X*) and imaginary (*Y*) parts of *Z* for various values of the external constant magnetic field *H*. The effect of a glass shell on the *R* value is insignificant, since the displacement current in the shell is, according to estimates, several orders of magnitude lower than the current in the central conductor. As can be seen from Fig. 2, the frequency dependence of the impedance has a resonance character and the resonance frequency depends on *H*, which is explained by a ferromagnetic resonance in the microwire.

The relative errors ΔZ for *X* and *Y* were determined by introducing the absolute errors $\Delta|R| = 0.01$ and $\Delta \arg R = 1°$ in the modulus and phase of *R*, respectively, which correspond to the accuracy of the multiresonance method of *R* determination [5] and the precision of modern vector network analyzers. The ΔZ values estimated in this way did not exceed 5%.

To summarize, we have proposed a waveguide technique for determining the impedance of microwires in the microwave frequency range that provides a simpler experimental realization and a higher precision in comparison to the other known methods. The accuracy of impedance determination by this method is determined almost completely by the accuracy of measurements of the complex reflection coefficient in the waveguide, since formula (1) has been derived without using the quasi-static approximation. With the modern techniques of *R* measurements, the relative error of impedance measurements does not exceed 0.05.

REFERENCES

1. A. Zhukov, J. Magn. Magn. Mater. **242–245**, 216 (2002).
2. S. A. Baranov, Pis'ma Zh. Tekh. Fiz. **24** (14), 21 (1998) [Tech. Phys. Lett. **24**, 549 (1998)].
3. D. Ménard, M. Britel, P. Ciureanu, *et al.*, J. Appl. Phys. **81**, 4032 (1997).
4. V. I. Ponomarenko, V. N. Berzhanskiĭ, A. V. Torkunov, *et al.*, Izv. Vyssh. Uchebn. Zaved., Radioélektronika **32** (3), 38 (1989).
5. V. I. Ponomarenko and V. V. Popov, Prib. Tekh. Éksp., No. 1, 94 (2005) [Instrum. Exp. Tech. **48**, 78 (2005)].
6. L. Lewin, *Theory of Waveguides* (Halsted Press, New York, 1975).

Translated by P. Pozdeev

Technical Physics Letters, Vol. 31, No. 11, 2005, pp. 961–963. Translated from Pis'ma v Zhurnal Tekhnicheskoĭ Fiziki, Vol. 31, No. 22, 2005, pp. 29–35.

Chaotic Pulse Trains Generated by a Dynamical System Driven by a Periodic Signal

A. S. Dmitriev*, E. V. Efremova, and L. V. Kuz'min

Institute of Radio Engineering and Electronics, Russian Academy of Sciences, Moscow, Russia

** e-mail: chaos@cplire.ru*

Received May 20, 2005

Abstract—Chaotic pulse trains (rf pulses) can be generated by a dynamical system driven by a periodic signal. This possibility is demonstrated using a generator of chaotic oscillations with 2.5 degrees of freedom. By controlling the frequency of external action and selecting a constant bias (working point), it is possible to vary the width of rf pulses and their repetition rate within broad limits. © *2005 Pleiades Publishing, Inc.*

In recent years, chaotic radio pulses have been widely used as data carriers in wideband and ultrawideband communication systems [1–4]. A train of such pulses can be obtained by modulating a stationary signal at the output of a generator of chaotic oscillations. However, this method implies the constant operation of the source of chaos and, hence, has low energy efficiency (especially in the case of small duty cycles).

This paper reports on the possibility of generating trains of chaotic pulses by means of a periodic action upon a dynamical system. The task is to select the parameters of external periodic action so as provide for the excitation of chaotic oscillations only during a part of the period, thus simplifying the process and increasing the energy efficiency.

Let us use a source of chaotic oscillations representing the conventional chaotic signal generator with a bipolar microwave transistor as the active element (Fig. 1a). The generator employs a three-point capacitive scheme described by three ordinary differential equations [5, 6], with an additional low-pass *RLC* filter in the feedback chain. This filter increases the number of the degrees of freedom to 2.5 and provides additional possibilities for the synthesis of a desired power spectrum of chaotic oscillations. The external action upon the generator is produced by a source of alternating voltage in the power supply chain.

The model system is described by the following system of differential equations:

$$C_1\dot{V}_{CE} = I_{L2} - I_C,$$

$$C_3\dot{V}_{BE} = (V_E - V_{BE})/R_E - I_{L1} - I_B(V_{BE}),$$

$$C_2\dot{V}_A = I_{L1} - I_{L2} - \frac{C_2}{C_3}((V_E - V_{BE})/R_E - I_{L1} - I_B(V_{BE})), \quad (1)$$

$$L_1\dot{I}_{L1} = V_C - V_A - R_{L1}I_{L1},$$

$$L_2\dot{I}_{L2} = V_A + V_{BE} - V_{CE} - R_2I_{L2},$$

where $V_E = V_{DC} + V_{AC}\sin(2\pi ft)$; V_{DC} and V_{AC} are the amplitudes of the dc and ac components, respectively, of the external signal V_E (in the autonomous regime, $V_{AC} = 0$); f is the frequency of this signal; V_{CE} and V_{BE} are the collector–emitter and base–emitter voltages;

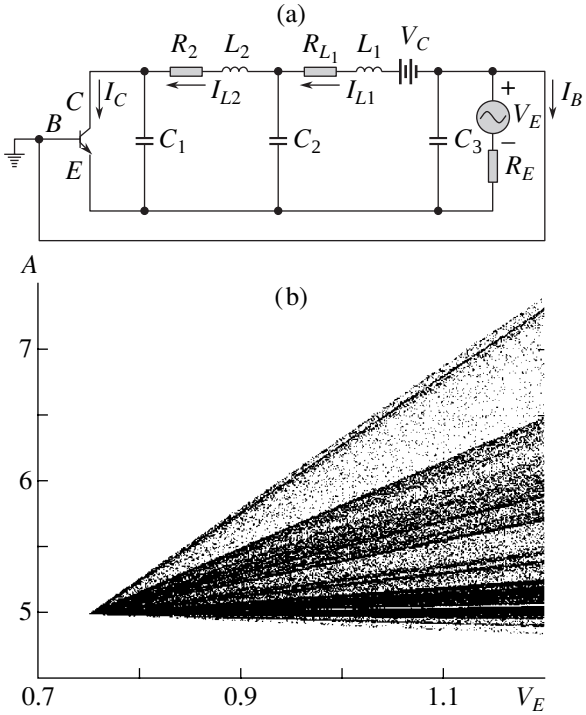

Fig. 1. A model chaotic generator with 2.5 degrees of freedom: (a) schematic diagram; (b) diagram of working regimes for V_C = 5 V, L_1 = 25 nH, L_2 = 2.5 nH, C_1 = 10 pF, C_2 = 1 pF, C_3 = 1.3 pF, R_{BE} = 200 Ω, R_E = 246 Ω, R_1 = 20 Ω, R_2 = 20 Ω, β = 425, V_T = 0.75 V. *A* denotes the local maxima of the V_A time series of the autonomous generator.

1063-7850/05/3111-0961$26.00 © 2005 Pleiades Publishing, Inc.

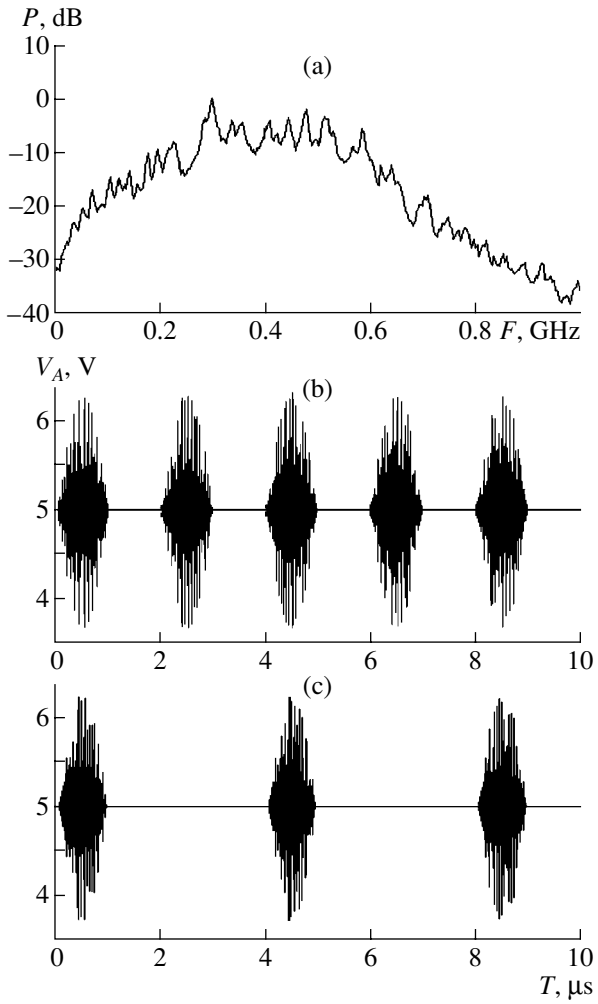

Fig. 2. The model generator operating under the action of an external modulating signal: (a) the typical output power spectrum of a train of chaotic pulses; (b, c) pulse trains (rf pulses) with the duty cycles 1/2 and 1/4, respectively.

V_A is the voltage at point A; V_C and V_E are the potential differences of the corresponding voltage sources; I_{L1}, I_{L2}, I_C, and I_B are the currents passing through the inductances L_1 and L_2, collector C, and base B, respectively; $I_C = \beta I_B$; and β is the transistor gain.

Below, the transistor operation in the model generator is described using a piecewise-linear approximation of the static current–voltage characteristic $I_B(V_{BE})$ of a bipolar transistor:

$$\begin{aligned} I_B &= 0, \quad \text{for} \quad V_{BE} \le V_T; \\ I_B &= (V_{BE} - V_T)/R_{BE}, \quad \text{for} \quad V_{BE} > V_T, \end{aligned} \tag{2}$$

where V_T is a threshold potential (~0.75 V) and R_{BE} is the resistance of the base–emitter junction. Oscillations in the system under consideration will be analyzed in terms of the variable voltage V_A.

Figure 1b shows a diagram of the working regimes A of the autonomous generator at various voltages versus the base–emitter voltage V_E. As can be seen from this diagram, the chaotic oscillations are generated at all V_E values above the threshold V_T. This circumstance is explained by the fact that a key parameter of the current–voltage characteristic, which determines the regime of oscillations, is the slope of the linear region of this characteristic. The bias voltage applied to the transistor only determines the characteristic amplitude of oscillations and serves as a normalizing factor on the passage from dimensional to dimensionless description of the model. In other words, the shape of the current–voltage characteristic is invariant with respect to a similarity transformation not changing the slope of the linear region, and this invariance accounts for the qualitatively similar regimes corresponding to the values of parameters obtained as a result of such a transformation.

Figure 2a presents an output power spectrum of the chaotic signal generator operating in an autonomous regime with the values of parameters indicated in the legend to Fig. 1 and a base–emitter voltage of $V_E = 1$ V. As can be seen, the main fraction of power is concentrated in the frequency band from 250 to 500 MHz.

Let us consider the operation of the generator under the action of an external harmonic signal producing a slow (in comparison to the characteristic frequency) periodic variation of the base–emitter voltage V_E. Calculations show that the presence of such a periodic (harmonic) signal leads to the modulation of chaotic oscillations with a period inversely proportional to the modulating signal frequency f. As the amplitude of the external signal is increased, the depth of modulation of the intrinsic chaotic oscillatory process also grows and eventually the output signal acquires the shape of trains of chaotic pulses. In this regime, the periods of time during which the chaotic oscillations are generated are separated by periods in which these oscillations are absent (Fig. 2b). The distance between trains (rf pulses) is determined by the period and amplitude of the external action and by the dc bias voltage V_{DC} on the transistor emitter.

From the standpoint of the regime of transistor operation, this behavior is related to the opening and closing of the p–n junction in the course of modulation, whereby the chaotic generation takes place when V_E exceeds the transistor threshold voltage V_T. Thus, by selecting the modulation frequency f, amplitude V_{AC}, and constant bias V_{DC}, it is possible to obtain chaotic pulse trains with a variable duty cycle. For example, Fig. 2b shows a fragment of the output time series observed when the generator is modulated by a signal V_E with the parameters $V_{DC} = V_T$, $V_{AC} = 0.25$ V, and $f =$ 500 kHz. This set of control parameters provides for obtaining chaotic pulse trains (rf pulses) at a duty cycle of 1/2. Figure 2c presents a fragment of the output time series observed when the same generator is modulated by a signal V_E with the parameters $V_{DC} = 0$, $V_{AC} = 1$ V, and $f = 250$ kHz, which yields chaotic pulse trains with

a duty cycle of 1/4. It should be noted that the current in the interval between adjacent chaotic pulses is close to zero, which significantly increases the energy efficiency of the proposed generator.

What are such chaotic pulse trains from the standpoint of nonlinear dynamics? On the time axis, there are periods featuring both regular behavior (intervals between rf pulses) and chaotic behavior (trains of chaotic pulses). An analysis of the Lyapunov exponents shows that regular periods correspond to negative values of the major Lyapunov exponent, whereas the periods filled with chaotic oscillations are characterized by positive average values of this exponent.

These features of the system dynamics are elucidated by an analysis of the data presented in Fig. 1b. This diagram shows that, when a periodic external action is absent and $V_E > V_T$, the system exhibits chaotic oscillations (this is confirmed by direct calculation of the Lyapunov exponent). The periodic action was produced at a frequency well below the characteristic frequency of intrinsic oscillations. From the standpoint of the dynamical properties of the system under consideration, the external action is quasi-stationary. According to this, when the variable component of V_E exceeds 0.75 V, the system also occurs in a chaotic regime, which is confirmed by the generation of chaotic pulses.

It is interesting to note that the system under consideration can also generate the trains of virtually identical pulses. This behavior is observed in the case of short pulses separated by rather long time intervals, whereby the average major Lyapunov exponent in the time intervals with pulses is positive. However, since the initial conditions for the pulses are almost identical, small distinctions of these conditions do not lead to significant differences between the trajectories.

Using the effects described above, it is possible to generate ultrawideband pulse trains (rf pulses) with preset pulse widths and duty cycles at a controlled continuous signal power spectrum.

Acknowledgments. This study was supported by the Russian Foundation for Basic Research, project no. 05-02-17667A.

REFERENCES

1. A. S. Dmitriev, B. E. Kyarginskiĭ, A. I. Panas, *et al.*, Radiotekh. Élektron. (Moscow) **46**, 224 (2001).
2. A. S. Dmitriev and A. I. Panas, *Dynamical Chaos: New Information Media for Communication Systems* (Fizmatlit, Moscow, 2002) [in Russian].
3. A. S. Dmitriev, B. E. Kyarginskiĭ, A. I. Panas, *et al.*, Pis'ma Zh. Tekh. Fiz. **29** (2), 21 (2003) [Tech. Phys. Lett. **29**, 72 (2003)].
4. A. S. Dmitriev, B. Ye. Kyarginsky, A. I. Panas, *et al.*, Int. J. Bifurcation Chaos Appl. Sci. Eng. **13**, 1495 (2003).
5. M. V. Kapranov, V. N. Kuleshov, and G. M. Utkin, *Oscillation Theory in Radio Engineering: A Student's Textbook* (Nauka, Moscow, 1984) [in Russian].
6. M. Kennedy, IEEE Trans. Circuits Syst. **41**, 771 (1994).

Translated by P. Pozdeev

Technical Physics Letters, Vol. 31, No. 11, 2005, pp. 964–966. Translated from Pis'ma v Zhurnal Tekhnicheskoĭ Fiziki, Vol. 31, No. 22, 2005, pp. 36–41.

Unstable Plastic Flow in a Zirconium Alloy

T. M. Poletika*, G. N. Narimanova, and S. V. Kolosov

Institute of Strength Physics and Materials Science, Siberian Division, Russian Academy of Sciences, Tomsk, 634055 Russia

** e-mail: poletm@ispms.tsc.ru*

Received June 20, 2005

Abstract—Unstable plastic flow has been observed in the parabolic stage of work hardening of a zirconium alloy, which was manifested by periodic variations of a spatiotemporal pattern of the local strain distribution. A synergistic model explaining this behavior is proposed according to which the plastic flow evolution in the final stage is considered as an unstable limiting cycle of the dynamical system. © *2005 Pleiades Publishing, Inc.*

It has been experimentally demonstrated [1, 2] that the deformation of single- and polycrystalline materials might be accompanied by the development of both wave and stationary spatiotemporal patterns of strain localization. The appearance of each particular pattern is determined by the regime of plastic flow and by the law of work hardening operative in the corresponding stage of deformation. Our recent investigations [3, 4] showed that stationary patterns of strain localization characterized by a constant spatial period λ are typical only of that part of the parabolic stage of work hardening ($\sigma \sim \varepsilon^n$) where $n \geq 0.5$. The other parts of this stage, corresponding to $n < 0.5$, are characterized by the motion of strain localization foci with variable λ, which proceeds up to the end of the parabolic stage [3–5].

This Letter presents the results of our investigation into the development of strain localization in the parabolic stage of plastic flow and in the stage of prefracture of a technical polycrystalline zirconium-rich alloy (Zr–1 wt % Nb–1.3 wt % Sn–0.4 wt % Fe) under uniaxial extension conditions. This process is accompanied by unstable plastic straining and leads to the neck formation. Knowledge of the laws governing the appearance and development of plastic strain macrolocalization, which leads to the instability of plastic flow and to material breakage in the course of plastic shaping, is of considerable practical significance. In particular, this knowledge can help to evaluate the margin of technological plasticity of zirconium alloys in which large strains are developed in the course of processing [6].

In order to determine the character of evolution of the spatiotemporal pattern of strain distribution, we have studied by speckle interferometry [1] the local deformation at the strain macrolocalization foci immediately in the course of plastic flow. Using these data, we determined both the total local elongation (by integrating the ε_{xx} component of the plastic strain tensor over the area occupied by a given localization focus) and the local strain increment $\Delta\varepsilon_{xx}$ in the given focus. The summation of ε_{xx} values in the parabolic stage of loading revealed three zones of intense strain localization. In these zones, the local strain increments $\Delta\varepsilon_{xx}$ were determined as differences between the integral ε_{xx} values corresponding to every 0.2% step of the total strain. It was found that the ε_{xx} increases more rapidly in one of the three zones, which transforms first into a focus of prefracture and then into a neck. A similar evolution of the strain localization focus accompanied by the appearance of several "inactive" necks, one of which then became "active" (stable), was previously observed during the extension of In–Pb alloys [6].

An analysis of the patterns of plastic strain localization corresponding to various parts of the parabolic curve showed that the distance λ between the localization foci value is constant for $n \geq 0.5$, whereas for $n < 0.5$, this distance exhibits periodic variations in the course of straining (Fig. 1, curve *1*). The experiments also revealed a correlation between the periodic variation of the spatial period λ of the strain macrolocalization and the periodic change in the local elongation increment $\Delta\varepsilon_{xx}$ in the foci of intense strain localization. Figure 1 (curve *2*) shows the behavior of $\Delta\varepsilon_{xx}$ in that focus of strain localization, from which the neck is subsequently formed.

Since the spatial period λ of strain localization is the distance between the active strain localization foci [1], we may assume that the number of such foci can be determined in the general case as $N = L/\lambda$, where L is the length of the working part of a sample. From this we infer that a decrease in N is accompanied by the intense accumulation of local strain or, in other words, a smaller N corresponds to a greater intensity of strain localization characterized by $\Delta\varepsilon_{xx}$.

The experimental data indicate that it is the correlated periodic variation of the spatial period λ of strain localization and the strain intensity $\Delta\varepsilon_{xx}$ at the localiza-

1063-7850/05/3111-0964$26.00 © 2005 Pleiades Publishing, Inc.

tion focus that determines the instability of plastic flow in the parabolic stage of deformation of the zirconium alloy studied, which leads eventually to the formation of a single localization focus, a precursor of the future neck.

The results obtained in this study correspond to notions about a spatiotemporal periodicity of the process of plastic strain localization [7, 8], according to which the instability of plastic flow is a consequence of a local increase in the strain rate leading to a local hardening in the strain localization zone. The corresponding growth of yield stress at this site leads to a retardation of the process of strain localization and to a more uniform character of sample shaping. One cycle of such hardening and loosening corresponds to one period observed in the part of the parabolic curve with $n < 0.5$.

The curve of $\lambda(t)$ presented in Fig. 1 is characteristic of a rigid loss of stability, whereby the system exhibits a jumplike transition from a stationary state to an oscillatory quasi-periodic regime corresponding to a limiting cycle of the dynamical system [9]. Variation of the strain localization pattern in this case can be described by a trajectory in the phase space, whereby the motion of an imaging point along this trajectory corresponds to the temporal evolution of a deformed sample (Fig. 2). This trajectory reflects a relationship between $\Delta\varepsilon_{xx}$ and N in the course of straining (i.e., with time). As can be seen from Fig. 2, an increase in the total strain corresponds to the system evolving along one turn of the spiral, whereby the density N of the strain localization foci first decreases (as a result of their merging together) and then increases again. Accordingly, the intensity of strain localization $\Delta\varepsilon_{xx}$ at the foci initially grows and then drops as a result of the local strain redistribution between the appearing additional strain localization zones, which corresponds to a more uniform sample shaping. One turn of the spiral trajectory corresponds to a part of the parabolic curve with $n < 0.5$ and represents one step in the plastic flow localization in the given alloy sample. The oscillatory regime is unstable, since the trajectory goes away from the limiting cycle [9] and tends to a point corresponding to the system with a single strain localization focus, a neck precursor (Fig. 2).

The stability of plastic flow along a phase trajectory depends on the character of work hardening and the margin of plasticity of a given material. In particular, the stress–strain curve for many plastic materials is restricted to a parabolic stage of work hardening with $n \approx 0.5$, which eventually leads to an increase in the strain amplitude at one of the stationary strain localization foci and its subsequent transformation into a neck [2]. If the parabolic curve has at least one part with $n < 0.5$, then one cycle of a quasi-periodic variation of λ is possible, such as that recently observed in a polycrystalline Fe–Si alloy [10].

Thus, the experimental data obtained in this study allow us to conclude that the evolution of a nonequilibrium system in the final stages of plastic flow is characterized by a loss of stability with the formation of a limiting cycle, the stability of which is determined by the capacity of a given material for plastic shaping.

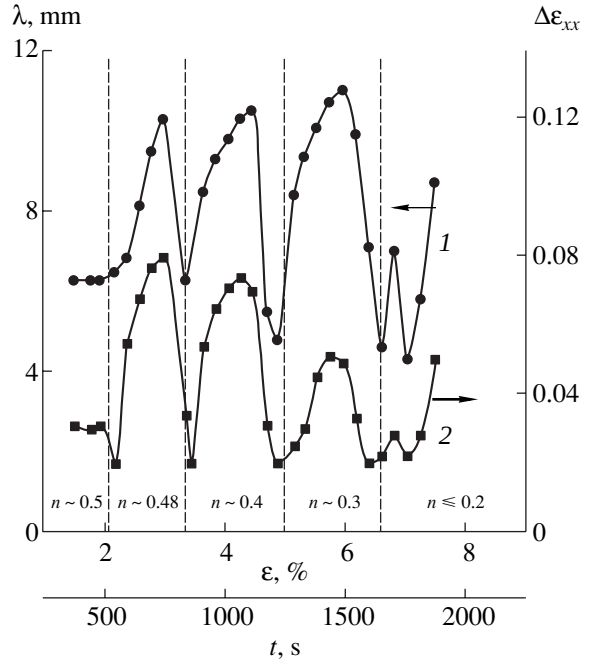

Fig. 1. Plots of (*1*) the spatial strain localization period λ and (*2*) the local elongation increment $\Delta\varepsilon_{xx}$ in the region of a prefracture focus versus the total strain ε for a zirconium alloy.

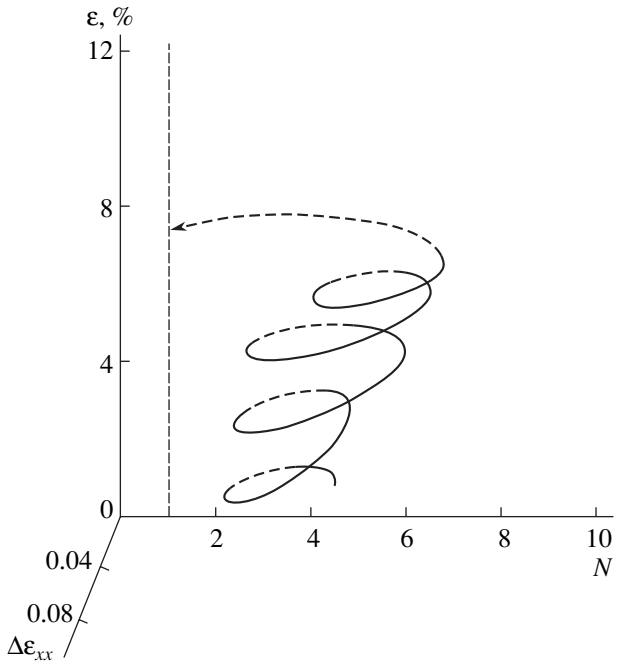

Fig. 2. A schematic phase trajectory describing the evolution of strain localization in a zirconium alloy.

REFERENCES

1. L. B. Zuev, Ann. Phys. **10**, 965 (2001).
2. L. B. Zuev, V. I. Danilov, and B. S. Semukhin, Usp. Fiz. Met. **3**, 237 (2002).
3. T. M. Poletika, V. I. Danilov, G. N. Narimanova, *et al.*, Zh. Tekh. Fiz. **72** (9), 57 (2002) [Tech. Phys. **47**, 1125 (2002)].
4. L. B. Zuev, V. I. Danilov, T. M. Poletika, and S. A. Barannikova, Int. J. Plast. **20**, 1227 (2004).
5. L. B. Zuev, T. M. Poletika, and G. N. Narimanova, Pis'ma Zh. Tekh. Fiz. **29** (12), 74 (2003) [Tech. Phys. Lett. **29**, 519 (2003)].
6. P. J. Wray, J. Appl. Phys. **41**, 3347 (1970).
7. A. A. Presnyakov, *Localization of Plastic Strain* (Mashinostroenie, Moscow, 1983) [in Russian].
8. A. S. Zaimovskii, A. V. Nikulina, and N. G. Reshetnikov, *Zirconium Alloys in Nuclear Energetics* (Énergoatomizdat, Moscow, 1994) [in Russian].
9. V. I. Arnold, *Catastrophe Theory* (URSS, Moscow, 2004; Springer-Verlag, Berlin, 1986).
10. S. A. Barannikova, V. I. Danilov, and L. B. Zuev, Zh. Tekh. Fiz. **74** (10), 52 (2004) [Tech. Phys. **49**, 1296 (2004)].

Translated by P. Pozdeev

Technical Physics Letters, Vol. 31, No. 11, 2005, pp. 967–968. Translated from Pis'ma v Zhurnal Tekhnicheskoĭ Fiziki, Vol. 31, No. 22, 2005, pp. 42–46.

Analysis of the Dynamic Characteristics of a Vacuum System

V. V. Savransky[a,*], R. A. Nevshupa[a], E. A. Deulin[a], and A. A. Avdienko[b]

[a] *Bauman Moscow State Technical University, Moscow, Russia*

[b] *METIS State Unitary Enterprise, Moscow, Russia*

* *e-mail: savransky@bmstu.ru*

Received June 22, 2005

Abstract—The gas pressure variation in a vacuum system featuring dynamic gas evolution in the form of a sequence of rectangular pulses has been experimentally studied. The observed behavior can be described in terms of a model developed previously. © *2005 Pleiades Publishing, Inc.*

In solving problems related to vacuum technology, it is necessary to analyze the dynamics of the total and partial gas pressures in a given vacuum system on the real time scale. One important problem is the *in situ* diagnostics of friction couples operating in vacuum. A system of such diagnostics developed at the Bauman Moscow State Technical University measures and analyzes the flow of gas evolved from a sliding or rolling friction couple and, using known relations, estimates the degree of wear, and assesses the technical state of the assembly [1]. Previously, it was shown [2–8] that the gas evolution during friction is a substantially nonstationary process representing a random sequence of pulses with certain distributions of the pulse amplitude and width. This character of gas evolution is related to the contact mechanics between rough surfaces of the two bodies, whereby each pulse of gas evolution corresponds to the interaction of one pair of protruding microsummits of the contacting surfaces.

The main problem in the abovementioned diagnostic system is related to determining the flux of evolved gases as a function of time, which has to be calculated from the curve of pressure variation measured in a given vacuum system in the course of friction. Previously, we established that the use of analytical models for particular forms of the initial gas flux variation offers a number of advantages to the universal methods of data processing with the use of functional transformations. An analytical model describing variations of the total and partial gas pressures $p(t)$ in a vacuum system for one of the main forms of gas evolution—meander—was recently described in [9]. This model describes the pressure in a dimensionless form, which makes it applicable to vacuum systems of all types. The results of modeling showed that a vacuum system can be considered as an aperiodic link, whereby the $p(t)$ function appears either as a sequence of peaks or as a smooth curve (representing unresolved peaks), depending on the parameters of the gas evolution process and on the vacuum system characteristics [1].

In order to verify the aforementioned model, we have modified the experimental setup described in [1] and performed a series of experiments as described below. The vacuum chamber had a volume of $V = 40.4$ liters and the effective pumping rate determined by the constant pressure technique was $S = 71$ l/s, so that the characteristic time constant of the vacuum system was $\tau_0 = V/S = 0.57$ s. The vacuum system was preliminarily evacuated to 1.3×10^{-3} Pa. The gas pulses were produced with the aid of a piezoelectric gas leak valve with a system of flexible control over the valve opening and closing process and the total gas flow. The valve opening and closing times could be varied using a set of resistors. In order to decrease the role of the dependence of the pumping rate on the pressure and to facilitate the pressure monitoring, the maximum gas flow rate Q_m^* was selected so that the pressure varied by no more than one order of magnitude and the pressure could be monitored without switching the gauge from one scale to another.

It was most interesting to study the behavior of gas pressure in the system in the course of periodic gas evolution pulses with a period within $0.1\tau \geq T_t \geq 10\tau$. In experiments, we varied the gas evolution pulse duration b at a constant period T_t (Fig. 1b). Figure 1b shows a sequence of control pulses U_{pz} applied to the piezoelectric gas leak valve, which correspond to the pulses of gas evolution, and Fig. 1a shows the corresponding pressure response. The amplitude A of pressure pulses and the maximum (p_{max}) and minimum (p_{min}) pressures exhibited nonlinear variation depending on the pulse duration b at $T_t = 16$ s. As the gas pulse duration was increased, the peak pressure gradually increased to a maximum value (p_{max}), while a minimum pressure between the peaks also increased from the background pressure level (p_0) to a stable value (p_{min}).

Since the increase in p_{min} was achieved with a delay relative to the growth in p_{max}, the peak amplitude initially increased to a maximum (for $b = 0.5T_t$) and then decreased. It is interesting to note that the increase in b was accompanied by a significant change in shape of the pressure peaks. The pressure peaks changes so as to remain symmetric relative to the central level: the peaks

1063-7850/05/3111-0967$26.00 © 2005 Pleiades Publishing, Inc.

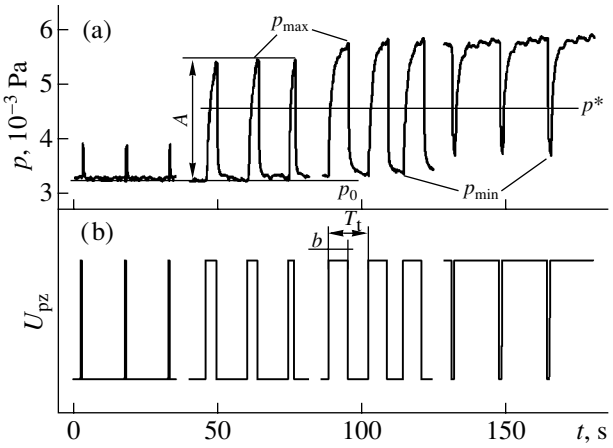

Fig. 1. (a) Variations of the total pressure p in the course of pulsed gas evolution via a piezoelectric gas-inlet device. (b) A sequence of control voltage pulses U_{pz} with increasing duration b = 0.5, 4, 8, and 15 s at a constant period T_t = 16 s.

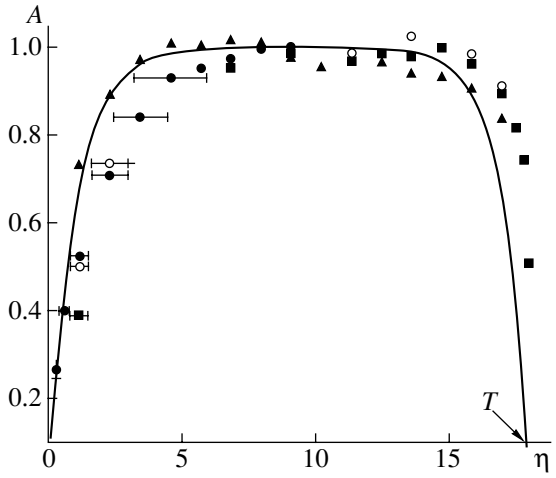

Fig. 2. A plot of the pressure pulse amplitude A versus gas evolution pulse duration η (in the dimensionless variables). Points present the experimental data; the curve shows the results of model calculations using formula (1).

corresponding to a certain b value appear as mirror reflections of the peaks corresponding to the pulse duration T_t–b relative to the horizontal axis $p^* = (p_{max} + p_{min})/2$. This explains the symmetry of the function $A = f(b)$ relative to the point $b = 0.5T_t$. Thus, the amplitude of the pressure peaks in the indicated interval of b and T_t is determined by the minimum of the two values, b or T_t–b, which is related to the equal time constants of the transient processes of pressure equilibration upon opening or closing of the leak valve.

In order to compare the experimental data with the results of model calculations, the experimental values were converted into the dimensionless form [9]: the dimensionless pressure was calculated as $\rho = (p - p_0)S/Q_m^*$ and the dimensionless time, as $\tau = tS/V$. Figure 2 shows a comparison of the experimental behavior (points) to the theoretical curve calculated for the given experimental conditions using the following formula [9]:

$$A = f_A(T, \eta) = \frac{\exp\eta - 1}{\exp T - 1}\left(\frac{\exp T}{\exp\eta} - 1\right),$$

where η and T are the dimensionless analogs of b and T_t, respectively. As can be seen, the agreement between theory and experiment is generally good, but there are some systematic deviations: for $b < 0.5T_t$, the measured peak pressure is lower than the calculated values, whereas for $b > 0.5T_t$ the experimental points occur above the theoretical curve. These discrepancies are probably related to a nonideal operation of the piezoelectric gas leak valve, namely, to a finite time of opening and closing (not taken into account in the model calculations). The finite valve opening time makes the real gas evolution pulse duration shorter, which is especially significant for small b values and leads to a decrease in the pressure amplitude. By the same token, the finite closing time makes the real gas evolution pulse duration longer and the gas amplitude greater than the theoretical values, which is more pronounced for large b values.

Conclusions. The obtained experimental data are consistent with the results of modeling. As the gas evolution pulse duration increases, both maximum and minimum pressures gradually increase, but the former pressure grows faster than the latter for $b < 0.5T_t$ and slower, for $b > 0.5T_t$. As a result, the pressure peak amplitude is maximum at $b = 0.5T_t$. On the passage through the point $b = 0.5T_t$, the pressure peaks are symmetric relative to the level of $p^* = (p_{max} + p_0)/2$.

Subsequent experiments will be performed with various gases and different forms of the gas evolution function.

Acknowledgments. This study was performed within the framework of the program "Development of the Research Potential of the High School-2005" supported by the Ministry of Education and Science of the Russian Federation.

REFERENCES

1. E. A. Deulin and A. G. Peresad'ko, Kontrol'. Diagnostika, No. 5, 21 (1998).
2. P. Řepa and M. Rott, Vacuum **48**, 775 (1997).
3. A. G. Peressadko, R. A. Nevshupa, and E. A. Deulin, Vacuum **64**, 451 (2002).
4. R. A. Nevshupa, J. L. de Segovia, and E. A. Deulin, Vacuum **53**, 295 (1999).
5. R. A. Nevshupa and J. L. de Segovia, Vacuum **64**, 425 (2002).
6. P. Řepa and D. Orálek, Vacuum **53**, 299 (1999).
7. J. T. Dickinson, L. C. Jensen, and M. R. McKay, J. Vac. Sci. Technol. A **4**, 1648 (1986).
8. J. T. Dickinson, L. C. Jensen, and S. C. Langford, Phys. Rev. Lett. **66**, 2120 (1991).
9. R. A. Nevshupa, J. L. de Segovia, A. G. Peressadko, *et al.*, Vacuum **69**, 477 (2003).

Translated by P. Pozdeev

Technical Physics Letters, Vol. 31, No. 11, 2005, pp. 969–972. Translated from Pis'ma v Zhurnal Tekhnicheskoĭ Fiziki, Vol. 31, No. 22, 2005, pp. 47–55.

Temperature Dependence of the Tensile Strength of Polymers and Metals at Elevated Temperatures

V. I. Vettegren[a,*], V. B. Kulik[a], and S. V. Bronnikov[b]

[a] *Ioffe Physicotechnical Institute, Russian Academy of Sciences, St. Petersburg, 194021 Russia*

[b] *Institute of Macromolecular Compounds, Russian Academy of Sciences, St. Petersburg, 199004 Russia*

** e-mail: Victor.Vettegren@mail.ioffe.ru*

Received May 17, 2005; in final form, July 14, 2005

Abstract—We have studied the temperature dependence of the tensile strength for polymers at temperatures above the glass transition temperature and for metals, above about half of the melting temperature. An empirical relation is found between the strength of these materials, the temperature, and the time to fracture. © *2005 Pleiades Publishing, Inc.*

Introduction. As is known [1–7], the time to fracture (lifetime) τ of metals, crystals, polymers, and other solids is related to the temperature T and the tensile strength σ by the Zhurkov equation:

$$\tau = \tau_0 \exp\frac{U}{kT} = \tau_0 \exp\frac{U_0 - \gamma\sigma}{kT}, \quad (1)$$

where $\tau_0 \approx 10^{-13}$ s, $U = U_0 - \gamma\sigma$ is the activation energy for the rupture of interatomic bonds under the action of thermal fluctuations, U_0 is the value of this energy at $\sigma \longrightarrow 0$, $\gamma = \partial U/\partial\sigma$ is a parameter related to the overstress coefficient and the activation volume of bond rupture, and k is the Boltzmann constant. Equation (1) has a clear physical meaning: the fracture takes place as a result of the accumulation of fractured bonds, and the activation energy for this fracture decreases by $\gamma\sigma$ under the action of mechanical stresses.

The initial activation energy U_0 is equal to the energy of dissociation of interatomic bonds and can be determined from independent measurements. Therefore, for determining the lifetime of a material for the given temperature and load, it is only necessary to determine the value of γ. As is known, this parameter depends on the defect structure of solids [4–6]. When the structure is subject to changes, the dependence of the lifetime on the temperature and stress becomes more complicated. In the presence of tensile stresses at elevated temperatures determined by the conditions $T > T_g$ for unoriented polymers and $T \geq 0.5T_m$ for non-strain-hardened metals (where T_g is the glass transition temperature and T_m is the melting temperature), these materials exhibit deviations from Eq. (1) [1–7]. These deviations are related to the fact that the prefracture strain under such modified conditions sharply increases and the γ value decreases [4–7].

It was demonstrated [8, 9] that the dependence of the lifetime on the temperature and stress for polymers and metals at elevated temperatures can be described by the following empirical relation:

$$\tau = \tau_0 \left(\frac{\sigma_*}{\sigma}\right)^m \exp\frac{U_0}{kT}, \quad (2)$$

where σ_* and m are certain constant "fitting" parameters. In contrast to the quantities entering into the Zhurkov equation, relation (2) contains two empirical parameters whose meaning is unclear. Use of this equation for estimating the lifetime of materials also meets additional difficulties, since both these parameters (σ_* and m) must be preliminarily determined, as opposed to one (γ) in the case of the Zhurkov equation.

Previously, we studied the temperature dependence of the strength of adhesion between epoxy-rubber glues and Steel 45 at temperatures $T > T_g$ [10] and established that Eq. (2) well described the experimental data. It was also found that the parameter m is related to the activation energy for the rupture of adhesive bonds:

$$m = \frac{U_0}{3kT_g}. \quad (3)$$

Substituting expression (3) into Eq. (2), we obtain

$$\tau = \tau_0 \left(\frac{\sigma_*}{\sigma}\right)^{\frac{U_0}{3kT_g}} \exp\frac{U_0}{kT}. \quad (4)$$

The aim of this study was to check for the validity of Eq. (4) in the case of unoriented polymers and annealed (non-strain-hardened) metals.

1063-7850/05/3111-0969$26.00

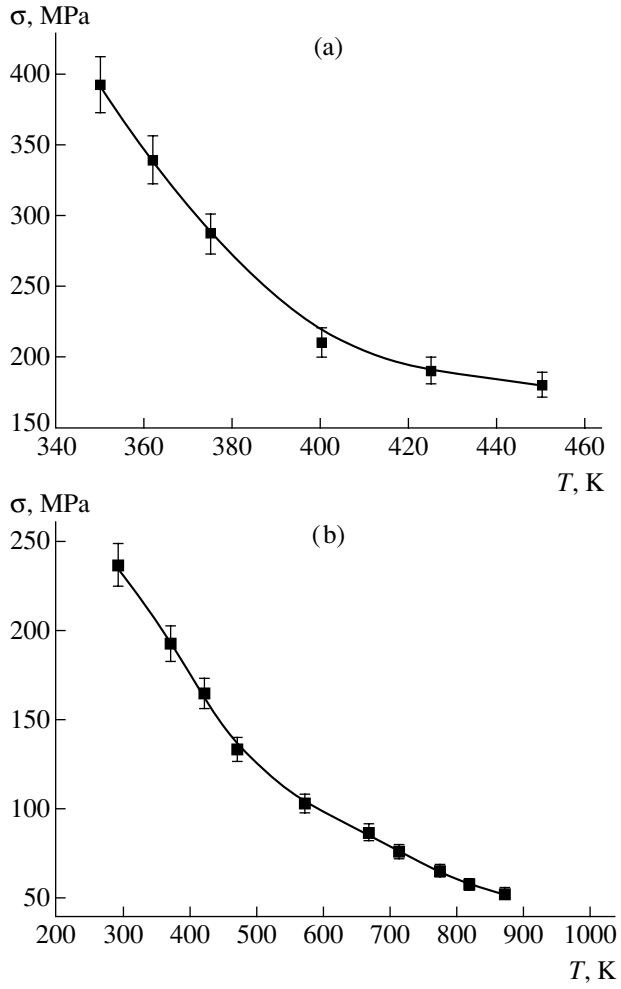

Fig. 1. The temperature dependences of the tensile strength of (a) PETP and (b) Al samples for a constant extension rate (corresponding to $t_f \approx 10$ s).

Experimental. We have studied the temperature dependence of the tensile strength of unoriented polymer films and annealed metal foils. The polymers were polyethylene (PE), polyamide 6 (PA6), polyamide 6.6 (PA66), polyamide 6.6/6 (PA66/6), poly(ethylene terephthalate) (PETP), poly(oxymethylene) (POM), and poly(vinylidene fluoride) (PVF_2); the metals were copper (Cu) and aluminum (Al).

The samples cut from polymer films and metal foils were 30 mm long, 1.5–2 mm wide, and 20–100 μm thick. The tensile tests were performed on UMIV-3 (ZIP, Ivanovo) and 1958 U-10-1 (NIKIMP, Moscow) testing machines at a fixed temperature and a constant strain rate in the interval from 0.005 to 500 mm/min. At each temperature, 5–10 samples were loaded until breakage and the results were averaged. The spread of σ values for samples tested at the same temperature did not exceed 5%.

Results. Figure 1 presents the temperature dependences of the tensile strength of PETP and Al samples for a constant extension rate. The curves obtained for the other polymers and copper had similar shapes. As can be seen from Fig. 1, the curves can be divided into two parts. In the first part, which corresponds to temperatures below T_g for polymers and $0.5T_m$ for metals, the tensile strength exhibits a linear decrease with increasing temperature. At elevated temperatures, the slope of the temperature dependence of the strength gradually decreases with increasing temperature. The values of T_g (for polymers) and T_m (for metals) reported in the literature [13, 14] are presented in the table.

Discussion. The temperature dependence of the tensile strength at $T < T_g$ for polymers and $T < 0.5T_m$ for metals at a constant extension rate can be described using Eq. (1) and the Baily criterion of damage addition [4–6]:

$$\int_0^{t_f} \frac{dt}{\tau[\sigma(t), T]} = 1, \qquad (5)$$

where t_f is the time to fracture. Upon integration [7, 8], we obtain the following approximate expression:

$$\sigma_f(T) \approx \frac{U_0}{\gamma} - \frac{kT}{\gamma} \ln \frac{\tau_{ef}}{\tau_0}, \qquad (6)$$

where $\tau_{ef} \approx 0.1t_f$ and σ_f is the fracture stress. According to relation (6), the tensile strength at a constant loading rate is an approximately linear function of the temperature. This result agrees with the experimental data for unoriented polymers at $T < T_g$ and annealed metals at $T < 0.5T_m$. At elevated temperatures, the tensile strengths of polymers and metals deviate from those predicted by the linear relationship (Fig. 1).

The defect structure of samples and the parameter γ (dependent on this structure) are known to change as a result of deformation. Below T_g (for polymers) and $0.5T_m$ (for metals), the strain at fracture did not exceed 10–20% and, hence, a change in γ in the course of ten-

A comparison of the glass transition temperatures T_g for polymers and the melting temperatures T_m for metals estimated using formula (7) with the published data for T_g [13] and T_m [14]

Material	T_g or T_m, K	
	reported [13, 14]	according to Eq. (7)
PA66	340	320
PETP	370	390
PE	250	250
POM	480	470
PVF_2	300	290
PA66/6	310	330
Al	933	1080
Cu	1356	1160

sile testing could be ignored. At elevated temperatures (above T_g and $0.5T_m$), the situation changes and the prefracture strain significantly increases (reaching especially large values—up to several hundred and thousand percent—in polymers). According to the published data [4, 5, 7], we may suggest that deviations from the Zhurkov equation are related to this significant increase in the prefracture strain. In order to verify this assumption, we have studied the samples of polymers upon preliminary orientational drawing at a temperature close to the melting point (methods of preparing highly oriented polymer samples were described in [11]). After this drawing, the prefracture strain of samples did not exceed 10–15%. It was found that the temperature dependences of the tensile strength for such polymer samples were linear (the Zhurkov equation was valid). This is illustrated in Fig. 2, which shows the temperature dependences of the tensile strength of some highly oriented polymers.

The empirical equation (4) can be rewritten as follows:

$$\ln\sigma \approx \ln\sigma_* - \frac{3kT_g}{U_0}\ln\frac{\tau_{ef}}{\tau_0} + 3\frac{T_g}{T} = A + 3\frac{T_g}{T}. \quad (7)$$

From this expression, it is seen that the logarithm of strength for a fixed loading rate must exhibit linear growth with the inverse temperature, with a slope $(3T_g)$ independent of the time to fracture. Figure 3 shows plots of the logarithm of strength versus inverse temperature at $T > T_g$ for the samples of unoriented PETP. As can be seen, the experimental points corresponding to various times to fracture fit to virtually parallel straight lines. The experimental plots of $\ln\sigma = f(1/T)$ for the other polymers, copper, and aluminum also fit to the straight lines. By measuring the slopes of these plots, we estimated the values of T_g for the polymers studied and T_m for copper and aluminum. As can be seen from the table, these estimates are close to the published values [13, 14].

Equation (4) can be also rewritten as

$$\tau = \tau_0 \exp\frac{U_0 - \frac{U_0 T}{3T_g}\ln\left(\frac{\sigma}{\sigma_*}\right)}{kT} \quad (8)$$

from which it is seen that the parameter γ can be expressed as

$$\gamma = -\frac{\partial U}{\partial\sigma} = \frac{U_0 T}{3T_g\sigma}. \quad (9)$$

It was reported [12] that the tensile strength of polymers at low temperatures (≈73 K) was related to the preliminary deformation ε of samples by the expression

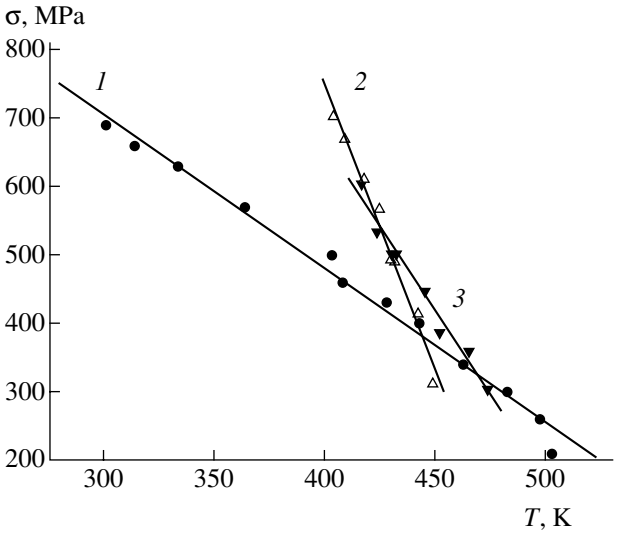

Fig. 2. The temperature dependences of the tensile strength of some highly oriented polymers for a constant extension rate (corresponding to $t_f \approx 10$ s): (*1*) PAN; (*2*) PA6; (*3*) PETP.

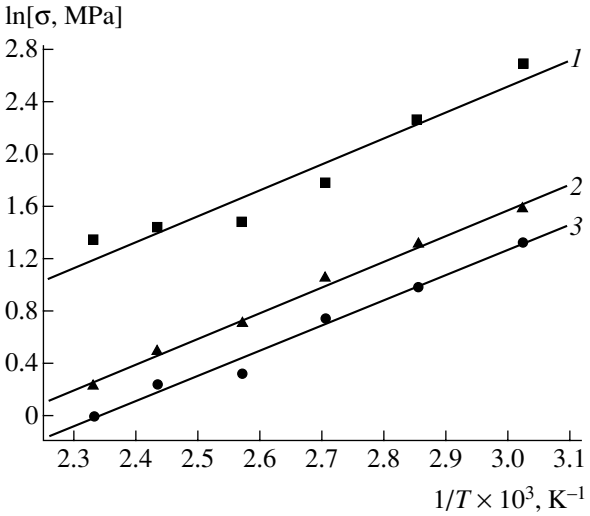

Fig. 3. Plots of $\ln\sigma = f(1/T)$ at $T > T_g$ for the samples of unoriented PETP at various constant loading rates corresponding to $t_f = 10$ (*1*), 10^2 (*2*), and 10^3 s (*3*).

$\sigma \approx \sigma(0)(1 + \varepsilon)$, where $\sigma(0)$ is the strength of the undeformed sample. Substituting this expression into formula (9), we obtain

$$\gamma \approx \frac{U_0 T}{3kT_g\sigma(0)(1+\varepsilon)}.$$

This relation shows that the value of γ at temperatures above T_g (for polymers) and $0.5T_m$ (for metals) is inversely proportional to the degree of elongation at break $1 + \varepsilon$ and directly proportional to the temperature.

For practical applications, it was also of interest to obtain a relation between the parameters σ_* and γ. Equating expressions (1) and (8) at $T = T_g$, we obtain

$$\sigma_* = \sigma_g \exp\left(-\frac{3\gamma\sigma_g}{U_0}\right), \quad (10)$$

where σ_g is the tensile strength at T_g for polymers and at $0.5T_m$ for metals. Thus, we obtained a relation between σ_* in Eq. (2) and the physically clear parameter γ in the Zhurkov equation.

In conclusion, the temperature dependence of the tensile strength for polymers at $T > T_g$ and for metals at $T > 0.5T_m$ is satisfactorily described by the empirical equation (6).

REFERENCES

1. S. N. Zhurkov, Vestn. Akad. Nauk SSSR **11**, 78 (1957).
2. S. N. Zhurkov, Int. J. Fract. Mech. **1**, 311 (1965).
3. S. N. Zhurkov, Vestn. Akad. Nauk SSSR **3**, 46 (1968).
4. V. R. Regel', A. I. Slutsker, and É. E. Tomashevskiĭ, Usp. Fiz. Nauk **106**, 193 (1972) [Sov. Phys. Usp. **15**, 45 (1972)].
5. V. R. Regel', A. L. Slutsker, and É. E. Tomashevskiĭ, *The Kinetic Nature of the Solid Strength* (Nauka, Moscow, 1974) [in Russian].
6. V. A. Petrov, A. Ya. Bashkarev, and V. I. Vettegren, *Physical Basis for the Prediction of the Destruction of Constructional Materials* (Politekhnika, St. Petersburg, 1993) [in Russian].
7. V. A. Stepanov, N. N. Peschanskaya, and V. V. Shpeizman, *Strength and Relaxation Phenomena in Solids* (Nauka, Leningrad, 1984) [in Russian].
8. M. F. Ashbi, C. Gandhi, and D. M. R. Taplin, Acta Metall. **27**, 729 (1979).
9. G. M. Bartenev, *Strength and Mechanisms of the Polymer Fracture* (Khimiya, Moscow, 1984) [in Russian].
10. V. I. Vettegren, A. Ya. Bashkarev, and V. A. Sytov, Pis'ma Zh. Tekh. Fiz. **30** (3), 31 (2004) [Tech. Phys. Lett. **30**, 99 (2004)].
11. A. V. Savitskiĭ and B. Ya. Levin, Vysokomol. Soedin., Ser. B **11**, 409 (1969).
12. A. V. Savitskiĭ and M. P. Nosov, Khim. Volokna **4**, 13 (1978).
13. *Proceedings of the American Chemical Symposium on Transitions and Relaxations in Polymers, Atlantic City, 1965* (Willey, New York, 1966); J. Polym. Sci. C **14** (1965).
14. S. N. Zhurkov and V. A. Kalinin, *Equations of State for Solids at High Temperatures and Pressures* (Nauka, Moscow, 1968) [in Russian].

Translated by P. Pozdeev

Technical Physics Letters, Vol. 31, No. 11, 2005, pp. 973–975. Translated from Pis'ma v Zhurnal Tekhnicheskoĭ Fiziki, Vol. 31, No. 22, 2005, pp. 56–61.

Optical Diagnostics of Dynamic Structures in Shock Waves

P. P. Belousov, P. Ya. Belousov, and Yu. N. Dubnishchev*

Institute of Thermal Physics, Siberian Division, Russian Academy of Sciences, Novosibirsk, Russia

** e-mail: dubnistchev@itp.nsc.ru*

Received May 27, 2005

Abstract—We demonstrate the possibility of applying optical diagnostics based on laser Doppler anemometry techniques and the laser imaging of dynamic density fields to the investigation of kinematic and structural parameters of shock waves and the properties of air perturbed by shock waves. Using the proposed methods, dynamic structures in the shock wave have been revealed and the velocity of their motion over the wave front has been determined. It is suggested that these dynamic structures have an oscillatory nature. *© 2005 Pleiades Publishing, Inc.*

Investigations into shock waves and related perturbations in gaseous media are among the most difficult tasks of experimental gasdynamics [1]. This Letter reports on the observation of dynamic structures formed at the shock wave front in air.

The experiments were performed in a small-size shock tube based on an air gun of the Izh-53 type with a barrel of d = 4.5 mm calibre and 200 mm length. The shock wave was generated upon the breakage of a diaphragm made of one or two layers of a 0.05-mm-thick aluminum foil. The use of an air gun as a portable shock tube provides for the simplicity and high efficiency of experiments.

The shock wave diagnostic setup was based on a Pulsar-3M laser Doppler anemometer (LDA) [2] intended for the measurement of 2D flow velocities in gaseous and condensed media in a range of up to 10^3 m/s. A special feature of this instrument is the high upper boundary of the dynamic range of velocities, which makes possible the investigation of high-rate nonstationary processes in the frequency range up to 250 MHz. The experimental setup consisted of a mechano-optical unit and a computer-controlled high-speed data acquisition and processing system. The radiation source was a 15-mW He–Ne laser, but the setup can operate (without significant modification) using other laser radiation sources, including semiconductor laser diodes emitting in the visible and near-IR spectral ranges.

Figure 1 shows a simplified diagram of the experimental arrangement, with a barrel axis oriented at an angle of 45° relative to the *xy* plane of a 2D base coordinate system set by the probing laser field in the LDA frame. Each realization of the process was used to measure one of the two orthogonal components of the velocity vector. Optical channels forming the 2D base coordinate system were switched by acousto-optical modulators of the running wave, which operated according to a preset program or under the action of an external control signal. The ultrasonic wave frequency in the modulators was 80 MHz. The dynamic structure of a probing laser field formed in the LDA (Pulsar-3M) was such that the array vector coinciding with the direction of motion of the interference fringes was oriented in the opposite direction relative to the measured components v_x and v_y of the shock wave velocity vector. For this reason, the Doppler shift equal to the carrier frequency f_0 = 80 MHz in the light scattered from the dynamic structure corresponded to a zero velocity. The probing field was localized within a volume bounded by an ellipsoid with a semiminor axis of 25 μm and a semimajor axis of 0.35 mm.

The Doppler signal is formed when the shock wave front travels through the probing field. This signal has the form of a short video pulse with the envelope modulated at a frequency determined by a periodic structure of the probing field and the corresponding component of the shock wave front velocity. Kinematic perturbations in the shock wave structure must be manifested in

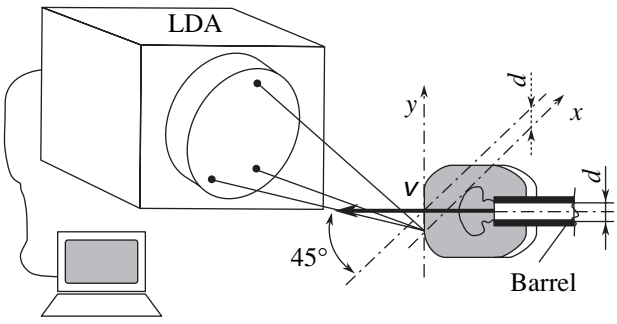

Fig. 1. Schematic diagram of the experimental arrangement (see the text for explanations).

1063-7850/05/3111-0973$26.00 © 2005 Pleiades Publishing, Inc.

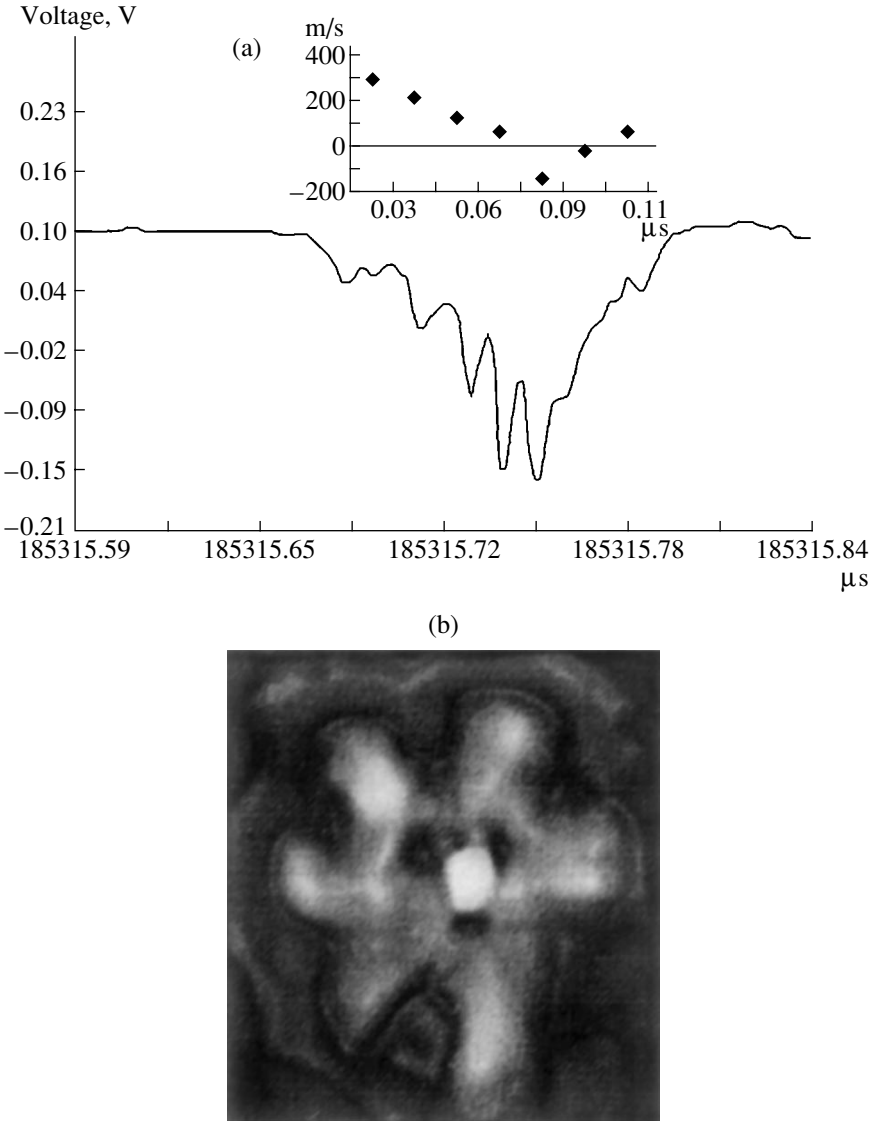

Fig. 2. (a) A fragment of the time series of a Doppler signal obtained for the *y* component of velocity in the shock wave front plane. The inset shows the time variation of the local velocity of motion of the dynamic scattering structure formed at the shock wave front. (b) Laser Doppler image of the dynamic structure formed at the shock wave front crossing the laser sheet.

the dynamic velocity. In order to measure this velocity, the base coordinate system set by the probing laser field was oriented so that the *y* axis would be parallel to the wave front velocity.

Figure 2a shows an example of the typical time series of the Doppler signal observed during the measurement of the *y* component of the velocity vector in the plane of the shock wave front. The probing field was localized at a distance of 10*d* from the barrel edge. The existence of the *y* component of the velocity vector in the configuration of Fig. 1 is indicative of the fact that laser radiation is scattered from the optical inhomogeneities moving in the plane of the wave front.

The shape of the Doppler signals corresponding to the *y* component of the velocity vector is indicative of the ordered structure of dynamic perturbations at the shock wave front. The inset in Fig. 2a shows the time variation of the local velocity of motion of the dynamic scattering structure formed at the shock wave front. The time intervals corresponding to the measured signal and the dynamic velocity are mutually consistent. As can be seen from Fig. 2a, the envelope of the Doppler signal is modulated at a variable frequency. The measured velocity is a single-valued function of this frequency. The velocity varies from 300 m/s to zero over a 0.08 μs time interval and then changes the sign. One possible explanation is that a signal of this type can be due to the scattering of a probing field on a tangential rotating dynamic structure.

In order to reveal the structure of the shock wave front, we performed special experiments using a 2D "laser sheet," which was formed by radiation of a

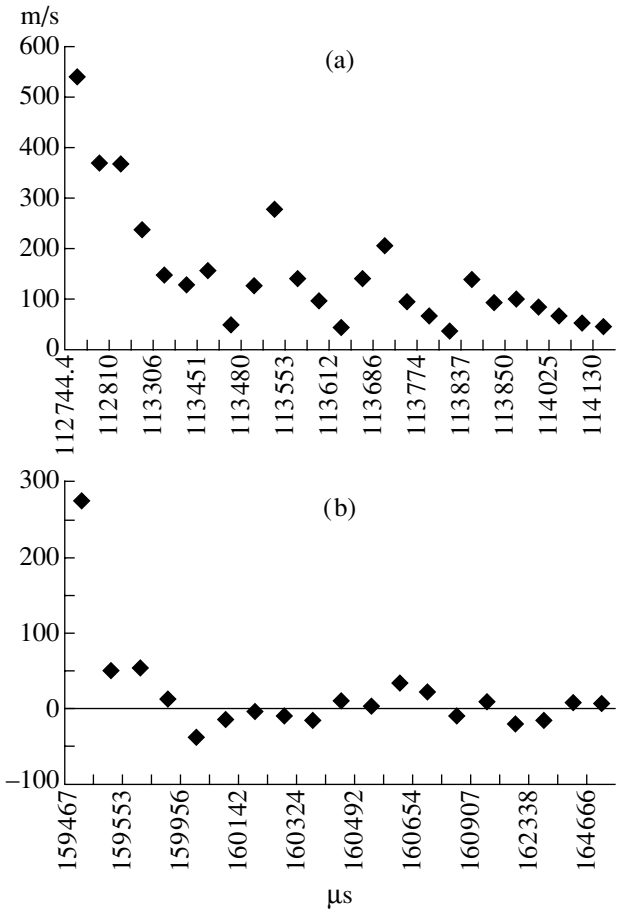

Fig. 3. The typical time variation of the (a) *x* and (b) *y* components of velocity in air perturbed by the shock wave in the geometry depicted in Fig. 1.

200-mW argon laser ($\lambda = 0.515$ μm) at distance of 20*d* from the barrel edge. The shock wave was initiated by the breakage of the diaphragm made of single-layer aluminum foil. The shock wave crossing the laser plane was monitored using a CCD camera. Figure 2b shows an example of the image of a shock wave front crossing the laser sheet, which clearly reveals the radial-tangential mode structure of optical density and is indicative of the possible oscillatory nature of such structures.

The LDA (Pulsar-3M) was used for the investigation of dynamic perturbations produced in air by the propagating shock wave. The particles and optical inhomogeneities crossing the probing field produce random discretization of a nonstationary process, which reflects the dynamic state of the medium in the spatial region within the localized probing field. Computer processing of the signal corresponding to a random sampling provides information on the local velocity field evolution during the shock wave propagation in the medium.

Figure 3 shows the typical time variation of the local velocity in air perturbed by the shock wave. The measurements were performed in the geometry depicted in Fig. 1. The probing field was localized at a distance of 10*d* from the barrel edge. The velocity component was measured along the *x* axis in the shock wave propagation direction (Fig. 3a) and along the *y* axis parallel to the shock wave front plane (Fig. 3b). These data illustrate the evolution of orthogonal components of the local velocity in air perturbed by the shock wave.

Acknowledgments. The authors are grateful to E.E. Meshkov, A.L. Mikhailov, and V.M. Titov for support and fruitful discussions.

This study was supported by the Russian Foundation for Basic Research (project no. 05-02-16896) and the Siberian Division of the Russian Academy of Sciences (integration project no. 28).

REFERENCES

1. L. Hous, T. T. Vtirjd, and G. Jourdan, Shock Waves, No. 9, 249 (1999).
2. Yu. N. Dubnishchev, V. A. Arbuzov, P. P. Belousov, and P. Ya. Belousov, *Optical Methods for Diagnostics of Flows* (Izd. Sib. Univ., Novosibirsk, 2003) [in Russian].

Translated by P. Pozdeev

Technical Physics Letters, Vol. 31, No. 11, 2005, pp. 976–978. Translated from Pis'ma v Zhurnal Tekhnicheskoĭ Fiziki, Vol. 31, No. 22, 2005, pp. 62–67.

Synchronizing Pulsations of a Saturating Absorber Injection Laser

A. S. Lar'kin* and G. V. Belokopytov

Department of Physics, Moscow State University, Moscow, Russia

** e-mail: larand@rambler.ru*

Received June 6, 2005

Abstract—Radiation pulses of an injection laser with a saturating absorber layer have been synchronized using a harmonic microwave (0.8–2.6 GHz) current with a power below 1 mW. The synchronization leads to a sharp decrease in instability of the laser pulse repetition period. The dependence of the synchronization frequency band on the pumping current, the synchronizing signal amplitude, and the temperature has been studied. © *2005 Pleiades Publishing, Inc.*

The phenomenon of synchronization of self-sustained pulsating injection lasers by external microwave oscillations was originally observed about four decades ago [1, 2]. The first experiments were performed with laser diodes possessing a rather imperfect structure, in which the synchronization effect was observed only for large pumping currents and significant microwave powers. The laser generation proceeded in a multimode regime, involved the joint action of several mechanisms of vibrational instability, and was accompanied by modulation of the width of the emitting region. These factors complicated the course of experiments and the interpretation of results. The fact of synchronization was established using the measurements of time series, which required laborious procedures and did not ensure high accuracy [3].

In recent years, periodic sequences of subnanosecond pulses have been obtained using injection lasers with saturating absorber layers [4–6]. A special feature in the structure of such a saturating absorber injection laser (SAIL) is a region of nonlinear optical absorption, which is formed in a layer of semiconductor parallel to the active region by the implantation of heavy metal ions at an energy of 10^6–10^7 eV. Another possible variant is the creation of a saturating absorber layer by doping the surface layers of reflectors of the injection laser.

This Letter reports on the synchronization of SAIL pulsations by a harmonic microwave current. The experiments have been performed using a series of 786-nm lasers with room-temperature threshold currents $I_{th} = 20 \pm 0.4$ mA and specific radiation output powers about 0.8 mW/mA. The laser emission in a self-sustained pulsation regime was observed for pumping currents in the interval from I_{th} up to $I_1 \approx 35$–40 mA. Being pumped in the vicinity of I_{th}, lasers generated periodic sequences of pulses with a width below 200 ps. The pulse repetition (self-pulsation) frequency f_{sp} increased with the pumping current and could be varied within 0.8–2.6 GHz (Fig. 1). Near the boundary I_1 of the continuous generation region, the emission did not completely decay during the interval between pulses and the resulting envelope acquired the shape of amplitude-modulated pulsations with a modulation depth that decreased on approaching I_1. At a pumping current of I_1, the lasers began to operate in a continuous regime.

A special feature of the injection lasers studied was the single-mode emission in the entire interval of pumping currents used in the experiment. No significant variations in the near-field spatial structure of radiation were observed during the laser pulse.

The course of synchronization was monitored using a spectral technique. The laser radiation pulses were

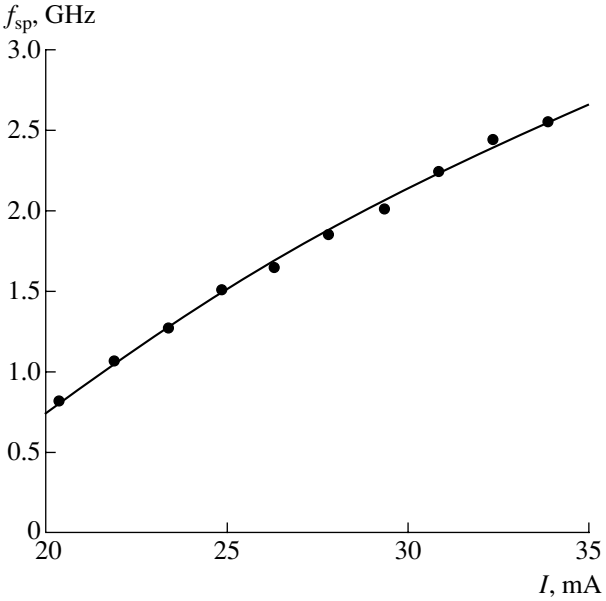

Fig. 1. A plot of the self-pulsation frequency f_{sp} versus pumping current I for a saturating absorber injection laser.

1063-7850/05/3111-0976$26.00 © 2005 Pleiades Publishing, Inc.

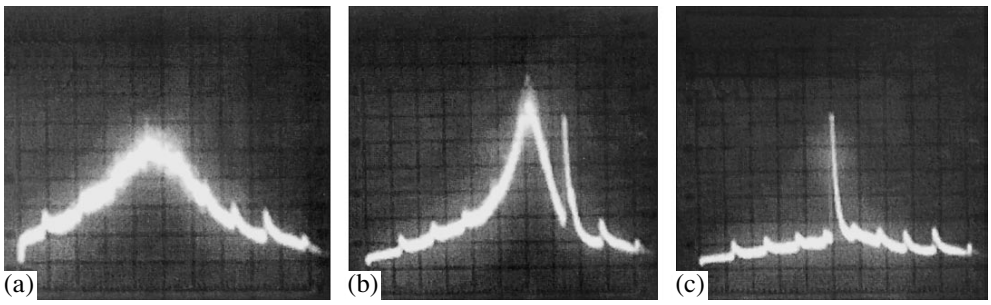

Fig. 2. Spectrograms of the optical pulse envelopes: (a) free self-pulsation regime (f_{sp} = 785 MHz, I = 20.5 mA); (b) asynchronous regime (f_{sp} = 1120 MHz, I = 23 mA, f_s = 1095 MHz, I_s = 2.5 mA); (c) synchronized self-pulsation regime ($f_{sp} = f_s$ = 1120 MHz, I = 23 mA, I_s = 2.5 mA). T = 17.5°C. The spikes in the spectrograms represent 10 MHz marks.

detected by an avalanche photodiode (LFD-2), whose output signal was fed to a microwave spectrum analyzer (S4-27). The spectral line of the first harmonic of the optical pulse envelope exhibited a maximum at the frequency of self-pulsation. At a pumping current slightly above I_{th}, this spectral line was significantly broadened, which is indicative of a high level of fluctuations of the time interval between laser pulses (Fig. 2a). As the pumping current was increased, the line exhibited narrowing (cf. the peak in Fig. 2a to the left peak in Fig. 2b).

The phenomenon of synchronization was studied by applying a harmonic signal from a microwave oscillator together with the dc pumping current to a laser diode. The entire range of synchronization frequencies f_s = 0.8–2.6 GHz was covered using three oscillators (G4-129, G4-78, and G4-79). The action of a harmonic current component led to modulation of the onset of laser pulsations, which was manifested by the appearance of a line with the frequency f_s in the spectrum of the optical pulse envelope. If f_s was significantly different from the self-pulsation frequency f_{sp}, then two spectral lines were separately displayed by the spectrum analyzer (Fig. 2b). When f_s was tuned so as to approach the self-pulsation frequency, the f_{sp} line also exhibited a shift towards f_s. Depending on the pumping current and the synchronizing signal amplitude, this shift amounted to from several units to several tens of megahertz.

With the subsequent tuning, the f_{sp} and f_s lines merged together, which was accompanied by a sharp narrowing of the resulting spectral line (Fig. 2c). This moment represented a boundary of the synchronization band. Attempts to further change the external signal frequency f_s led to the breakage of synchronism and the appearance of two separate lines in the spectrum.

Figure 3 illustrates the dependence of the synchronization band on the microwave current amplitude I_s and the pumping current I. As the pumping current I is increased above the threshold I_{th}, the synchronization band initially exhibits narrowing (Fig. 3a), but then, for I approaching I_1, the band becomes broad again (Fig. 3b). The nonmonotonic dependence of the synchronization bandwidth on the pumping current indicates that the mechanisms of synchronization of the laser radiation pulses near the lasing threshold and near the boundary of the region of stable self-sustained pulsations are different. Some qualitative considerations in favor of this hypothesis can be formulated using a SAIL model based on the rate equations [7]. According to this model, the addition of a harmonic signal to the pumping current near the threshold changes the time to reaching a threshold density of carriers in the active region and thus controls the repetition period of light pulses. This mechanism is analogous to the traditional scenario of synchronization of a sawtooth oscillator [8]. The situation near a boundary of the transition to a regime of continuous generation is different. At a pumping current exceeding I_1, the microwave component produces forced modulation at the f_s frequency rather than synchronization. At a somewhat lower pumping current ($I < I_1$), the microwave oscillations at a frequency of f_s also produce forced modulation of the

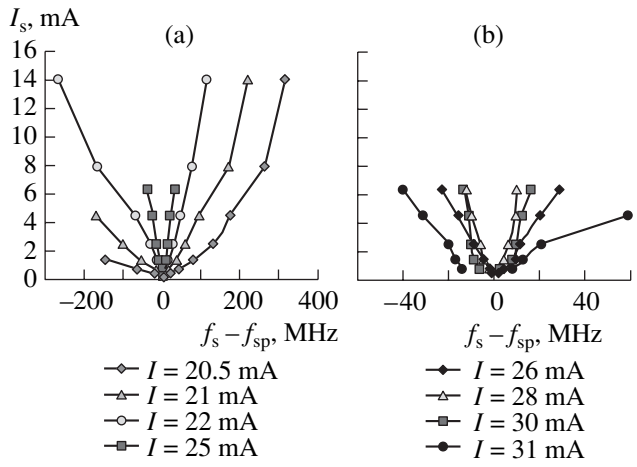

Fig. 3. Effect of the synchronizing signal amplitude I_s on the synchronization bands for SAILs in self-pulsation regimes (a) near the generation threshold and (b) near the boundary of the region of continuous generation.

light intensity and, in addition, suppress the self-pulsation at f_{sp} as a result of the asynchronous quenching [8].

The phenomenon of SAIL synchronization was observed in a temperature interval from 8.5 to 45°C. As the temperature was increased, the frequency of self-pulsation at a fixed pumping current decreased at a rate of 25 MHz/K. This was accompanied by narrowing of the synchronization band at a constant microwave signal amplitude. For example, the synchronization bandwidth for $I_s = 4.5$ mA and $f_{sp} = 1.0$ GHz decreased from 250 MHz at 8.5°C to 70 MHz at 45°C.

The SAIL radiation pulses were also synchronized under the microwave action at a second harmonic frequency, provided that $f_s \approx 2f_{sp}$. In this regime, the synchronization band was much narrower and varied, depending on the conditions, from 16 to 30 MHz (for $I_s = 2$–6 mA).

The effect of synchronization was reached at a synchronizing signal power of 10^{-5}–10^{-3} W, which is three to five orders of magnitude lower than the power used in the early experiments [3]. This result opens the way to using the phenomenon of SAIL synchronization in a number of practical applications. First, the microwave synchronization provides for an increase in the stability of SAIL pulsation frequency. This synchronization decreases the influence of both the working temperature and pumping current variations, as well as of the gain fluctuations in the active region. Second, by changing the microwave signal frequency, it is possible to control the period of SAIL pulsations in a broad range (up to 40% and even more, see Fig. 3a). Third, one master microwave oscillator can be used for the synchronization of several SAILs, and then the appropriate delay elements can readily provide desired time shifts between the stable pulse sequences of different lasers.

Acknowledgments. The authors are grateful to A.S. Logginov and B.Yu. Terletskiĭ for fruitful discussions and to G.T. Pak for kindly providing the samples of injection lasers with saturating absorber layers.

REFERENCES

1. V. N. Magalyas, A. A. Pleshkov, L. A. Rivlin, *et al.*, Pis'ma Zh. Éksp. Teor. Fiz. **6**, 550 (1967) [JETP Lett. **6**, 68 (1967)].
2. Yu. P. Zakharov, I. N. Kompanets, V. V. Nikitin, *et al.*, Zh. Éksp. Teor. Fiz. **53**, 1553 (1967) [Sov. Phys. JETP **26**, 895 (1967)].
3. K. Ya. Senatorov, A. S. Logginov, L. P. Ivanov, *et al.*, Kvantovaya Élektron. (Moscow), No. 1, 160 (1974).
4. I. Kidoguchi, H. Adachi, S. Kamiyama, *et al.*, IEEE J. Quantum Electron. **33**, 831 (1997).
5. H. D. Summers, S. H. Molloy, P. M. Smowton, *et al.*, IEEE J. Sel. Top. Quantum Electron. **5**, 745 (1999).
6. G. B. Venus, I. M. Gadzhiev, A. M. Gubenko, *et al.*, Pis'ma Zh. Tekh. Fiz. **25** (13), 4 (1999) [Tech. Phys. Lett. **25**, 506 (1999)].
7. T. W. Carr and T. Erneux, IEEE J. Quantum Electron. **37**, 1171 (2001).
8. *Fundamentals of the Oscillation Theory*, Ed. by V. V. Migulin (Nauka, Moscow, 1988), pp. 214–223 [in Russian].

Translated by P. Pozdeev

Technical Physics Letters, Vol. 31, No. 11, 2005, pp. 979–981. Translated from Pis'ma v Zhurnal Tekhnicheskoĭ Fiziki, Vol. 31, No. 22, 2005, pp. 68–73.

Features of the Coercivity of Strained Epitaxial Garnet Ferrite Films

S. V. Dubinko*, A. S. Nedviga, V. G. Vishnevskiĭ, A. N. Shaposhnikov, V. S. Yagupov, A. G. Nesteruk, and A. R. Prokopov

Taurida National University, Simferopol, Ukraine

** e-mail: domain@crimea.edu*

Received June 17, 2005

Abstract—We have studied the influence of the relative film–substrate lattice mismatch in the 0.5–0.85% range on the behavior of coercivity in epitaxial garnet ferrite (EGF) films with compositions $(Bi, Sm, Lu, Ca)_3(Fe, Sc, Ga, Al)_5O_{12}$ grown on (111)-oriented gadolinium gallium garnet (GGG) substrates. As the relative film–substrate lattice mismatch increases, the coercivity of EGF films initially grows, passes through a maximum, and then decreases. The maximum in the coercivity is related to periodic localized stresses caused by the formation of a misfit dislocation network whose period is comparable with the width of domain walls. The period of localized stresses is determined by the relative lattice mismatch between the EGF film and the GGG substrate.

Epitaxial garnet ferrite (EGF) films are widely used in thermomagnetic data recording devices [1] and in systems used for the topography and imaging of inhomogeneous magnetic fields. In these applications, a special position is occupied by the EGF films with increased coercivity, which make possible the imaging of even weak inhomogeneous magnetic fields, with strengths on the order of 0.1 Oe and spatial periods below 1 μm, using replication techniques [2]. Previously, it was established [3–5] that the coercive force H_c of EGF films depends on a relative lattice mismatch f between the epitaxial film and a substrate. In particular, it was found that H_c significantly increases with f growing from 0.2 to 0.5%, and it was suggested that the coercivity would further increase with f exceeding 0.5%. However, no experimental data for the influence of the relative lattice mismatch above 0.5% on the coercivity of EGFs have been reported so far. Jatau *et al.* [6] explained the increase in the coercivity of GGG films by the presence of iridium inclusions, which induce stresses and produce local changes in the EGF anisotropy at various distances from the substrate surface, while the possible influence of the film–substrate lattice mismatch was ignored.

In this context, we have studied the influence of the relative lattice mismatch above 0.5% between epitaxial films and substrates on the coercivity of the EGF films.

The investigation was performed for EGF films with compositions $(Bi, Sm, Lu, Ca)_3(Fe, Sc, Ga, Al)_{0.5}O_{12}$ grown on (111)-oriented gadolinium gallium garnet (GGG) substrates by the method of isothermal liquid phase epitaxy from Bi_2O_3–PbO–B_2O_3 solution melts. The f values were varied by changing the growth temperature and the molar ratio of components in the initial mixture.

The coercivity H_c was determined from magnetooptical hysteresis loops, which were recorded using a magnetooptical polarimeter. The relative lattice mismatch f was estimated using a standard technique based on X-ray diffraction measurements, which were performed on a DRON-3 diffractometer. The effective uniaxial anisotropy fields, saturation fields, and equilibrium periods of the domain structure of EGF films were determined using magnetooptical techniques. In all the EGF films studied, the effective uniaxial anisotropy field was about 10^3 Oe, the saturation fields varied within 149–290 Oe, the coercivity fields H_c varied from 25 to 70 Oe, the equilibrium periods of the domain structure upon exposure to an ac magnetic field fell within 4.6–8.0 μm, and the Néel temperatures were T_N = 55–97°C. The EGF film thicknesses upon surface polishing were 3–4 μm. We have studied EGF films grown with the relative lattice–substrate mismatch f varying from 0.55 to 0.85%. The films with f values in this interval were continuous and exhibited a sufficiently high specific Faraday's rotation for the imaging of inhomogeneous magnetic fields. Further increase in the relative lattice mismatch led to violation of the continuity of EGF films, sharp deterioration of their optical properties, and even delamination of the epilayers from the substrate surface.

The results of our experimental investigation of the coercivity of EGF films as a function of f showed that H_c reached a maximum at a relative film–substrate lattice mismatch of about 0.7% (Fig. 1). We may suggest that the initial growth, followed by the passage through a maximum and a subsequent decrease in the coerciv-

1063-7850/05/3111-0979$26.00 © 2005 Pleiades Publishing, Inc.

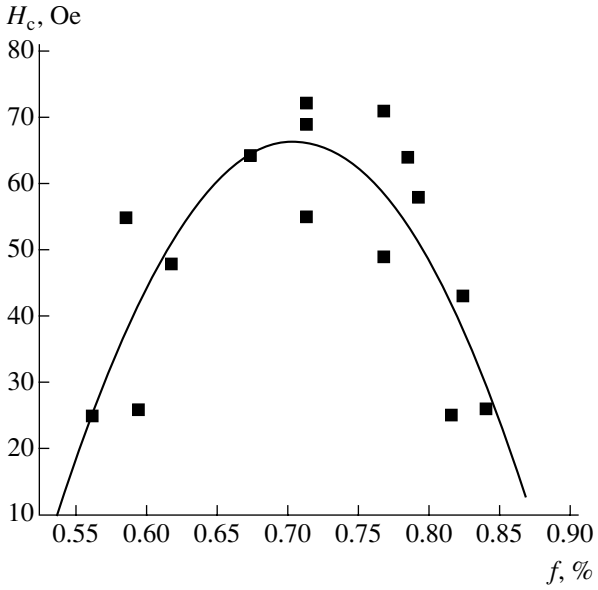

Fig. 1. The experimental plot of coercivity H_c versus relative film–substrate lattice mismatch f for EGF films on GGG substrates.

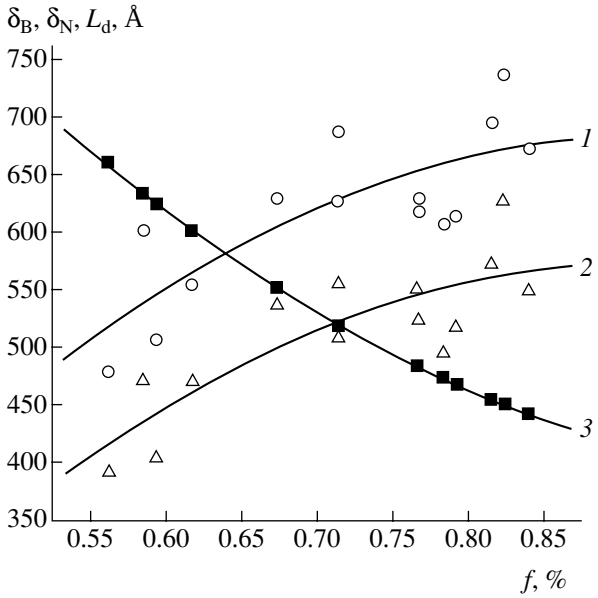

Fig. 2. Plots of the (*1*) δ_B, (*2*) δ_N, and (*3*) L_d versus f for EGF films on GGG substrates.

ity, is related to the formation of a network of misfit dislocations in the EGF film. This misfit dislocation network creates periodic localized stresses and a related potential relief with a certain period l, which hinders the motion of domain walls and leads to a change in the H_c value [7].

Previously, the behavior of coercivity was explained in terms of the stress theory [8–10], and it has been concluded that H_c acquires the maximum value for a given magnetic material when the period of local stresses is approximately equal to the domain wall width. Therefore, it is logical to assume that the period l is equal to the interdislocation distance L_d.

We have plotted the width δ of the domain walls (of the Bloch and Néel types) and L_d versus lattice mismatch f. The δ values were calculated using the formulas [11] $\delta_B = \pi(A/K_u)^{1/2}$ for the Bloch walls and $\delta_N = \pi[A/(K_u + 2\pi M_s^2)]^{1/2}$ for the Néel walls, where A is the exchange constant, K_u is the uniaxial anisotropy constant, and M_s is the saturation magnetization. The exchange constant was calculated as [12] $A = A_0(T_N - T)/(T_{N0} - T)$, where $A_0 = 3.7$ pJ/m is the exchange constant for yttrium iron garnet (YIG), $T_{N0} = 560$ K is the Néel temperature of YIG, and $T = 300$ K. The values of K_u were calculated using the measured effective fields of uniaxial anisotropy of the EGF films, and their M_s values were determined using data on the saturation fields, equilibrium periods of the domain structure, and film thicknesses [12]. The interdislocation distances were calculated using the formula $L_d = kb/f$ [13, 14], where $b = 2a_f a_s/(a_f + a_s)$ is the Burgers vector of dislocations, a_f is the lattice period of the EGF film, $a_s = 12.383$ Å is the substrate lattice period [15], and $f = [(a_f - a_s)/a_f] \times 100\%$. In the (111)-oriented EGF films under consideration, $k = 1$ for the edge dislocations and $k = 0.3$ for 60° dislocations [13].

As is known, the misfit dislocation network can be formed by the edge dislocations and 60° dislocations. Figure 2 shows the plots of $\delta_B(f)$, $\delta_N(f)$, and $L_d(f)$, where L_d is determined for 60° dislocations. As can be seen, the $\delta_N(f)$ and $L_d(f)$ curves intersect at the f value corresponding to the H_c maximum in the $H_c(f)$ curve (Fig. 1). In the interval of f values studied, the $\delta_B(f)$ and $\delta_N(f)$ curves do not intersect with $L_d(f)$ for the edge dislocations.

The equality of δ_N and L_d (for 60° dislocations) observed for the EGF films with the maximum H_c value is in agreement with conclusions of the stress theory. Thus, we may suggest that EGF films with maximum H_c contain domain walls of the Néel or mixed types and that the dislocation networks are formed predominantly by 60° dislocations.

In conclusion, we have established that an increase in the relative film–substrate lattice mismatch leads to an increase followed by decrease in the EGF film coercivity. It was demonstrated that the maximum coercivity is characteristic of EGF films with the domain wall width equal to the period of localized stresses caused by the formation of a misfit dislocation network. The period of localized stresses is determined by the relative lattice mismatch between the film and the substrate. Using the obtained results, it is possible to predict the coercivity of EGF films in a broad range of the lattice mismatch between the film and the substrate and to obtain films with a desired coercivity.

Acknowledgments. This study was supported by the Ministry of Education and Science of Ukraine within the framework of the National Budget Article "Applied Works in Research and Development Activity of High School."

REFERENCES

1. D. Inoue, A. Itoh, and K. Kawanishi, Jpn. J. Appl. Phys. **19**, 2105 (1980).
2. R. M. Mikherskii, S. V. Dubinko, V. G. Vishnevskii, *et al.*, Functional Materials **9**, 115 (2002).
3. A. M. Balbashov, A. Ya. Chervonenkis, M. L. Shupegin, *et al.*, Mikroélektronika **11**, 126 (1982).
4. D. M. Gualtieri and P. F. Tumelti, J. Appl. Phys. **57**, 3879 (1985).
5. L. A. Dovbnya, D. E. Naumov, and B. V. Khramov, Pis'ma Zh. Éksp. Teor. Fiz. **73**, 410 (2001) [JETP Lett. **73**, 366 (2001)].
6. J. A. Jatau, M. Pardavi-Horvath, and E. Della Torre, J. Appl. Phys. **75**, 6106 (1994).
7. V. V. Randoshkin and A. Ya. Chervonenkis, *Applied Magnetooptics* (Énergoizdat, Moscow, 1990) [in Russian].
8. R. M. Bozorth, *Ferromagnetism* (Van Nostrand, New York, 1951; Inostrannaya Literatura, Moscow, 1956).
9. S. V. Vonsovskii, *Magnetism* (Nauka, Moscow, 1971; Wiley, New York, 1974).
10. V. I. Ivanovskiĭ and L. A. Chernikova, *Physics of Magnetic Phenomena: Seminars* (Moscow, 1981) [in Russian].
11. V. F. Lisovskiĭ, *Physics of Circular Magnetic Domains* (Sov. Radio, Moscow, 1979) [in Russian].
12. A. M. Balbashov, F. V. Lisovskiĭ, V. K. Raev, *et al.*, in *Elements and Devices Based on the Bubble Magnetic Materials: A Handbook*, Ed. by N. N. Evtikhiev and B. N. Naumov (Radio i Svyaz', Moscow, 1987) [in Russian].
13. J. H. Van der Merve, in *Single Crystal Films* (Mir, Moscow, 1966), pp. 172–201 [in Russian].
14. M. G. Mil'vidskii, *Semiconductor Materials in Modern Electronics* (Nauka, Moscow, 1986) [in Russian].
15. L. S. Palatnik and V. K. Sorokin, *Materials Science in Microelectronics* (Moscow, 1978) [in Russian].

Translated by P. Pozdeev

Technical Physics Letters, Vol. 31, No. 11, 2005, pp. 982–985. Translated from Pis'ma v Zhurnal Tekhnicheskoĭ Fiziki, Vol. 31, No. 22, 2005, pp. 74–81.

Experimental Investigation of Electron Beam in the Squeezed State

S. Ya. Belomyttsev[a], A. A. Grishkov[b], S. A. Kitsanov[a], S. D. Korovin[a,*], S. D. Polevin[a], V. V. Ryzhov[b], and A. P. Yachnyĭ[b]

[a] *Institute of High-Current Electronics, Siberian Division, Russian Academy of Sciences, Tomsk, 634055 Russia*
[b] *Lebedev Institute of Physics, Russian Academy of Sciences, Moscow, 117924 Russia*
* *e-mail: korovin@hcei.tsc.ru*
Received June 20, 2005

Abstract—The electron beam transported in a two-section drift tube of a SINUS-7 setup has been studied. A high-density electron beam in the "squeezed" state has been obtained with a relativistic factor γ_b below that corresponding to the limiting current ($\gamma_b < \Gamma^{1/3}$). © *2005 Pleiades Publishing, Inc.*

It is well known that an electron beam with a given total current I transported in a cylindrical channel can occur either in the normal "fast" state or in a "slow" (or "squeezed") state. The fast state is characterized by a low density of electrons and a high relativistic factor, $\gamma_b > \Gamma^{1/3}$ (where $\Gamma = 1 + eU/mc^2$, e is the electron charge, m is the electron mass, c is the velocity of light, and U is the diode voltage), whereas the slow state corresponds to a high density of electrons and a relatively low relativistic factor, $\gamma_b < \Gamma^{1/3}$ [1]. Electron beams obtained in experiments usually occur in the fast state.

Ignatov and Tarakanov [2] originally demonstrated by means of numerical simulation that electron beams in the squeezed state can be obtained using a two-section drift channel. When the injected beam current (I_{inj}) exceeds a certain threshold corresponding to the limiting transport current (I_{lim2}) for the channel section with a greater radius, a virtual cathode (VC) is formed at the junction between sections. If the injected current is further increased to exceed a certain critical transition value (I_{Tr}), the VC shifts toward the electron injector and the beam behind the VC plane passes to the squeezed state [3]. However, electron beams in the squeezed state have not been experimentally studied so far.

This Letter reports on the results of an experimental investigation of an electron beam in the squeezed state transported in a two-section drift channel. The experiments were performed on a high-current electron accelerator SINUS-7 [4] operating at a cathode voltage of up to 2 MV, a diode current up to 20 kA, and an injected current pulse duration of 50 ns.

Figure 1 shows a schematic diagram of the experimental arrangement. The electron beam was generated in a coaxial vacuum diode with magnetic isolation and injected via an anode insert into the two-section drift tube. Electrons were emitted from a cylindrical graphite explosive-emission cathode with a radius of $R_C \approx 9.5$ mm and a ridge width of 0.5 mm. As a result, a thin-wall annular electron beam was formed in a homogeneous longitudinal magnetic field of sufficiently high strength (~15 kOe). The anode insert had a channel radius of 20 mm and a length of 130 mm. The fixed lengths of the first and second sections of the drift channel in our setup ($L_{dr1} \approx 150$ mm and $L_{dr2} \approx 400$ mm, respectively) were significantly greater than the corresponding radii ($R_{A1} \approx 24$ mm and $R_{A2} \approx 41$ mm). The current injected into the drift channel could be controlled by changing the distance from the cathode to the anode insert (L_{AC}) at a constant diode voltage $U \approx (800 \pm 30)$ kV. The potential difference between the electron beam and the anode was measured using capacitive voltage dividers arranged in the central part of each section of the drift tube. The beam current was measured using a low-inductance ohmic shunt in the collector circuit.

The vacuum diode current I_D was measured in a series of experiments with a collector arranged at the end of the anode insert. In this geometry, variation of the anode–cathode distance L_{AC} from 70 mm (when the cathode occurs in the anode tube, Fig. 1) to –15 mm (whereby the cathode edge protrudes 15 mm into the anode insert) led to a change of the diode current within $I_{FD} < I_D < I_{FA}$, where $I_{FD} \approx 3$ kA and $I_{FA} \approx 6.8$ kA are the Fedosov currents of coaxial diodes with magnetic isolation and the drift channel radii equal to the radii of the anode tube and anode insert, respectively.

In experiments with the electron beam transported via the two-section drift channel, the collector was arranged at the end of the second section (Fig. 1) and the injected current upon the VC formation was determined with allowance for the magnitude and direction

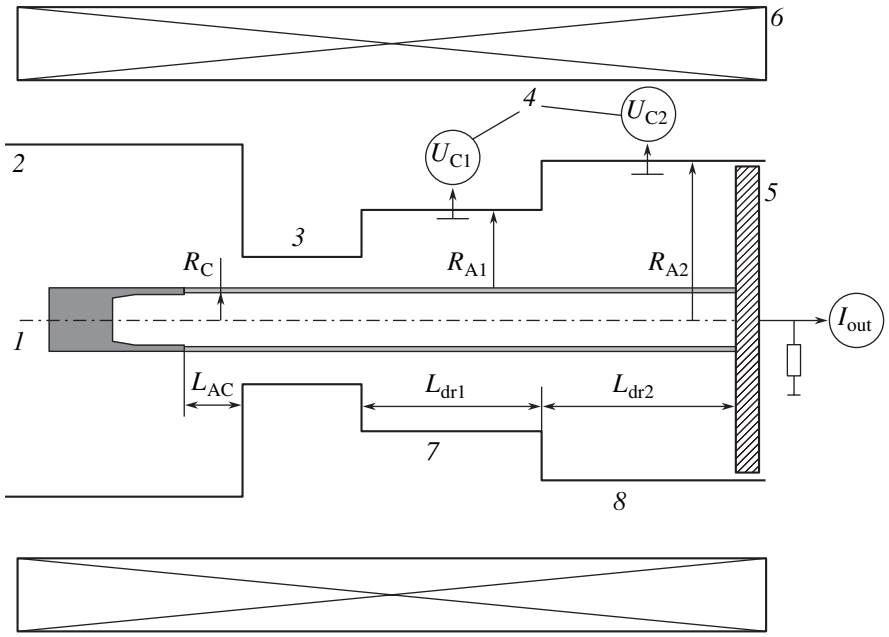

Fig. 1. Schematic diagram of the experimental arrangement: (*1*) cathode; (*2*) anode tube; (*3*) anode insert; (*4*) capacitive voltage dividers; (*5*) collector; (*6*) solenoid; (*7*, *8*) drift channel sections of small and large radius, respectively.

of the current (I_{back}) reflected from the VC: $I_{inj} = (I_D + I_{out})/2$, where $I_D = I_{inj} - I_{back}$ is the experimentally measured value of the diode current in the presence of VC at a given gap width L_{AC} and I_{out} is the collector current.

Figure 2 shows the typical oscillograms of signals measured using the voltage dividers and the low-ohmic shunt in the cases of beam transport without and with VC in the drift channel. At a large gap width L_{AC}, the VC is absent (because $I_D < I_{lim2}$) and the signals have nearly trapezoidal shapes (Fig. 2a). In this case, the collector current I_{out} coincides with the injected current, $I_{out} = I_{inj} = I_D$ (straight segment in the plot of the relative collector current versus injected current in Fig. 3a). When the injected current slightly exceeded the limiting value for the second channel section ($I_{inj} > I_{lim2}$), the oscillogram of U_{C2} exhibited a sharp decrease at a certain moment of time (indicated by the arrow in Fig. 2b). The results of numerical simulation performed using the PIC code KARAT [5] showed that this moment corresponded to the VC formation. For this reason, the experimental data were processed assuming that the collector current I_{out} after this moment corresponded to the beam current behind the VC.

Thus, the results of experiments (Fig. 2b) and numerical simulations (Fig. 3a) showed evidence for a decrease in the transmitted beam current when the injected current exceeded I_{lim2}. This is explained by the fact that, at the moment of VC formation near the junction of the two drift channel sections, the fluxes of the *z*-component of the electric field and particle momenta at this junction exhibit jumplike changes. Numerical estimates of these changes for the case under consideration correspond to $\Delta I \approx 0.1 I_{lim2}$, in agreement with the experimental values. As the injected current is increased further, the transmitted current approaches I_{lim2} (to within the experimental accuracy). In our previous experiments involving the measurement of the beam current behind the VC in a homogeneous drift channel [6], the transmitted current also decreased upon the VC formation, but the precision of the measurements and numerical calculations was insufficient for reliably detecting this effect.

The state of the electron beam in a transport channel can be characterized using the results of potential measurements. As can be seen from Fig. 3a, the value of the electron beam potential U_{C2}/U in the channel section of greater radius and its dependence on the injected current correspond to a beam with the limiting current, that is, to a beam in the fast state.

The experiments and the numerical simulations showed that, as the injection current was increased, the beam potential U_{C1}/U in the channel section of smaller radius initially exhibited a monotonic growth. When the injected current reached a certain level [3], the beam potential ceased to grow and remained virtually constant (Fig. 3b). For the interpretation of experimental data, we have estimated the U_C/U ratio using data on the beam charge in the channel section of smaller radius for two cases (Fig. 3b). In the first case, it is assumed that, when the injected current exceeds I_{lim2}, a VC is formed at the junction of two sections and a reflected current appears, but the beam still occurs in the fast state (Fig. 3b, curve *ABCD*). In the second case, it is

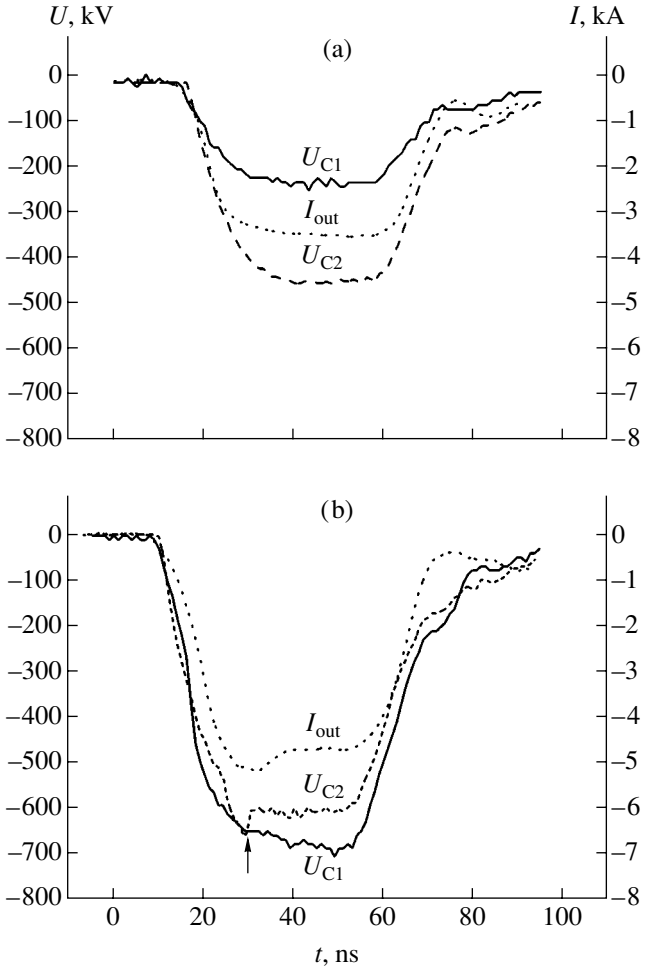

Fig. 2. The typical oscillograms of the beam potential and current in the two-section drift channel (a) without and (b) with VC (arrow indicates the moment of VC formation).

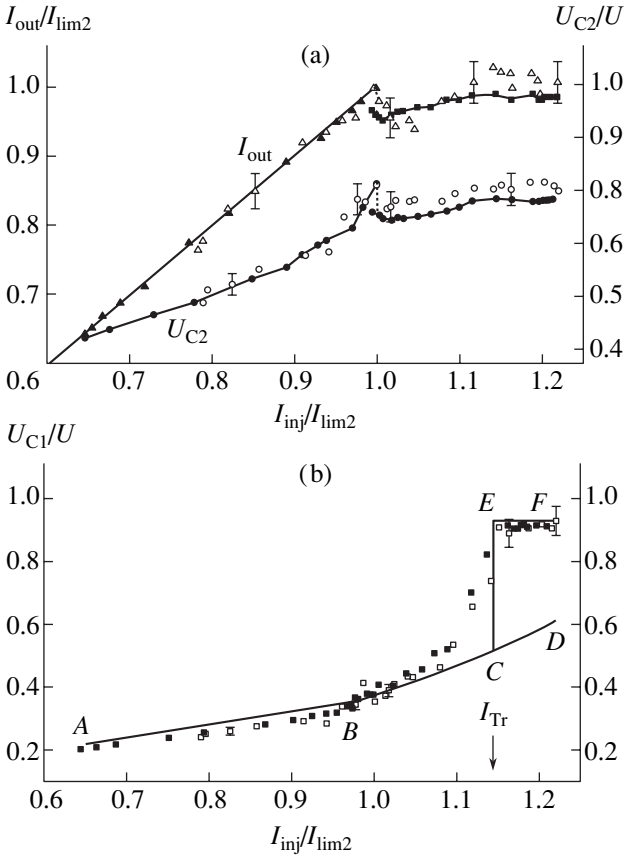

Fig. 3. Plots of the relative beam potential U_C/U and current I_{out}/I_{lim2} versus relative injected current I_{inj}/I_{lim2} for a two-section drift channel. Solid curves in (a) and filled symbols present the results of numerical simulations performed using the PIC code KARAT; open symbols present the experimental data obtained on a SINUS-7 accelerator; curves *ABCD* and *ABCEF* in (b) show the results of approximate calculations of U_{C1}/U using two models (see the text).

assumed that, when the injected current reaches the transition value $I_{inj} = I_{Tr}$ [3], the VC shifts from the junction to the beginning of the first channel section and a squeezed beam is formed behind the VC (Fig. 3b, curve *ABCEF*). As can be seen from Fig. 3b, the results of calculations in the second case well agree with the obtained experimental data. Therefore, in all experiments where the injected current reached or exceeded the transition value, $I_{inj} \geq I_{Tr}$, the electron beam in the channel section of smaller radius occurred in a single-flux squeezed state. In this state, the measured beam potential in the first section remained constant, independently of the injected current (Fig. 3b). The kinetic energy of electrons in the squeezed beam, $mc^2(\gamma_b - 1) \approx$ 70–80 keV, was approximately one order of magnitude lower than their energy on the collector, and the relativistic factor ($\gamma_b = 1.15$) was smaller than that for the beam with $I_{inj} = I_{lim2}$ (for which $\Gamma^{1/3} \approx 1.36$).

The transition current calculated using the law of conservation of the *z*-component of the field and particle momentum, $I_{Tr} = 5.4$ kA [3], well agrees with the minimum injection current at which the beam potential in the first channel section becomes equal to that for a beam in the single-flux squeezed state.

The results of numerical simulations showed that, in the interval of injection currents $I_{lim2} < I_{inj} < I_{Tr}$ (whereby the VC occurs at the junction of two sections), the first channel section features a two-flux state of the beam and the VC is formed at the front of the voltage pulse applied to the diode. For this reason, low-energy electrons reflected from the VC are accumulated in the drift channel (rather than returned to cathode), which leads to an increase in the electron density and in the potential energy of particles in the beam behind the VC. This probably accounts for the discrepancy between the results of measurements and the approximate calculations for this interval of I_{inj} (Fig. 3b, curve *BCE*), in which this effect was ignored.

In conclusion, we have reported on the first experimental verification of the possibility of obtaining elec-

tron beams in the squeezed state, in which the relativistic factor γ_b of electrons in the beam is below the value corresponding to the limiting current ($\gamma < \Gamma^{1/3}$).

Acknowledgments. This study was supported by the Russian Foundation for Basic Research (project no. 04-02-16527a).

REFERENCES

1. B. N. Breizman and D. D. Ryutov, Nucl. Fusion **14**, 873 (1974).
2. A. M. Ignatov and V. P. Tarakanov, Phys. Plasmas **1**, 741 (1994).
3. A. A. Grishkov, S. Ya. Belomyttsev, S. D. Korovin, and V. V. Ryzhov, Pis'ma Zh. Tekh. Fiz. **29** (22), 46 (2003) [Tech. Phys. Lett. **29**, 944 (2003)].
4. S. D. Korovin and V. V. Rostov, Izv. Vyssh. Uchebn. Zaved., Fiz., No. 12, 21 (1996).
5. V. P. Tarakanov, *User's Manual for Code KARAT* (Berkley, Springfield, 1992).
6. S. Ya. Belomyttsev, A. A. Grishkov, S. A. Kitsanov, *et al.*, Pis'ma Zh. Tekh. Fiz. **31** (2), 22 (2005) [Tech. Phys. Lett. **31**, 55 (2005)].

Translated by P. Pozdeev

Technical Physics Letters, Vol. 31, No. 11, 2005, pp. 986–988. Translated from Pis'ma v Zhurnal Tekhnicheskoĭ Fiziki, Vol. 31, No. 22, 2005, pp. 82–86.

The Sound Velocity Profile and the Effect of Weak Shock Wave Destruction in the Positive Column of Transverse Glow Discharge

A. S. Baryshnikov*, I. V. Basargin, and M. V. Chistyakova

Ioffe Physicotechnical Institute, Russian Academy of Sciences, St. Petersburg, 194021 Russia

** e-mail: al.bar@mail.ioffe.ru*

Received June 24, 2005

Abstract—The sound velocity profile in the direction across the positive column of glow discharge in air has been experimentally measured and theoretically calculated. The sound velocity exhibits a sharp local increase, which coincides in the experimental and theoretical profiles. *© 2005 Pleiades Publishing, Inc.*

In studying the stability and destruction of shock waves in the case of glow discharge in air, it is important to use a correct classification of the observed phenomena. For a strong shock wave, the electric plasma is an energy medium with a high degree of excitation of the internal degrees of freedom. This situation is analogous to that in the case of exothermal reactions, such as explosion or combustion, in which the instability is described in terms of the classical theory of shock wave instability [1]. However, a thorough analysis of plasma instabilities shows that, in the case of a plasma in air, the instability is restricted to moderate Mach numbers (approximately to M = 3–5) and appears only in the presence of restrictions imposed on the preexponential factor of the equilibrium constant (Saha's formulas). For a weak shock wave, the situation is substantially different and the aforementioned mechanism is impossible. Therefore, the destruction of a weak shock wave can be explained only within the framework of a description of the relaxation of excited plasma components [2].

The results of our experiments performed using a setup described elsewhere [3], in which ultimately low shock wave velocities (on a level of the sound velocity in plasma) at which the shock wave still exists were measured, showed that the sound velocity exhibits sharp local maxima in the direction across the discharge column (Fig. 1). The question arises as to whether this behavior is related to the presence of a charged component or is determined entirely by the laws of sound velocity dispersion in reacting mixtures. The answer must show us whether it is possible to use the observed effect in more than the plasma alone, the formation of which is energy consuming.

Calculation of the velocity of sound is not a simple problem even for a single-temperature mixture of reacting gases. In low-temperature plasma, where physicochemical processes are determined both by the temperature of a heavy component (atoms) and by that of the light component (electrons), solving this problem involves additional complications. In the case of an equilibrium mixture of reacting components, it is possible to use the method of the transition to a system of intense thermodynamic parameters proposed by Rydalevskaya [4, 5]. According to this method, the sound velocity is defined as a square root of the coefficient entering into the wave equation for the density of the heavy component. The approach can be applied to the investigation of flows in gas mixtures featuring various physicochemical processes. In order to determine the influence of various components, the sound velocity calculations can be performed for a gas mixture, with a sequential addition of the required components. This

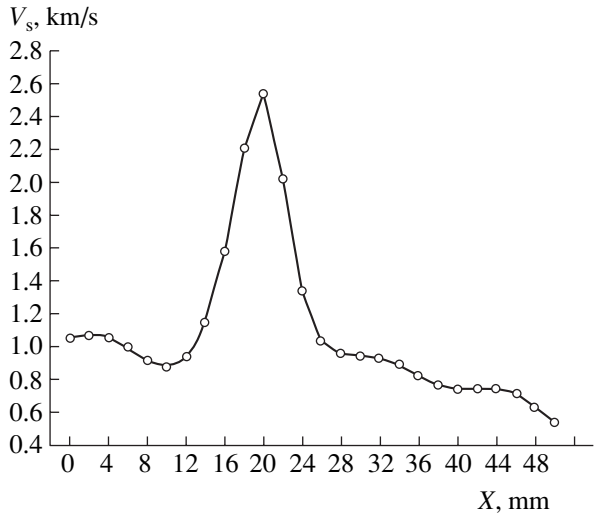

Fig. 1. The experimental sound velocity profile along the radius of the positive column of glow discharge in air.

1063-7850/05/3111-0986$26.00 © 2005 Pleiades Publishing, Inc.

approach not only simplifies the calculation, but also provides grounds for assuming that the resulting equilibrium sound velocity approximately describes (discretely, but with small jumps) the dependence of the nonequilibrium sound velocity on the concentrations of reacting components. At the same time, the process of the establishment of equilibrium can be considered as a discrete series of such processes with respect to separate components, for example, via the formation of transition complexes. We believe that this methodological idea is also applicable to the establishment of temperature equilibrium between light and heavy components of a mixture.

The nonequilibrium state of a low-temperature plasma with respect to the temperature poses the problem of taking into account the existence of two temperatures in this medium. The energy of heavy particles in the plasma is insufficient for the effective excitation, dissociation, and ionization. We may assume that physicochemical processes involving the Coulomb interaction at small scattering angles [6, 7] are determined by the temperature of electrons (whose energy is high and is maintained by the electric field). More precisely, we must consider the effective electron temperature T_e^{eff}, which is 10–20% lower than the electron temperature T_e, since a certain portion of the particles is still excited due to collisions with heavy particles. This effective reduction in the electron temperature is indicated in Fig. 2 as a percentage decrease from T_e.

We have calculated the radial profiles of the concentrations of component and of the sound velocity in the plasma column using the method described in [4, 5] with the partition functions taking into account the translational and rotational degrees of freedom, the excitation of vibrational and electron degrees of freedom, and the dissociation and ionization of components (the distributions of the temperatures of electrons and atoms were taken from the experimental data [8, 9]). The temperature determining these processes was calculated as the average-weighed value using the formula $T^{\text{eff}} = \alpha T_e^{\text{eff}} + (1 - \alpha)T_a$, where the weight α decreased from unity at the discharge axis to zero at the periphery as a linear function of the ratio of the total cross section to the translational cross section, so that the temperature varies from T_e^{eff} on the axis to T_a at the periphery.

In our experiments, a local increase in the velocity of sound was observed at a distance of about 20 mm from the axis (Fig. 1). The results of calculations performed for the effective electron temperature 20% below T_e also showed an increase in the relative concentration of excited components at a distance of approximately 20 mm from the center (Fig. 2a). At the same time, a 20–40% decrease in the electron temperature leads to a local increase in the sound velocity at a distance of 20–30 mm from the center (Fig. 2b). The results of calculations also revealed a small increase at the center of the discharge column, which was confirmed in experiment.

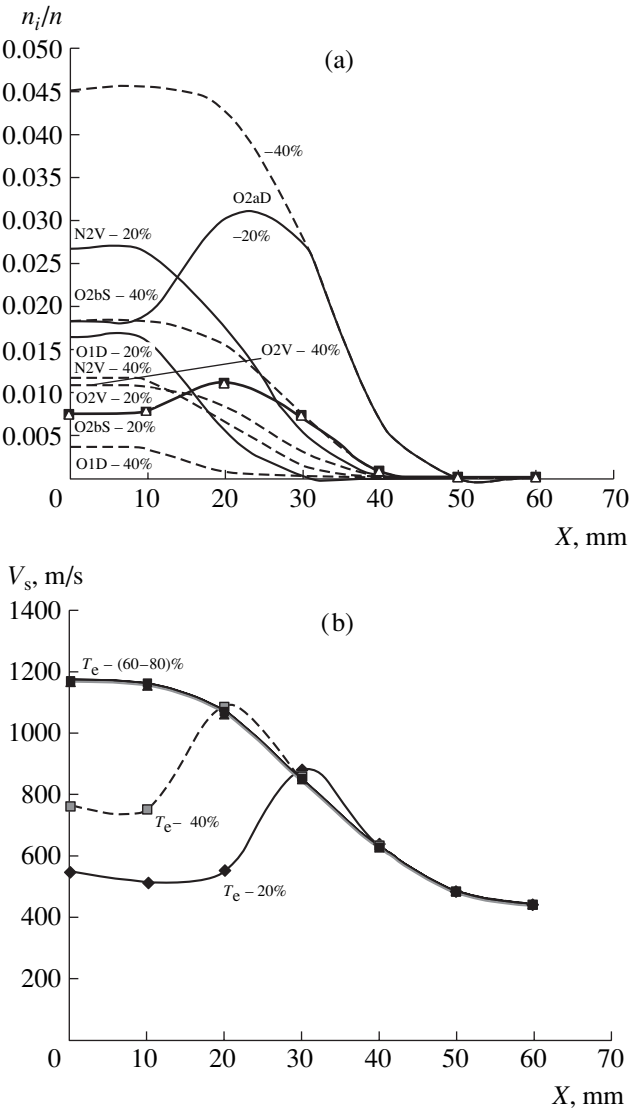

Fig. 2. The calculated radial profiles of (a) the concentrations of excited components and (b) the sound velocity across the positive column of glow discharge in air: O2aD–O_2 ($a_1\Delta$), O2aD–O_2 ($b_1\Sigma$), O1D–O ($b_1\Sigma$), N2V, and O2V are the concentrations of components with the average energies of vibrational excitation; dashed and solid curves refer to the cases of T_e reduced by 40 and 20%, respectively.

REFERENCES

1. Ya. B. Zel'dovich, G. I. Barenblatt, V. B. Librovich, and G. M. Makhviladze, *Mathematical Theory of Combustion and Explosion* (Nauka, Moscow, 1980).

2. A. S. Baryshnikov, I. V. Basargin, and M. V. Chistyakova, Zh. Tekh. Fiz. **71** (3), 17 (2001) [Tech. Phys. **46**, 287 (2001)].

3. A. S. Baryshnikov, I. V. Basargin, and M. V. Chistyakova, in *Proceedings of the Conference on the Physics of Compressible Turbulent Mixing, St. Petersburg, 1999*, p. 461.
4. M. A. Rydalevskaya, *Statistical and Kinetical Models in Physicochemical Gas Dynamics* (St. Petersburg State University, St. Petersburg, 2003) [in Russian].
5. M. A. Rydalevskaya, in *Aerodynamics*, Ed. by P. N. Miroshin (St. Petersburg State University, St. Petersburg, 2000), p. 83 [in Russian].
6. L. S. Polak, *Nonequilibrium Chemical Kinetics and Applications* (Nauka, Moscow, 1979) [in Russian].
7. J. H. Ferziger and H. G. Kaper, *Mathematical Theory of Transport in Gases* (North-Holland, Amsterdam, 1972).
8. I. V. Basargin and A. P. Vasil'ev, FTI Preprint No. 1643 (Ioffe Physicotechnical Institute, Russian Academy of Sciences, St. Petersburg, 1995).
9. I. V. Basargin and G. I. Mishin, FTI Preprint No. 860 (Ioffe Physicotechnical Institute, USSR Academy of Sciences, Leningrad, 1984).

Translated by P. Pozdeev

Technical Physics Letters, Vol. 31, No. 11, 2005, pp. 989–992. Translated from Pis'ma v Zhurnal Tekhnicheskoĭ Fiziki, Vol. 31, No. 22, 2005, pp. 87–94.

Charge and Mass Transfer in the Cathode Plasma Jet of a Low-Inductance Vacuum Spark

S. P. Gorbunov[a], V. I. Krasov[a], V. L. Paperny[a], Yu. V. Korobkin[b,*], and I. V. Romanov[b]

[a] *Irkutsk State University, Irkutsk, Russia*

[b] *Lebedev Institute of Physics, Russian Academy of Sciences, Moscow, Russia*

* *e-mail: korobkin@sci.lebedev.ru*

Received June 24, 2005

Abstract—The contributions of fast and slow ion components to the average mass transfer rate in the cathode plasma jet of a low-inductance vacuum spark have been determined using time-of-flight measurements. The total mechanical momentum of the cathode plasma jet has been found using the ballistic pendulum technique. The coefficient γ of ion erosion of a cathode material was evaluated in the range of discharge current amplitudes 3–13 kA and the discharge current buildup rates 4×10^9–1.5×10^{10} A/s. The γ value exhibits small variations in the indicated range of discharge parameters and is close to the values known for vacuum arcs. © *2005 Pleiades Publishing, Inc.*

Introduction. As is known, a plasma jet in vacuum discharge arises at the cathode and expands into the interelectrode gap. According to the ecton model, the plasma generation processes in stationary vacuum arc and spark discharges are generally similar [1]. Using this model, it is possible to estimate an important parameter called the ion erosion coefficient and defined as $\gamma = M/Q$, where M is the mass of a cathode material transferred by the discharge current and Q is the transferred charge. The γ value has proven to be independent of the discharge current buildup rate below a certain threshold $(dI/dt)_{th} \approx 1.4 \times 10^8$ A/s [2]. Previously, the ion erosion coefficients were measured for various cathode materials under stationary arc discharge conditions with arc currents in the range from 50 A to 1 kA [3]. Recent measurements performed using pulsed arc discharge with a pulse duration of about 300 μs gave γ values close to those reported in [4]. The close coincidence of the calculated γ values with the experimental data for various cathode materials was important evidence for the validity of the ecton model of vacuum arc discharge. The applicability of this model to spark discharges, for which the ion erosion measurements were previously performed at relatively small discharge currents (on the order of several tens of amperes) and current buildup rates (on the order of 10^9 A/s) [5, 6], has been studied to a lesser extent.

In this context, the aim of this study was to establish the main laws of the charge and mass transfer in the cathode plasma jet of vacuum spark discharge at elevated amplitudes (above 10 kA) and buildup rates (up to 3×10^{10} A/s) of the discharge current.

Experimental. The investigations were performed with low-inductance (L = 40 nH) vacuum spark discharge. The electrode system comprised a cylindrical copper cathode with a diameter of 1 mm occurring at a distance of 9 mm from an anode connected to a grounded vacuum chamber with a diameter of 50 mm and a length of 100 mm. The residual pressure in the vacuum chamber was (5–8) × 10^{-6} Torr. A capacitive energy store (C = 2 μF) was charged to an initial voltage of U_d and then used for initiating a discharge at the cathode edge by means of a high-voltage breakdown over the surface of a dielectric sleeve between the cathode and a firing electrode. The discharge current with the amplitude determined by the U_d value was measured directly in the cathode circuit. The temporal resolution of the measuring system was about 40 ns.

The experiments were carried out in two variants. In the first variant, the ion flow velocity was measured using the time-of-flight technique in the discharge chamber with a grid anode, through which the plasma generated at the cathode edge expanded into a drift tube with a length of L = 10 or 36 cm. After traveling via this channel, ions were detected on a collector occurring at a negative potential of 200 V relative to the anode, which corresponded to the ion saturation current. In the second variant, the mechanical momentum of the cathode plasma jet was measured using a ring anode with a 10-mm central hole, through which the ion jet was emitted from the interelectrode gap to strike a ballistic pendulum (a metal disk weighing 0.35 g) suspended on a grounded metal filament. The angle of deviation of the disk under the action of the plasma jet was measured to determine the mechanical momentum transfer from the jet to the pendulum.

Results. Figure 1 presents the results of the time-of-flight measurements using drift tubes of different lengths. As can be seen, the cathode plasma jet consists of ions of two types. A smaller delay relative to the

1063-7850/05/3111-0989$26.00 © 2005 Pleiades Publishing, Inc.

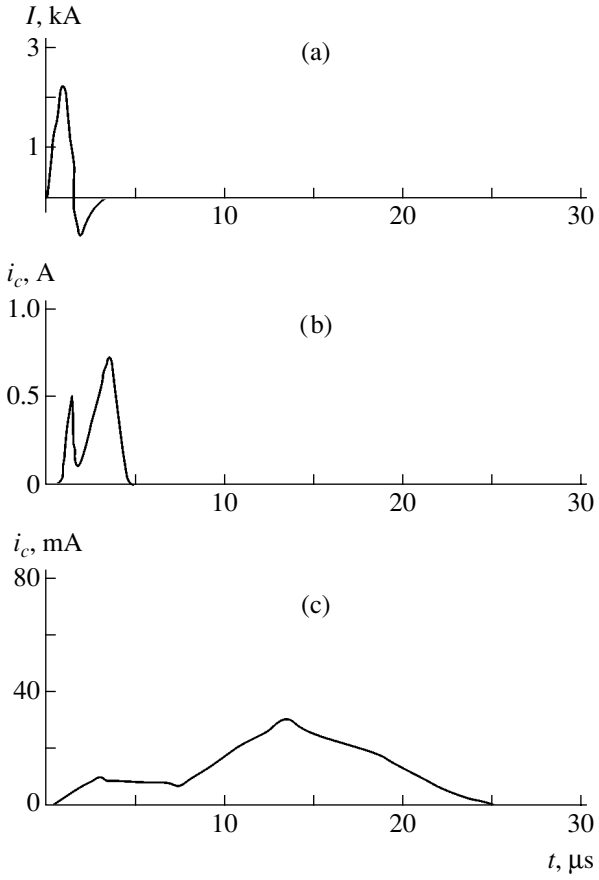

Fig. 1. The typical oscillograms of (a) discharge current and (b, c) ion current measured at the collector for a drift tube length of L = 10 and 36 cm, respectively.

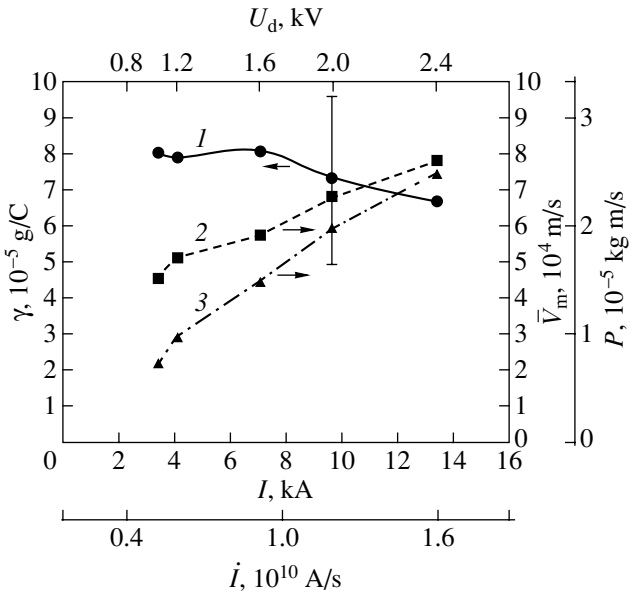

Fig. 2. Plots of the (*1*) ion erosion coefficient γ, (*2*) average mass transfer rate $\bar{V}_m$, and (*3*) average mechanical momentum of the cathode jet plasma versus parameters of the vacuum spark discharge.

onset of discharge corresponds to a fast ion component, while a greater delay corresponds to the slow component. An analysis of the obtained data showed that the fast component represents multiply charged ions of cathode material, which are generated in the initial stage of discharge [7]. The slow component accounts for the main part of ions of the cathode plasma jet, and the average ion velocity in this component at a small amplitude of the discharge current is close to the standard ion velocity in vacuum arc discharge [8]. As the discharge current amplitude is increased, the average velocities for both plasma jet components grow. It is important to emphasize that, even with allowance for a rather large average ion charge, the number of fast ions in each pulse (which is proportional to the area under the corresponding part of the oscillogram in Fig. 1b), accounts for a quite significant part (several tens of percent) of the total ion current. Therefore, since the velocity of fast ions is 3–5 times that of ions in the main (slow) component, it is necessary to take into account the contribution of the fast component to the total mechanical momentum of the cathode plasma jet.

For a given value of the initial stored charge and the corresponding discharge current amplitude, the velocities of both ion current components were calculated by averaging data over a series of oscillograms. The velocity of the main component was determined from the delay of the maximum of the corresponding signal of the collector current relative to the first peak of the discharge current (which corresponds, according to the ecton model, to the peak of the ion current). The velocity of the fast component was determined from the delay of the maximum of the corresponding signal relative to the initial time moment t_0 = 300 ns from the onset of discharge. This moment of time corresponds, according to the results of preliminary investigations [7], to the generation of fast multiply charged ions in spark discharge. The ion velocities were determined using only experimental data for the drift tube with L = 36 cm, which provided (see Fig. 1) for a satisfactory accuracy (about 20%).

Using the ion velocities of the current components measured as described above, we determined the average mass transfer rate $\bar{V}_m$ in the cathode plasma jet with allowance for the relative content of the ions of two types. This ratio was evaluated from the collector signal components measured using the tube with L = 10 cm. As can be seen from the data presented in Fig. 2, the average mass transfer rate $\bar{V}_m$ exhibits a significant growth with increasing discharge current amplitude. Figure 2 also shows the mechanical momentum P of the plasma jet, which was determined using the ballistic pendulum technique. It was assumed that the entire momentum of the plasma jet is transferred to the pendulum and that the reflection of ions from the pendulum surface can be ignored.

Using data on the charge, mass, and momentum transfer in the plasma jet, we evaluated the ion erosion coefficient as

$$\gamma = \frac{M}{Q} = \frac{P\bar{V}_m}{Q} = \frac{P/\bar{V}_m}{CU_d},$$

where M and Q are the total mass of the cathode material and the total charge transferred by the plasma in each pulse. The dependence of γ on the discharge parameters is presented in Fig. 2. As can be seen, the variation of the ion erosion coefficient in response to a more than threefold increase in the discharge current amplitude and buildup rate, as well as approximately the same growth in the mechanical momentum of the cathode plasma jet, does not exceed 20% and falls within the experimental accuracy limits. The absolute value of γ is also close (taking into account the relatively low accuracy of mechanical measurements) to the well-known value for vacuum arc discharge with copper cathode: $\gamma \approx 40$ μg/C [3].

Discussion. The results of our investigation show that the coefficient of ion emission for the given cathode material is a stable parameter having close values for the stationary arc and spark discharges with relatively high current buildup rates (above 10^{10} A/s). The value of γ exhibits relatively small variations when the discharge current changes from tens of amperes (in arc discharge) to more than 10 kA (in the spark discharge studied in our experiments), that is, by almost four orders of magnitude. These results provide evidence for the applicability of the ecton model to the vacuum discharges of various types in a broad range of their parameters.

Using the obtained data, it is also possible to estimate the mechanical momentum of a cathode plasma jet produced by the given ion source per unit of transferred charge: $P/Q \approx 5 \times 10^{-3}$ (kg m)/(s C), which is one and a half orders of magnitude greater than the typical value for a vacuum arc (about 2×10^{-4} (kg m)/(s C) [1]). The significantly higher specific momentum transfer observed in our system can be explained by several factors. First, the data in Fig. 2 show that the cathode plasma jet velocity in our case is 3–6 times that in the arc discharge. Second, the vacuum discharge at currents above 1 kA is accompanied by radial contraction of the plasma jet under the action of the intrinsic magnetic field [9], which decreases the spread of the transverse ion velocity and increases the longitudinal momentum of the plasma jet. Third, the value of the momentum transfer estimated using the ballistic pendulum technique can be overstated due to the possible ion reflection from the pendulum surface.

It should also be noted that another well established fact is the presence of fast and slow ion components at zero current in a laser-generated plasma. This phenomenon is related to the emission of hot electrons in a plasma jet expanding in vacuum. The ambipolar field of these electrons entrains a fraction of ions and accelerates them to energies significantly exceeding that in the thermal region of the ion energy distribution (see, e.g., [10]). Recently, we reported on the high-energy electron beams generated by a current-carrying cathode plasma jet in the initial stage of vacuum spark discharge [11]. In this case, the electron beam generation is explained by the formation of micropinch structures at the plasma jet front, where the plasma is heated to a temperature of $T_e \approx 100$–200 eV [11, 12]. It is natural to assume that the fast ion component observed in the present experiments also appears as a result of the entrainment of multiply charged ions formed in the micropinch by the ambipolar field of high-energy electrons.

Let us consider some possible applications of the above results. At present, the maneuver reaction propulsors intended for correcting the orbits of artificial satellites predominantly employ gas plasma accelerators that are based on the closed electron drift effect. The results presented in this paper show the principal possibility of using vacuum spark discharge for the development of a small-size plasma propulsor with sufficiently high thrust characteristics. In the present state of the art in this field, such a propulsor has the following parameters:

(i) weight (without power supply source), not exceeding 1 kg;

(ii) thrust force (at a 10 Hz pulse repetition rate), about 10^{-3} N;

(iii) efficiency ($P\bar{V}_m/CU_d^2$), up to 20%;

(iv) power consumption, below 50 W;

(v) characteristic velocity, up to 8×10^6 cm/s.

The advantages of the proposed ion jet propulsor are the simple design, the absence of heated and eroded elements (except for the cathode, which is a working body), and the possibility of using metals with large atomic weights as working bodies in order to increase the propulsion characteristics.

Acknowledgments. This study was supported by the Russian Foundation for Basic Research (project no. 03-02-16366).

REFERENCES

1. G. A. Mesyats, *Ectons in Vacuum Discharge: Breakdown, Spark, Arc* (Nauka, Moscow, 2000) [in Russian].
2. G. A. Mesyats, in *Proceedings of the 18th International Symposium on Discharges and Electrical Insulation in Vacuum, Eindhoven, Netherlands, 1998,* Vol. 2, pp. 720–731.
3. J. E. Daalder, Physica B & C **104** (1), 91 (1981).

4. A. Anders, E. Oks, and G. Yushkov, in *Proceedings of the 21st International Symposium on Discharges and Electrical Insulation in Vacuum, Yalta, Ukraine, 2004*, Vol. 1, pp. 272–275.

5. G. A. Mesyats and D. I. Proskurovsky, *Pulsed Electric Discharge in Vacuum* (Nauka, Novosibirsk, 1984) [in Russian].

6. S. A. Popov, D. I. Proskurovsky, and A. V. Batrakov, in *Proceedings of the 19th Internationals Symposium on Discharge and Electrical Insulation in Vacuum, Xi'an, China, 2000*, Vol. 1, pp. 81–84.

7. M. F. Artamonov, V. I. Krasov, and V. L. Paperny, J. Phys. D: Appl. Phys. **34**, 3364 (2001).

8. S. P. Gorbunov, V. I. Krasov, I. A. Krinberg, and V. L. Paperny, Plasma Sources Sci. Technol. **12**, 313 (2003).

9. D. F. Alferov, N. I. Korobova, and I. O. Sibiryak, Fiz. Plazmy **19**, 399 (1993).

10. F. B. Rosmej, D. H. H. Hoffmann, W. Süß, *et al.*, Zh. Éksp. Teor. Fiz. **121**, 73 (2002) [JETP **94**, 60 (2002)].

11. Yu. V. Korobkin, I. V. Romanov, A. A. Rupasov, and A. S. Shikanov, Zh. Tekh. Fiz. **75** (9), 34 (2005) [Tech. Phys. **50**, 1139 (2005)].

12. M. F. Artamonov, V. I. Krasov, and V. L. Paperny, Prikl. Fiz., No. 5, 34 (2003).

Translated by P. Pozdeev